2011-06-16

An Evaluation of Constitutive Laws and their Ability to Predict Flow Stress over Large Variations in Temperature, Strain, and Strain Rate Characteristic of Friction Stir Welding

Katherine Lynn Kuykendall
Brigham Young University - Provo

An Evaluation of Constitutive Laws and their Ability to Predict Flow Stress over Large Variations in Temperature, Strain, and Strain Rate Characteristic of Friction Stir Welding

Katherine Kuykendall

A dissertation submitted to the faculty of
Brigham Young University
in partial fulfillment of the requirements for the degree of

Doctor of Philosophy

Tracy W. Nelson, Chair
Carl D. Sorensen
David T. Fullwood
Anton Bowden
Michael P. Miles

Department of Mechanical Engineering

Brigham Young University

August 2011

ABSTRACT

An Evaluation of Constitutive Laws and their Ability to Predict Flow Stress
Over Large Variations in Temperature, Strain, and Strain Rate
Characteristic of Friction Stir Welding

Katherine Kuykendall
Department of Mechanical Engineering, BYU
Doctor of Philosophy

Constitutive laws commonly used to model friction stir welding have been evaluated, both qualitatively and quantitatively, and a new application of a constitutive law which can be extended to materials commonly used in FSW is presented.

Existing constitutive laws have been classified as path-dependent or path-independent. Path-independent laws have been further classified according to the physical phenomena they capture: strain hardening, strain rate hardening, and/or thermal softening. Path-dependent laws can track gradients in temperature and strain rate characteristic to friction stir welding; however, path-independent laws cannot. None of the path-independent constitutive laws evaluated has been validated over the full range of strain, strain rate, and temperature in friction stir welding. Holding all parameters other than constitutive law constant in a friction stir weld model resulted in temperature differences of up to 21%. Varying locations for maximum temperature difference indicate that the constitutive laws resulted in different temperature profiles.

The Sheppard and Wright law is capable of capturing saturation but incapable of capturing strain hardening with errors as large as 57% near yield. The Johnson-Cook law is capable of capturing strain hardening; however, its inability to capture saturation causes over-predictions of stress at large strains with errors as large as 37% near saturation. The Kocks and Mecking model is capable of capturing strain hardening and saturation with errors less than 5% over the entire range of plastic strain. The Sheppard and Wright and Johnson-Cook laws are incapable of capturing transients characteristic of material behavior under interrupted temperature or strain rate. The use of a state variable in the Kocks and Mecking law allows it to predict such transients.

Constants for the Kocks and Mecking model for AA 5083, AA 3004, and Inconel 600 were determined from Atlas of Formability data. Constants for AA 5083 and AA 3004 were determined with the traditional Kocks and Mecking model; however, constants for Inconel 600 could not be determined without modification to the model. The temperature and strain rate combinations for Inconel 600 fell into two hardening domains: low temperatures and high strain rates exhibited twinning while high temperatures and low strain rates exhibited slip. An additional master curve was added to the Kocks and Mecking model to account for two hardening mechanisms. The errors for the Kocks and Mecking model predictions are generally within 10% for all materials analyzed.

Keywords: friction stir welding, constitutive law, modeling, flow stress, stacking fault energy

ACKNOWLEDGMENTS

I would like to thank my husband Brad for encouragement and emotional support, my advisors, Tracy Nelson and Carl Sorensen, for countless hours of guidance and direction, and Scott Taysom for performing experiments analyzed in this dissertation.

This research was made with Government support under and awarded by DoD, Air Force Office of Scientific Research, National Defense Science and Engineering Graduate (NDSEG) Fellowship, 32 CFR 168a.

TABLE OF CONTENTS

LIST OF TABLES

LIST OF FIGURES

1 INTRODUCTION

1.1 Friction Stir Welding

Friction stir welding (FSW) is a solid state bonding process patented by The Welding Institute (TWI), Cambridge, U.K., in 1991 [1]. Bonding results from the combined action of mechanical deformation and frictional heating due to a rotating tool composed of a shoulder and a pin (Figure 1-1). The tool is plunged into the seam of two plates until the shoulder contacts the workpiece. Once sufficient heat is sustained, the tool traverses along the seam to create the weld.

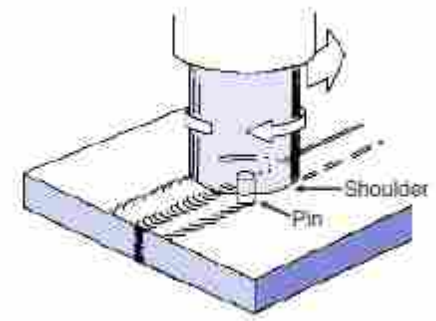

Figure 1-1: Friction stir welding schematic [2].

FSW is a localized deformation process characterized by large strain and moderate- to high-strain rate at elevated-temperature. The strain, strain rate, and temperature change over a very small distance. Strain and strain-rate have been reported from zero to maximum over a few

millimeters, and temperatures from zero to maximum over a few centimeters. While various metalworking and joining models have been used to model FSW, the steep gradients in strain, strain rate, and temperature inherent in FSW potentially limit the accuracy of such models.

1.2 FSW Modeling

There have been several attempts to model friction stir welding. Discrepancies in temperature, strain, and strain rate predictions exist amongst the various attempts. Temperatures have been predicted between 0.6 and 0.95 times the absolute melting temperature of the material. Peak strain rates have been predicted from 1 to 1000 s^{-1}, and peak strains from 1 to 80.

There are several reasons for discrepancies in maximum strains, strain rates, and temperatures reported from model predictions. Parameters that may account for discrepancies that are not inherent results of modeling are materials and weld parameters such as the rotational speed of the tool or the traverse speed of the plate. However, there are several parameters that are specific to the model itself.

Boundary conditions and heat transfer properties are variables specific to a model. Because these variables are unknown, estimations must be made to compute their values. For example, although the heat transfer between the workpiece and the backing plate is conduction, the heat transfer is often modeled as convection with an experimentally determined convection heat transfer coefficient [3].

Constitutive law is also a model specific variable that may account for discrepancies in predicted temperatures, strains, and strain rates. A constitutive law consists of a set of parametric equations that characterizes flow stress as a function of strain rate and temperature

and accounts for the prior strain, strain rate, and temperature history of the material; and a set of constants determined to fit the parametric equations to the behavior of a given material.

A variety of constitutive laws is available for those who model hot deformation processes. In this dissertation, constitutive laws are classified as path-independent or path-dependent. Several of the path-independent laws commonly used to model friction stir welding have been proven successful in metals process simulation for isothermal, uniform strain rate processes such as hot rolling [4]. However, such conditions do not exist in friction stir welding where temperature and strain rate are variable outputs of the process.

1.3 Objective

The objective of this research is to analyze constitutive laws commonly used to model friction stir welding, both qualitatively and quantitatively, and to present a new application of a constitutive law which can be extended to materials commonly used in FSW.

1.4 About this Dissertation

This dissertation consists of a collection of three papers that will be submitted for publication. The first paper is a qualitative analysis which compares characteristics of commonly used constitutive laws and their applicability in the various zones of a typical friction stir weld. Two path-independent laws, namely Sellars and Tegart and Johnson-Cook, and one path-dependent law, Kocks and Mecking are implemented into a two-dimensional finite element friction stir welding model to investigate the effect of constitutive law on model predictions. Appendix A describes the changes made to the source code to implement the constitutive laws.

The second paper consists of a quantitative analysis focused on the Sellars and Tegart, Johnson-Cook, and Kocks and Mecking laws. Predictions for these three constitutive laws are

evaluated against experimental data for isothermal, constant strain rate conditions as well as interrupted temperature and strain rate conditions. Model performance near yield and saturation and upon changes in temperature and strain rate is considered.

The third paper describes an extension of the Kocks and Mecking model from pure fcc metals to solid-solution strengthened fcc metals of various stacking fault energies. A discussion of the influence of stacking fault energy and test parameters, namely temperature and strain rate, on dominant hardening mechanisms is presented.

2 ON THE SELECTION OF CONSTITUTIVE LAWS USED IN MODELING FRICTION STIR WELDING

2.1 Abstract

Discrepancies in friction stir welding model predictions for temperature, strain, and strain rate may be due to material, process parameters, boundary conditions, heat transfer properties, or constitutive laws. The focus of this work is to investigate the effect of the constitutive law on friction stir welding model predictions. This paper provides a description of constitutive laws with their uses and limitations to facilitate the selection of an appropriate constitutive law for a given modeling objective.

None of the path-independent constitutive laws evaluated in this paper has been validated over the full range of strain, strain rate, and temperature in friction stir welding. Holding all parameters other than constitutive law constant in a friction stir weld model resulted in temperature differences of up to 21%. Varying locations for maximum temperature difference indicate that the constitutive laws resulted in different temperature profiles. Peak strains and strain rates predicted vary by up to 130% and 166%, respectively. Predicted flow stress profiles are also affected by the choice of constitutive law.

2.2 Introduction

Friction stir welding (FSW) is a large strain, moderate- to high-strain rate, elevated-temperature deformation process. Strain values have been reported as high as 80 in a limited

volume of the weld [5], strain rates as high as 160 s^{-1} [6], and temperatures up to 0.95 times the absolute melting temperature of the material [7]. While exact values are uncertain, the peak strains, strain rates, and temperatures in FSW are higher than most metalworking processes.

The strain, strain rate, and temperature change over a very small distance. Strain and strain-rate go from zero to the maximum over a few millimeters, and temperature goes from room temperature to the maximum over a few centimeters. While various metalworking and joining models have been used to model FSW, the steep gradients in strain, strain rate, and temperature inherent in FSW potentially limit the accuracy of such models.

To develop accurate models of the friction stir welding process, a valid constitutive law is required throughout the entire weld. A constitutive law consists of a set of parametric equations that characterizes flow stress as a function of strain rate and temperature and accounts for the prior strain, strain rate, and temperature history of the material; and a set of constants determined to fit the parametric equations to the behavior of a given material.

A variety of constitutive laws is available for those who model hot deformation processes. In this paper, constitutive laws are classified as path-independent or path-dependent. Several of the path-independent laws commonly used to model friction stir welding have been proven successful in metals process simulation for isothermal, constant strain rate processes such as hot rolling [4]. However, such conditions do not exist in friction stir welding where temperature and strain rate are variable outputs of the process.

Those who model the FSW process often use constitutive laws without any justification for why the particular law was chosen. Virtually all constitutive laws used to date in modeling FSW are path-independent. Currently, only one path-dependent constitutive law is being used in FSW models [8]; however, the use of a second path-dependent law is investigated.

Characteristic strains, strain rates, and temperatures reported in FSW are identified. Constitutive laws commonly used to model FSW are reviewed, and reported strains, strain rates, and temperatures are compared to the ranges over which path-independent law constants have been developed. Results from FSW simulations run in Hickory, a two-dimensional finite element model, for several constitutive laws are compared.

2.3 Characteristic Temperatures, Strains, and Strain Rates in a Typical FSW Weld

The values of strain, strain rate, and temperature in friction stir welding are higher than most metalworking processes. Strain values have been reported from 0 to 80 [5]. Maximum strain rate values have been reported between 100 s^{-1} [9] and 1000 s^{-1} [10], and maximum temperatures have been reported as high as 0.6 to 0.95 times the absolute melting temperature of the material [7].

Figure 2-1 is a schematic of a typical FSW weld which consists of four distinct zones: base metal, heat affected (HAZ), thermomechanically affected (TMAZ), and nugget (stirred).

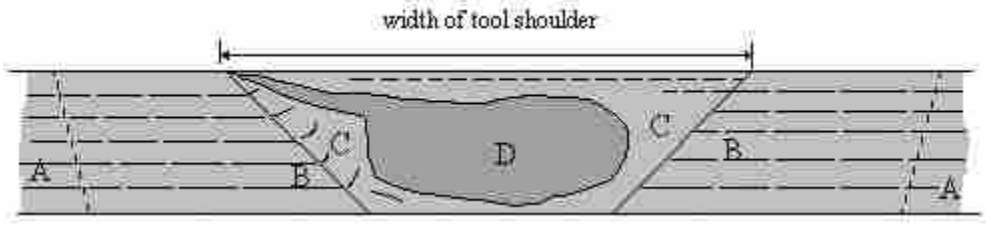

Figure 2-1: Schematic cross-section of a typical SW weld showing four distinct zones: (A) base metal, (B) heat affected, (C) thermomechanically affected, and (D) stirred (nugget) zone.

No material deformation has occurred in the base metal (Zone A). The material has not been measurably affected by the thermal cycle in terms of microstructure or mechanical properties [11].

In the HAZ (Zone B) the material has undergone a thermal cycle which has modified the microstructure and/or the mechanical properties. However, no plastic deformation has occurred in this area [11].

In the TMAZ (Zone C) the material has been plastically deformed by the tool, and the heat flux has also exerted some influence on the material. By definition, there is no recrystallization in the TMAZ for aluminum alloys; however, extensive deformation is present [11]. The TMAZ experiences lesser strains and strain rates as well as lower peak temperatures than the stir zone.

The maximum temperature occurs in the stir zone (Zone D). The stir zone or nugget is the recrystallized area in the TMAZ in aluminum alloys. In the nugget, the original grain and subgrain boundaries appear to be replaced with fine equiaxed recrystallized grains [11].

There is no deformation in the HAZ, and thus constitutive laws are not used to model the HAZ. However, material on the leading edge of the tool has characteristic HAZ temperatures and may be deformed while at the characteristic HAZ temperatures. The evolution of the deformation will be predicted by a constitutive law; thus, temperatures in the HAZ are reported in this paper.

Temperature distributions throughout the weld have been estimated experimentally for aluminum alloys. Unfortunately, information regarding the distribution of strain and strain rate throughout the zones present in a typical FSW weld is limited.

2.3.1 Temperatures

Temperatures will be presented for the HAZ, TMAZ, and nugget regions. The values reported in this section have been further subdivided into results from weld measurements and results from friction stir weld simulations.

2.3.1.1 HAZ Measured

Hamilton et al. [12] performed a study on AA 7136-T76511 extrusions. The distribution of precipitates in the HAZ suggested that temperatures during FSW were adequate to ripen present phases but insufficient for dissolution and reprecipitation. Thus, temperatures within the HAZ most likely exceed/approach the aging temperatures of 7136-T76, i.e. 121 and 157 ˚C, but remain well below the solution heat treat temperature. The maximum temperatures reported by Mahoney et al. [13] for AA 7075 in the HAZ near the unaffected zone (base metal) are between 200 and 300 ˚C.

2.3.1.2 HAZ Modeled

The maximum temperature in the HAZ for AA 2024 reported by Heurtier et al. [14] is 325 ˚C. Song and Kovacevic [15] calculated the maximum temperatures in each zone for a weld performed on AA 6061. The calculated peak temperatures in the HAZ are in the range of 207-337 ˚C.

2.3.1.3 TMAZ Measured

Away from the nugget region toward the TMAZ/HAZ interface, Hamilton et al. [12] estimated maximum temperatures of 276 ˚C for a rotational speed of 350 rev/min and 212 ˚C for a 250 rev/min weld. These temperatures are consistent with the resultant microstructures:

limited dissolution and reprecipitation with a decreased number of coarse particles compared to the nugget region. The maximum temperatures reported by Mahoney et al. [13] for AA 7075 in the TMAZ are between 300 and 475 ˚C.

2.3.1.4 TMAZ Modeled

The maximum temperature in the TMAZ reported by Heurtier et al. [14] for AA 2024 is 425 ˚C. The peak temperatures in the TMAZ calculated by Song and Kovacevic [15] for AA 6061 are in the range of 337-487 ˚C. Nandan et al. [6] report peak temperatures in the TMAZ for AA 6061 between 507 and 527 ˚C.

2.3.1.5 Nugget Measured

Nelson et al. [16], Arbegast et al. [17], and Arbegast and Hartley [18] report that maximum temperatures approach 0.8 times the absolute melting temperature in aluminum alloys.

Jata and Semiatin [19] estimated the maximum temperature in an Al-Li alloy weld. TEM observations of the precipitates in the weld nugget revealed a supersaturated solid solution. Thus, the maximum temperature was estimated to be the solutionizing temperature 540 ˚C.

For AA 2024, Li et al. [20] measured maximum temperatures in the nugget region approaching 0.8 times the absolute melting temperature. Benavides et al. [21] measured a maximum temperature of 330 ˚C in a low-temperature weld.

Schneider et al. [22] performed TEM studies on the weld nugget in AA 2195-T81. TEM studies of the grains within the weld nugget indicate welding temperatures were obtained on the order of 400 ˚C or higher during the FSW process. These temperatures are in agreement with published values for aluminum alloys indicating they are exposed to temperatures in the range of 400 to 450 ˚C during FSW [23, 24].

For AA 6061, Tang et al. [23] measured a peak temperature of 450 ˚C, Murr et al. [24] measured a peak temperature of 425 ˚C, and Li et al. [20] measured peak temperatures not exceeding 0.8 times the absolute melting temperature.

The maximum temperature reported by Sato et al. [25] for AA 6063 is 522 ˚C. Sato et al. [26] measured peak temperatures throughout the weld between 201 and 553 ˚C.

TEM micrographs by Hamilton et al. [12] indicate temperatures at the weld center sufficient to cause coarsening and even dissolution of the strengthening phases followed by reprecipitation upon cooling. The welding temperatures in the nugget were most likely near, but below the standard solution heat treat temperature of AA 7136, i.e. 471 ˚C.

The maximum temperatures reported by Mahoney et al. [13] for AA 7075 in the nugget, TMAZ, and HAZ near the nugget fall between 300 and 475 ˚C.

Lienert et al. [27], report temperature measurements and microstructural evidence for mild steel that indicate peak temperatures in the stir zone exceed 1100 ˚C and likely surpass 1200 ˚C. Tool materials included both molybdenum- and tungsten-based alloys.

2.3.1.6 Nugget Modeled

The maximum temperature reported by Heurtier et al. [14] for AA 2024 is about 475 ˚C. Song and Kovacevic [15] calculated a peak temperature in the nugget of about 562 ˚C for AA 6061. Buffa et al. [28] report maximum temperatures for AA 6082 between 536 and 567 ˚C. Bastier et al. [29] report a maximum temperature for AA 7050 of approximately 498 ˚C.

Khandkar et al. [30] and Buffa et al. [31] studied the temperatures in friction stir welding of stainless steel. The maximum temperatures calculated by Khandkar et al. and Buffa et al. were between 1040 and 1270 ˚C and between 900 and 1200 ˚C, respectively. Khandkar et al. used a tungsten alloy tool, and Buffa et al. used a WC based material.

Table 2-1 summarizes the characteristic temperatures in friction stir welding.

Table 2-1: Characteristic temperatures in frictions stir welding. All melting temperatures are taken from ASM Handbook Volume 2 [32] unless otherwise noted.

First Author	Material	Zone	Method	Reported Temperature (˚C)	Melting Temperature (˚C)	Homologous Temperature
Hamilton [12]	AA7136-T7	HAZ	Measured	121-157	488 [12]	0.52-0.57
Mahoney [13]	AA7075-T6	HAZ	Measured	200-300	477	0.63-0.76
Heurtier [14]	AA2024	HAZ	Modeled	325	502	0.77
Song [15]	AA6061	HAZ	Modeled	207-337	582	0.56-0.71
Hamilton [12]	AA7136-T7	TMAZ	Measured	212-376	488 [12]	0.64-0.72
Mahoney [13]	AA7075-T6	TMAZ	Measured	300-475	477	0.76-1.00
Heurtier [14]	AA2024	TMAZ	Modeled	425	502	0.90
Song [15]	AA6061	TMAZ	Modeled	337-387	582	0.71-0.77
Nandan [6]	AA6061-T6	TMAZ	Modeled	507-527	582	0.91-0.94
†McNelley [7]	AAXXXX	nugget	Measured	--	--	0.60-0.95
†Nelson [16], Arbegast [17], Arbegast [18]	AAXXXX	nugget	Measured	--	--	0.80
Jata [19]	Al-LI alloy	nugget	Measured	540	--	--
Schneider [22]	AA2195-T8	nugget	Measured	400	540 [33]	0.83
†Li [20]	AA2024	nugget	Measured	402	502	0.87
Benavides [21]	AA2024	nugget	Measured	330	502	0.78
Sato [26]	AA6063	nugget	Measured	201-553	615	0.53-0.91
Tang [23]	AA6061-T6	nugget	Measured	450	582	0.85
Murr [24]	AA6061-T6	nugget	Measured	425	582	0.82
Sato [25]	AA 6063	Nugget	Measured	522	615	0.90
†Li [20]	AA6061	nugget	Measured	466	582	0.80
Hamilton [12]	AA7136-T7	nugget	Measured	471	488 [34]	0.98
Mahoney [13]	AA7075-T6	nugget	Measured	300-475	477	0.76-1.00
Lienert [27]	mild steel	nugget	Measured	1100-1200	1520 [35]	0.77-0.82
Heurtier [14]	AA2024	nugget	Modeled	475	502	0.97
Buffa [28]	AA6082-T6	nugget	Modeled	536-567	570 [36]	0.96-1.00
Song [15]	AA6061	nugget	Modeled	562	582	0.98
Bastier [29]	AA7050	nugget	Modeled	498	465	1.04
Khandkar [30]	SS 304L	nugget	Modeled	1040-1270	1400 [37]	0.78-0.92
Buffa [31]	SS 304L	nugget	Modeled	900-1200	1400 [37]	0.70-0.88

† Homologous temperature was reported in the literature. Peak temperatures were calculated when possible.

2.3.2 Strains

Because strain in the HAZ is zero by definition, we only examine strain in the TMAZ and nugget.

Due to the limited data on equivalent strain, there is no clear distinction between strain values in the TMAZ and nugget regions. All values reported in this section are results from friction stir weld simulations.

Heurtier et al. [5] and Heurtier et al. [14] studied AA 2024. Heurtier et al. [5] calculated strain levels in the nugget zone as high as 80. The order of magnitude of the strain is about 40. The strain contours developed are similar to the onion rings geometry reported in the literature [38, 39]. The average equivalent strain in the nugget reported by Heurtier et al. [14] is about 6.

Buffa et al. [28] report maximum effective strains for AA 6082 between 5 and 6, and Buffa et al. [40] report maximum effective strains for AA 7075 between 7 and 9.

Zhang and Chen [41] used simulations to determine the distribution of the equivalent plastic strain in the cross section perpendicular to the welding line in mild steel. The highest strain occurs beneath the pin in the nugget region and at the edge of the shoulder near the top of the workpiece. The highest equivalent strain is estimated at about 5.2.

Buffa and Fratini [31] report a maximum strain level of approximately 50 for friction stir welding of 304 stainless steel.

Table 2-2 summarizes the characteristic strains in friction stir welding.

Table 2-2: Characteristic strains in the TMAZ/nugget region in friction stir welding.

First Author	Material	Method	Reported Strain
Heurtier [5]	AA2024	Modeled	40/80
Heurtier [14]	AA2024	Modeled	6
Buffa [28]	AA6082-T6	Modeled	5-6

Table 2-2 Continued

First Author	Material	Method	Reported Strain
Buffa [40]	AA7075	Modeled	7-9
Zhang [41]	1018 steel	Modeled	5.2
Buffa [31]	304 SS	Modeled	50

2.3.3 Strain Rates

Because strain rate in the HAZ is zero by definition, we only examine strain in the TMAZ and nugget.

Due to the limited data on strain rate, there is no clear distinction between strain rate values in the TMAZ and nugget regions. The values reported in this section have been divided into results from weld measurements and results from friction stir weld simulations.

2.3.3.1 Measured

Many previous papers have attempted to estimate the strain rate during FSW of aluminum alloys. Jata and Semiatin [19] estimated an effective strain rate of 10 s^{-1} using the shear strain extrapolated from that measured in the thermomechanically affected zone and the deformation time in the stir zone.

Previous attempts to estimate strain rate did not consider grain growth during the cooling cycle in FSW [19]. Masaki et al. [42] attempted to simulate the recrystallized grains of the stir zone in AA 1050 through a combination of plane-strain compression at various strain rates and subsequent cooling tracing the cooling cycle of FSW. The effective strain rates calculated were between 1.7 and 2.7 s^{-1}.

In the thermomechanical treatment used in the above study, the fine grains produced at a strain rate higher than about 30 s^{-1} rapidly grew during the subsequent cooling. This result implies that the effective strain rate during FSW would not exceed 100 s^{-1} [42].

Frigaard et al. [43] estimated strain rates for AA 6082 between 1.6 and 10.3 s^{-1} and strain rates for AA 7108 between 1.7 and 17.3 s^{-1} using the measured subgrain size of the stir zone, the computer-simulated maximum temperature, and a simple equation relating the subgrain size and the Zener-Holloman parameter during hot deformation of aluminum alloys.

2.3.3.2 Modeled

Schmidt and Hattel [44] report strain rates in friction stir welding on the order of 1000 s^{-1}; however, Nandan et al. [6] suggest that the strain rates are much lower than 1000 s^{-1}. Nunes et al. [9] estimate the maximum strain rate to be 100 s^{-1}. Askari et al. [45] report maximum strain rates in FSW between 10 and 100 s^{-1} for aluminum alloys.

Darras and Khraisheh [46] performed a study on the strain rate distribution in friction stir processing of aluminum alloys. Their model is capable of accommodating different contact conditions. Computed strain rate values are on the order of hundreds, which is in agreement with reported values in the literature [6, 9].

Buffa et al. [28] estimate strain rates for AA 6082 between 4 and 11 s^{-1}. The strain rate values are larger at the top of the joint because of the shoulder action.

Nandan et al. [6] report that below the surface, maximum strain rate occurs at the surface of the pin where the velocity gradient is highest. Near the top surface of the workpiece, the strain rate is highest near the outer edge of the tool shoulder. Nandan et al. estimate a maximum strain rate of 160 s^{-1} for AA 6061. The order of magnitude of strain rate is higher than 100 s^{-1} near the shoulder, which sharply drops to about 30 s^{-1} at about 4 mm below the shoulder.

Colegrove and Shercliff [47] report strain rates as high as 500 s^{-1} for AA 7449. Buffa et al. [40] report maximum strain rates between 7 and 8 s^{-1} for AA 7075.

Chang et al. [48] estimated strain rates between 1 and 100 s^{-1} (depending on the welding parameters) for AZ31 Mg under the assumption that a torsion-type deformation occurs.

Buffa and Fratini [31] estimated an effective strain rate of 20 s^{-1} for 304 stainless steel.

Table 2-3 summarizes the characteristic strain rates in friction stir welding.

Table 2-3: Characteristic strain rates in the TMAZ/nugget region in friction stir welding.

First Author	Material	Method	Reported Strain rate
Jata [19]	AAXXXX	Measured	10
Masaki [42]	AA1050	Measured	1.7-2.7
Frigaard [43]	AA6082	Measured	1.6-10.3
Frigaard [43]	AA7108	Measured	1.7-17.3
Schmidt [10]	--	Modeled	1000
Nunes [9]	--	Modeled	100
Askari [45]	AAXXXX	Modeled	10-100
Darras [46]	AAXXXX	Modeled	100
Buffa [28]	AA6082-T6	Modeled	4-11
Nandan [6]	AA6061	Modeled	160
Colegrove [47]	AA7449	Modeled	500
Buffa [40]	AA7075	Modeled	7-8

It is apparent that there is much discrepancy over the magnitude of strain rate in FSW and the appropriate technique to predict strain rate distributions. Estimates of the effective strain rate vary from 1.7 to 1000 s^{-1}. While the majority report strain rates below 160 s^{-1}, a few report higher values from numerical modeling.

2.4 Modeling Discrepancies

Peak temperatures in the nugget have been reported between 0.7 and 0.98 times the absolute melting temperature of the material. Peak strains have been reported between 5 and 80 and strain rates between 1.7 and 1000 s^{-1}. These discrepancies in temperature, strain, and strain rate can occur between measured and modeled data, as well as between models performed by different authors.

Hamilton et al. [12] reported maximum measured temperatures in the nugget of 0.98 times the absolute melting temperature of the material, while Buffa and Fratini [31] report maximum temperatures as low as 0.70 time the absolute melting temperature of the material from their friction stir weld simulations. Temperatures predicted by Bastier et al. [29] are reported as high as the absolute melting temperature of the material.

While none of the reported values for maximum strain were measured results, there is discrepancy between the predicted values. Zhang and Chen [41] predict maximum strain values of 5.2; however, Heurtier et al. [5] predict a maximum strain value of 80.

Frigaard et al. [43] reported measured strain rates between 1.7 and 17.3 s^{-1}, while Schmidt and Hattel [10] predicted strain rates of 1000 s^{-1} using a numerical model. Modeled strain rates reported by Nandan et al. [6] are only 160 s^{-1}.

There are several reasons for discrepancies in maximum strains, strain rates, and temperatures reported from model predictions. Parameters that may account for discrepancies that are not inherent results of modeling are materials and weld parameters such as the rotational speed of the tool or the traverse speed of the plate. However, there are several parameters that are specific to the model itself.

Boundary conditions and heat transfer properties are variables specific to a model. Because these variables are unknown, estimations must be made to compute their values. For example, although the heat transfer between the workpiece and the backing plate is conduction, the heat transfer is often modeled as convection with an experimentally determined convection heat transfer coefficient [3].

Constitutive law is also a model specific variable that may account for discrepancies in predicted temperatures, strains, and strain rates. This parameter will be the focus of this paper. Several constitutive laws used to model FSW will be introduced and their validity across the weld will be evaluated.

2.5 Constitutive Laws used in FSW Modeling

FSW modelers have used a variety of constitutive laws to characterize material behavior. Table 2-4 summarizes constitutive laws used in FSW with their corresponding references. The constitutive laws have been characterized as path-independent or path-dependent.

Table 2-4: Summary of constitutive laws used to characterize material behavior in FSW modeling.

Constitutive Law	Path Dependence	References
Sellars and Tegart	Independent	[6, 29, 49-54]
Johnson-Cook	Independent	[44, 45]
Buffa	Independent	[55]
Zhang and Chen	Independent	[41]
Heurtier	Independent	[14]
Arbegast	Independent	[56]
Saturated Hart Model	Independent	[57]
Modified Hart Model	Dependent	[8]

The majority of the constitutive laws currently used to model FSW are path-independent. Path-independent constitutive laws use only the current processing conditions to determine flow

stress. Path-dependent constitutive laws account for the full thermomechanical history of the material. Kocks and Mecking have demonstrated that the use of path-independent constitutive laws to characterize flow stress under variable temperature and strain rate conditions can lead to inaccurate predictions [58]. This idea will be discussed in more detail in Chapter 3.

2.5.1 Path-Independent Equations used in FSW Modeling

The following discussion describes primarily the parametric equations of path-independent constitutive laws used to model FSW. If information on the process to determine constants is available, it will be discussed. If no discussion on constants is presented, then no information was provided in the literature.

2.5.1.1 Sellars and Tegart/Sheppard and Wright Law

The Sellars and Tegart/Sheppard and Wright law treats the material as an incompressible viscous non-Newtonian fluid [59, 60]:

$$\sigma = \frac{1}{\alpha}\sinh^{-1}\left[\left(\frac{Z}{A}\right)^{1/n}\right] = \frac{1}{\alpha}\ln\left\{\left(\frac{Z}{A}\right)^{1/n} + \left[1 + \left(\frac{Z}{A}\right)^{2/n}\right]^{1/2}\right\} \quad \textbf{(2-1)}$$

$$Z = \dot{\varepsilon}\exp\left(\frac{Q}{RT}\right) \quad \textbf{(2-2)}$$

where Z is the Zener-Hollomon parameter or temperature compensated strain rate, and Q is the apparent activation energy.

A, α, Q, and n are determined from hot compression and torsion tests. Material constants generally used are those determined by Sheppard and Jackson for aluminum alloys [61].

The Sellars and Tegart law modified by Sheppard and Wright has the advantages of availability of material constants for aluminum alloys and ease of implementation in commercial codes.

2.5.1.2 Johnson-Cook Plasticity Law

The Johnson-Cook plasticity law is a multiplicative law. The Johnson-Cook law for the von Mises flow stress is [62]:

$$\sigma = [A + B\varepsilon^{n}][1 + C\ln\dot{\varepsilon}^{*}][1 - T^{*m}] \quad \textbf{(2-3)}$$

$$T^{*} = \frac{T - T_{ROOM}}{T_{MELT} - T_{ROOM}} \quad \textbf{(2-4)}$$

where $\dot{\varepsilon}^{*} = \dot{\varepsilon}/\dot{\varepsilon}_0$ is the dimensionless strain rate and $\dot{\varepsilon}_0$=1.0 s^{-1}. *A* is the room temperature yield stress of the material. *B* and *n* are representative of the effects of strain hardening. *C* is the strain rate hardening coefficient, and *m* is the thermal softening exponent.

The Johnson-Cook law requires experimental data over a broad range of strains, strain rates, and temperatures to determine constants that capture the effects of strain, strain rate, and temperature. Torsion and tensile data at room temperature and constant strain rate, Hopkinson bar tests run at various temperatures, and torsion and tensile data over a wide range of strain rates and various strain levels are required to determine the strain, thermal, and strain rate sensitivities, respectively [62].

This law can be fit over a wide range of strain, strain rate, and temperature. Several materials, each with its own set of constants, can be characterized by the Johnson-Cook law. However, accuracy for a particular material may be sacrificed for this versatility [62].

2.5.1.3 Buffa Law

A common form of a multiplicative exponential law including strain, strain rate, and temperature sensitivity is [55]:

$$\sigma = KT^{A}\dot{\varepsilon}^{B}\varepsilon^{C} \quad \textbf{(2-5)}$$

where *A*, *B*, and *C* represent the thermal, strain rate, and strain sensitivities, respectively. This form can easily be modified to neglect strain hardening by setting *C*=0.

2.5.1.4 Zhang and Chen Law

Zhang and Chen proposed a mixed exponential law shown in Equation 2-6 [41].

$$\sigma = \sigma_0(T) + \eta(\varepsilon)^{n}(\dot{\varepsilon})^{m} \quad \textbf{(2-6)}$$

In this form, the temperature sensitivity of the material is separated from the strain and strain rate sensitivities. $\sigma_0(T)$ is the current yield stress which is a function of temperature, *m* is the viscosity exponent, *n* is the strain hardening exponent, and η is the viscosity coefficient.

If *n*=0, then strain hardening is neglected and the resultant law represents a strain rate hardening/softening model. If *m*=0, then the law is rate independent.

This equation can be transformed to a perfectly plastic model when η=0. If η>0, then the material is in a state of strain rate hardening, but if η<0, then the material is in a state of strain rate softening.

2.5.1.5 Heurtier Law

Heurtier et al. proposed a multiplicative exponential law with the Zener-Hollomon parameter shown in Equation 2-7 [14].

$$\sigma = KZ^{m} \quad \textbf{(2-7)}$$

K and *m* are constants determined by means of conventional torsion testing.

2.5.1.6 Arbegast Law

Arbegast proposed a multiplicative polynomial exponential law shown in Equations 2-8 through 2-10 [56].

$$\sigma_{0.1} = \exp(b)\exp(mT) \quad \textbf{(2-8)}$$

$$m = m_1\dot{\varepsilon}^2 + m_2\dot{\varepsilon} + m_3 \quad \textbf{(2-9)}$$

$$b = b_1\dot{\varepsilon}^2 + b_2\dot{\varepsilon} + b_3 \quad \textbf{(2-10)}$$

where $\sigma_{0.1}$ is the flow stress at a strain level of 0.1 and *b* and *m* are determined experimentally from hot compression experiments. All flow stress values are taken at a strain level of 0.10 to ensure the flow stress is in the plastic region.

2.5.1.7 Saturated Hart Model

The saturated Hart model developed by Nandan et al. [57] uses the flow stress from the modified Hart model, but has no hardness evolution, as the saturation value of the hardness is used throughout the entire deformation process.

2.5.2 Path-Dependent Equations used in FSW Modeling

Currently, only one path-dependent constitutive law, namely a modified Hart model developed by Cho et al. [8], has been reported in FSW models. However, the use of a second path-dependent law developed by Kocks and Mecking [58] is investigated in this paper.

2.5.2.1 Modified Hart Model

The modified Hart model consists of one master curve and an explicit equation for flow stress as a function of strain rate, temperature, and hardness.

The flow stress and strain rate at any stage of deformation history characterize the current strength or hardness of the material. The Hart model refers to the $\sigma(\dot{\varepsilon})$ characteristic at any level of strain hardening as the current hardness curve for the specimen. Each state, as characterized by its unique hardness curve, is referred to as a hardness state. Hardness as defined in the modified Hart model is a state variable that governs flow stress; it is not the yield stress [63].

Dynamic intermittent load relaxation tests with very little plastic strain are used to measure σ-$\dot{\varepsilon}$ characteristics at a fixed level of hardness. This test is capable of generating reliable data over as much as seven decades of strain rate in a single run.

A master curve is a single curve that can be used to represent all hardness states. The master hardness curve can generate all hardness curves by rigid translation along a straight line with slope β where $1/\beta$ is comparable in value to the high temperature creep exponent for the material [63] (Figure 2-2). The hardness (κ) is evolved, while flow stress is a function of hardness and strain rate.

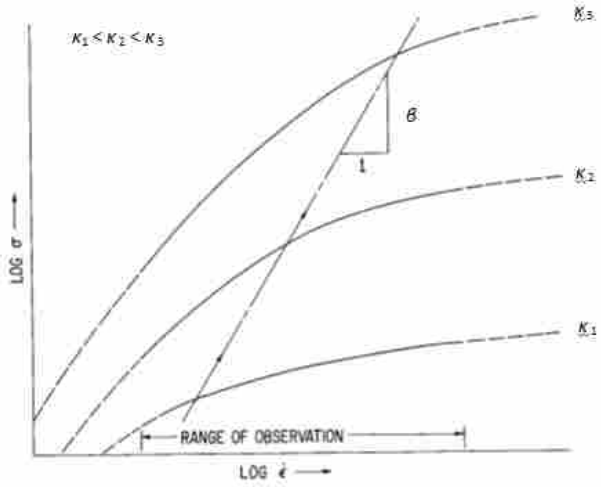

Figure 2-2: A schematic of the scaling of stress and strain rate with change of hardness (κ). A single master curve is shown displaced to several positions in the direction shown by the diagonal line. The observed hardness curves at each level of hardness appear in the strain rate segment labeled "range of observation" [63].

The explicit flow stress equation for the modified Hart model is a function of strain rate, temperature and hardness [8].

$$\sigma = \kappa \exp\left[-\left(\frac{b}{\dot{\varepsilon}}\right)^{\lambda}\right] + G\left(\frac{\dot{\varepsilon}}{a}\right)^{1/M} \quad \textbf{(2-12)}$$

$$a = a_0 \exp\left[\frac{-Q\prime}{RT}\right] \quad \textbf{(2-13)}$$

$$b = b_0\left(\frac{\kappa}{G}\right)^{N} \exp\left[\frac{-Q}{RT}\right] \quad \textbf{(2-14)}$$

where κ is the hardness, and *G, Q, Q', M, N, λ, b_0,* and a_0 are material model parameters.

The hardness evolution equation with a Voce-like saturation limit, κ^{sat} is a function of temperature and strain rate [8].

$$\kappa^{sat} = \left(\frac{C}{\varphi}\right)^{m_0} \quad \textbf{(2-15)}$$

$$\varphi = T\ln\left(\frac{D_0}{\dot{\varepsilon}}\right) \quad \textbf{(2-16)}$$

$$\frac{D}{Dt}(\kappa) = h_0\left(1 - \frac{\kappa}{\kappa^{sat}}\right)^{n_0} \dot{\varepsilon} \quad \textbf{(2-17)}$$

The initial state of the material is determined by the initial hardness. *C*, m_0, D_0, h_0, and n_0 are material constants.

Cho et al. [8] determined constants for annealed 304 stainless steel using data from large deformation tests for the flow stress equations and compression testing at various strain rates and temperatures for the hardness evolution equations.

Material behavior at high temperature and strain rate can be predicted by experiments at low temperature and strain rate. As a result, characteristic curves over extended temperatures and strain rates can be extrapolated from experimental data.

2.5.2.2 Kocks and Mecking Model

The Kocks and Mecking model consists of two master curves and one implicit equation [58]. The first master curve characterizes the hardening rate which is defined as:

$$\Theta = \frac{d\sigma}{d\varepsilon} \quad \textbf{(2-18)}$$

when temperature and strain rate are held constant (Figure 2-3(a)). A plot of hardening rate versus stress for several combinations of temperature and strain rate can be normalized to collapse the data onto one master curve (Figure 2-3(b)). The hardening rate is normalized by the temperature dependent shear modulus (μ), and the stress is normalized by the Voce stress (σ_V) as seen in Figure 2-3(b).

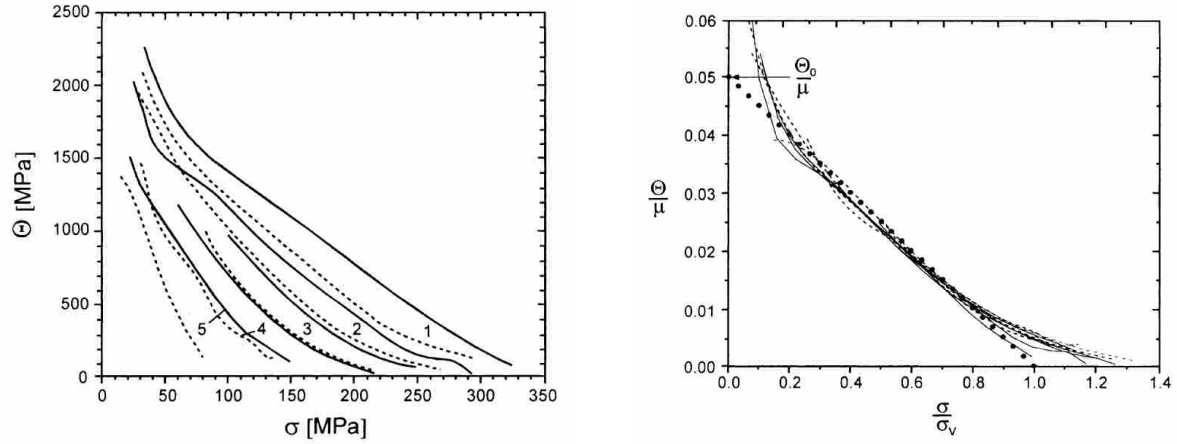

(a) **(b)**

Figure 2-3: (a) Differentiated stress strain curves at various combinations of temperature and strain rate are normalized to produce (b) the hardening rate master curve [58].

The flow stress is represented implicitly by a Voce approximation to the hardening rate.

$$\frac{\Theta}{\Theta_0} = \left(1 - \frac{\sigma}{\sigma_V}\right) \quad \textbf{(2-19)}$$

Θ_0 is the initial hardening rate and σ_V is the scaling or Voce stress which is a function of temperature and strain rate.

The initial state of the material is determined by the flow stress at the initial strain rate and temperature and zero plastic strain.

A master curve for Voce stress as a function of temperature and strain rate can be approximated by Equation 2-20.

$$\frac{\sigma_V}{\mu} = \frac{\sigma_{V0}}{\mu_0}\left\{1 - \left(\frac{1}{g_0}\frac{kT}{\mu b^3}\ln\frac{\dot{\varepsilon}_0}{\dot{\varepsilon}}\right)^p\right\}^q \quad \textbf{(2-20)}$$

μ is the temperature dependent shear modulus, k is the Boltzmann constant, b is the magnitude of the Burgers vector, and $\dot{\varepsilon}_0$ is a constant on the order of magnitude of 10^7 s^{-1}. For pure fcc materials p = ½ and q = 2 as shown in Figure 2-4.

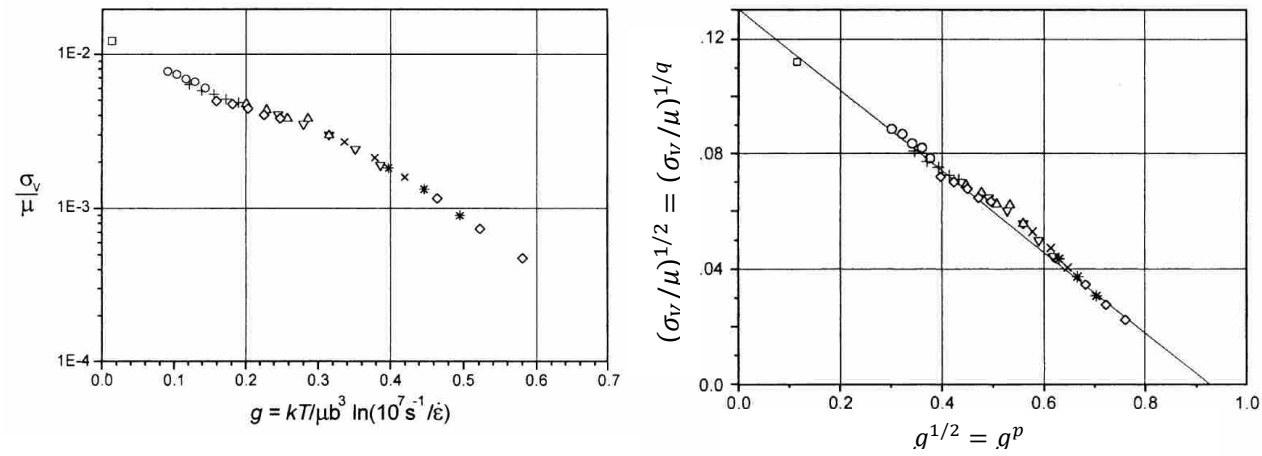

Figure 2-4: Normalized Voce stress as a function of temperature and strain rate (left). Same as figure on left but with coordinates according to Equation 2-20 for pure fcc materials (right) [58].

The most basic consequence of thermal activation control is that the temperature and strain rate dependencies are coupled in a way that preserves the behavior when temperature or strain rate are varied such that the normalized activation energy $g = \frac{kT}{\mu b^3}\ln\left(\frac{\dot{\varepsilon}_0}{\dot{\varepsilon}}\right)$ is within the experimental range. Thus, the use of g expands the range of temperature and strain rate over which the constants are valid for any material (Figure 2-5). The rectangle represents the range of

temperature and strain rate over which the constants were determined, and the contours represent lines of constant *g*. Any combination of temperature and strain rate which results in a *g* value that passes through the box is actually an interpolation point in activation energy.

Master curves capture flow stress data from a wide range of strain rates and temperatures. Figure 2-3 and Figure 2-4 represent strain rates and temperatures ranging from 10^{-4} to 1 s^{-1} and room temperature to 400 °C, respectively.

All constants and relationships can be determined from uniaxial deformation, commonly compression testing, at various combinations of constant strain rate and temperature. Thus, data at constant strain rate and temperature can be applied to any variable path.

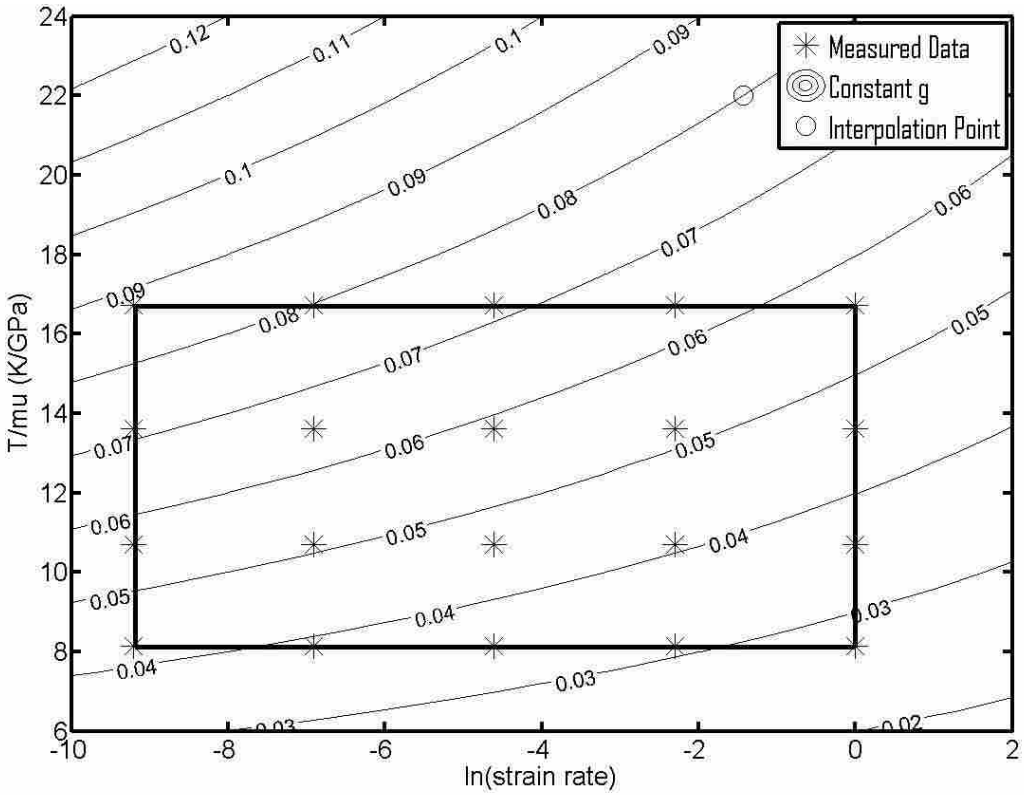

Figure 2-5: Visual representation of interpolation in *g*. The box on the plot represents the experimental range of temperature and strain rate over which constants were determined.

2.6 Evaluation of Path-Independent Constitutive Laws used in FSW

The constants for each path-independent constitutive law mentioned are a fit to experimental data. The goodness of fit is known only for the ranges of strains, strain rates, and temperatures over which the constants were determined. The intention of this evaluation is to compare these ranges with those encountered in FSW. If conditions present in FSW lie outside of the ranges over which the constants were determined, then the validity of the constitutive law is undemonstrated under these conditions and use of the law requires extrapolation.

The validity of the Johnson-Cook constants used by Schmidt and Hattel [44] is undemonstrated in the nugget region and possibly a portion of the TMAZ due to limitations in the strain over which the constants are determined. The constants are limited to strains under 0.4.

The validity of the Sellars and Tegart constants for aluminum alloys used by several authors [6, 29, 50-53] is undemonstrated in the portion of the TMAZ which has strains less than saturation values and in the nugget when peak temperatures exceed 440 °C.

The validity of the constants for the constitutive law proposed by Arbegast [56] is unknown in the nugget where strain values exceed 0.1, temperatures exceed $0.8T_m$, and strain rates exceed 1 s^{-1}.

The validity of the constants for the saturated Hart model proposed by Nandan et al. [57] is undemonstrated in the TMAZ and nugget regions. Constants were determined over a variety of temperatures and strain rates, but no exact ranges were reported. The validity of the constants is not limited by strain in the nugget and possibly a portion of the TMAZ where strains are saturated.

Constants for constitutive laws proposed by Askari et al. [45], Ulysse [49], Buffa et al. [55], Zhang and Chen [41], and Heurtier et al. [14] cannot be evaluated according to the zones in a typical FSW weld without knowledge of the ranges of strain, strain rate, and temperature over which they were developed.

Table 2-5 summarizes the constants used by FSW modelers and the regions in which they have been demonstrated valid.

Table 2-5: Summary of validity of constants used by FSW modelers and their associated limitations in modeling typical zones of a FSW.

Reference(s)	Constitutive Law	Constants	Temperature	Strain Rate (s^{-1})	Strain	TMAZ	Nugget
[44]	Johnson-Cook	Lesuer [64]	RT-0.95T_m [65]	0.088-123 [65]	0-0.4 [65]	May have $\varepsilon > 0.4$	$\varepsilon > 0.4$
[45]	Johnson-Cook	Not Reported	Not Reported	Not Reported	Not Reported	Unknown	Unknown
[6, 29, 50-53]	Sellars and Tegart	Sheppard and Jackson [61]	RT-440 °C [61]	0-100 [61]	Assumed Saturated	$\varepsilon <$ Saturation	May have T > 440 °C
[49]	Sellars and Tegart	Not Reported	Not Reported	Not Reported	Assumed Saturated	Unknown	Unknown
[54]	Sellars and Tegart	Kozlowski [66]	850-1400 °C [67, 68]	5.5E-4-2.3E-2 [67, 68]	Assumed Saturated	T < 850 °C $\dot{\varepsilon} >>$ 2E-2	May have T < 850 °C
[55]	Buffa	Buffa et al. [55]	Not Reported	Not Reported	Not Reported	Unknown	Unknown
[41]	Zhang and Chen	Not Reported	Not Reported	Not Reported	Not Reported	Unknown	Unknown
[14]	Heurtier	Heurtier et al. [14]	Not Reported	Not Reported	Not Reported	Unknown	Unknown
[56]	Arbegast	Arbegast [56]	0.6-0.8T_m	0.3-1.1	0.1	None	$\varepsilon > 0.1$ T > 0.8T_m $\dot{\varepsilon} > 1.1$
[57]	Saturated Hart Model	Cho et al. [8]	Variety [69, 70]	Variety [69, 70]	Assumed Saturated	$\varepsilon <$ Saturation	Unknown

A constitutive law that is not valid over the entire weld may be valid over certain zones. The development of a numerical model capable of accurately determining the distribution of

strain, strain rate, and temperature throughout the zones in a typical FSW weld is essential to a complete evaluation of existing constitutive laws.

2.7 Comparison of Constitutive Laws in FSW Modeling

In order to evaluate the effect of constitutive laws in FSW modeling, Hickory, a two-dimensional fiction stir welding model developed by the Deformation Process Simulation Laboratory research group at Cornell [71], was modified by the author to include the Sellars and Tegart, Johnson-Cook, and Kocks and Mecking laws. Appendix A describes the changes made to the source code to implement the constitutive laws.

The Hickory model has been used and reported in the literature, and the boundary conditions are consistent with those used by Cho et al. [8]. Material constants were determined for AA 5083 for the three laws from constant strain rate and temperature compression data found in the Atlas of Formability [72] as described in Chapter 3, and the material laws have been demonstrated under conditions typical of portions of the weld. The predicted temperature data is reasonable in comparison to values reported in the literature.

No attempt has been made to adjust parameters to match experimental data. The focus of this evaluation is only to investigate the effects of constitutive laws on model predictions.

The weld was simulated at 600 RPM and 3 ipm. Simulations were performed holding all parameters constant while changing only the constitutive law.

Figure 2-6 is a schematic showing weld direction, rotation direction, and advancing and retreating sides of the weld.

Figure 2-7, Figure 2-8, Figure 2-9, and Figure 2-10 display the resultant temperatures in Kelvin, strains, strain rates, and flow stress values in MPa for each constitutive law as well as pair-wise comparisons between the three laws, respectively.

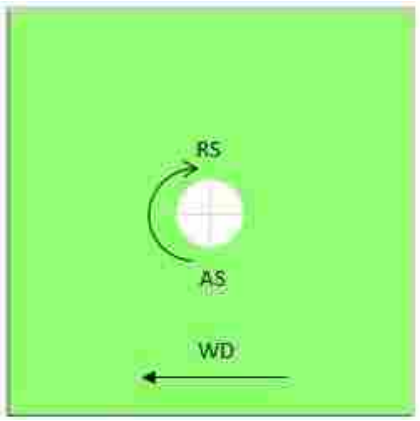

Figure 2-6: Schematic showing weld direction (WD), rotation direction, advancing side (AS), and retreating side (RS) of the weld.

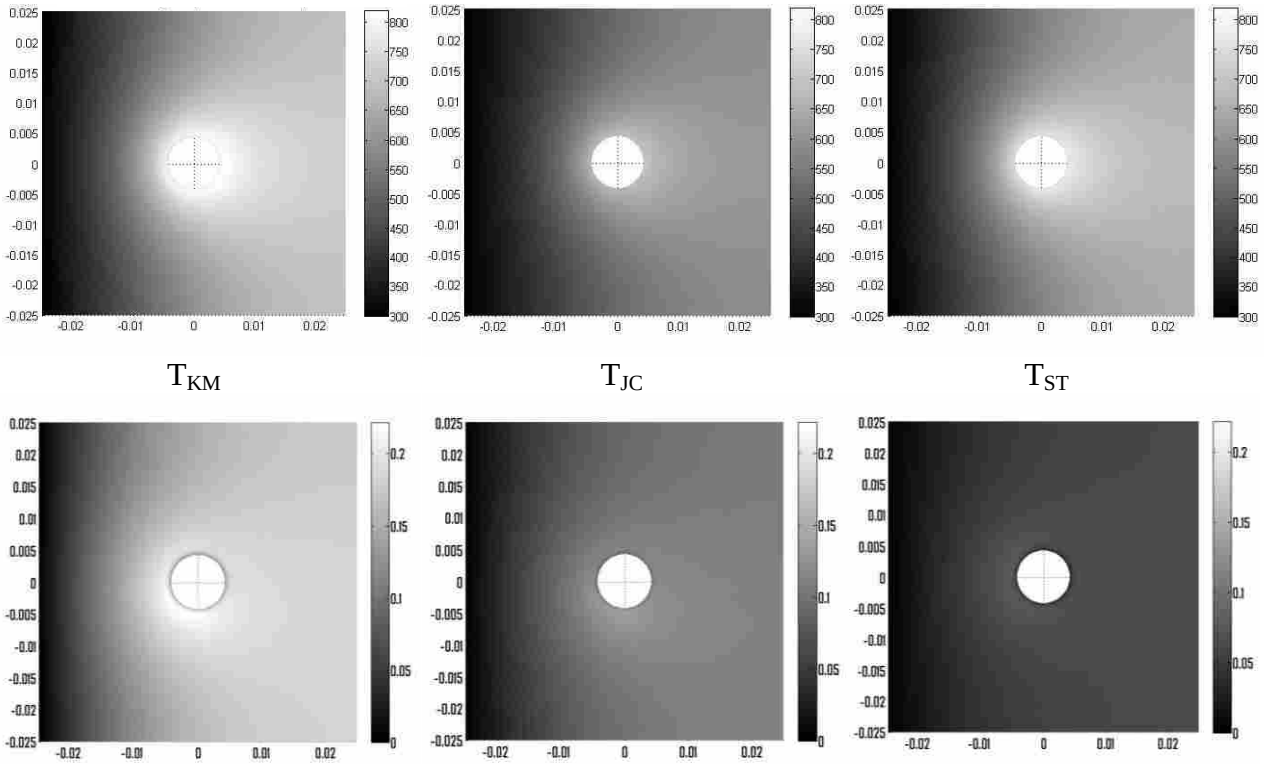

T_{KM} T_{JC} T_{ST}

$\frac{T_{KM} - T_{JC}}{T_{JC}}$ $\frac{T_{ST} - T_{JC}}{T_{JC}}$ $\frac{T_{KM} - T_{ST}}{T_{ST}}$

Figure 2-7: Comparison of temperature data for a Hickory FSW simulation for Kocks and Mecking (T_{KM}), Johnson-Cook (T_{JC}), and Sellars and Tegart (T_{ST}).

The maximum temperatures predicted for the Sellars and Tegart, Johnson-Cook, and Kocks and Mecking models are 762, 680, and 821 K, respectively. The maximum temperature difference seen is between Kocks and Mecking and Johnson-Cook where the difference in peak temperature is over 140 K, which is a 21% difference when referenced to the Johnson-Cook constitutive law. The maximum difference between Kocks and Mecking and Sellars and Tegart is the smallest of the three pairwise comparisons at only 7.8%. The results displayed in Figure 2-7 demonstrate that the constitutive law alone can cause significant quantitative differences in peak temperatures modeled in friction stir welding.

Qualitative differences in peak temperature can also be deduced from Figure 2-7. The peak difference in temperature between the Kocks and Mecking and Sellars and Tegart laws occurs on the leading edge of the tool. However, the peak differences in the remaining pairwise comparisons occur near the pin on the advancing side of the weld. This indicates that changing the constitutive law results in a different temperature profile.

The peak strain values predicted for the Sellars and Tegart, Johnson-Cook, and Kocks and mecking laws are 109, 230, and 101, respectively. The maximum strain differences occur in the wake of the pin on the advancing side of the tool (Figure 2-8). While all three constitutive laws predict similar strain profiles, the Johnson-Cook law predicts strain values over twice as large as those for the Sellars and Tegart and Kocks and Mecking laws. The high strain values predicted by the Johnson-Cook law are a cause for concern as the Johnson-Cook law is not valid at high strains where the material has saturated; however, the Sellars and Tegart and Kocks and Mecking models do accomodate saturation at large strains.

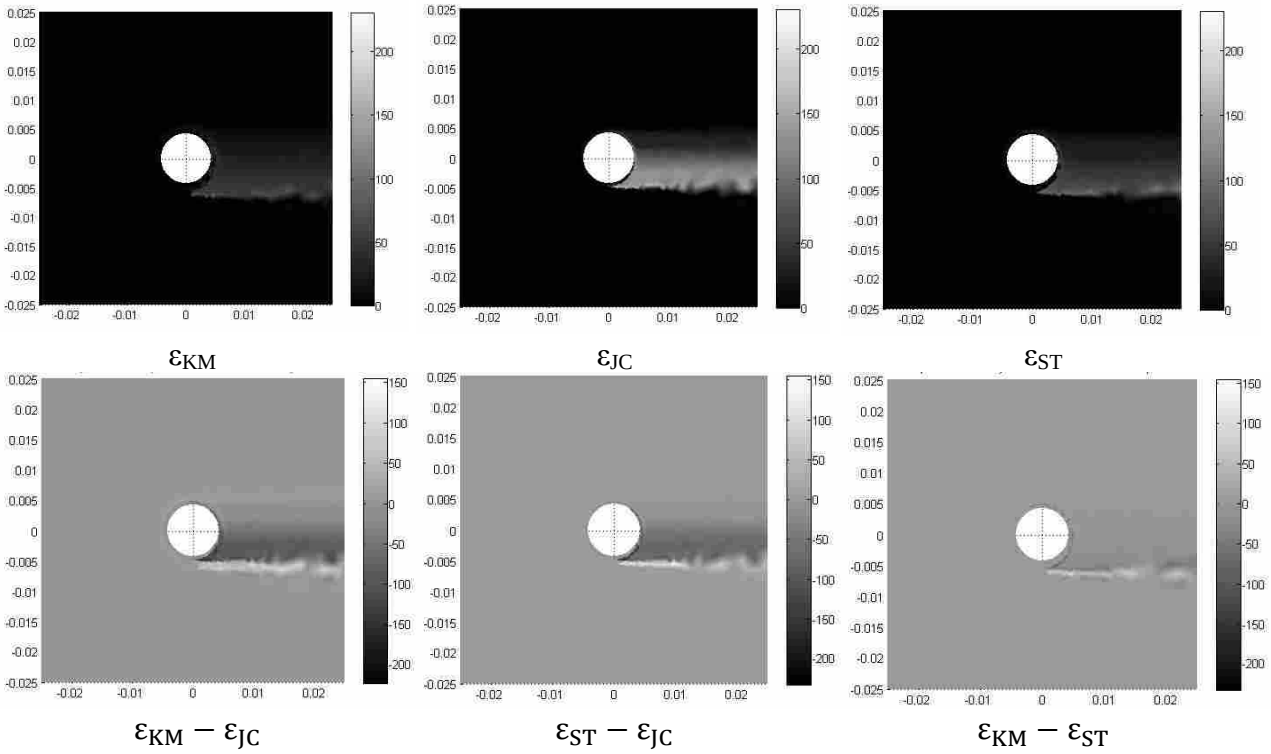

Figure 2-8: Comparison of strain data for a Hickory FSW simulation for Kocks and Mecking (ε_{KM}), Johnson-Cook (ε_{JC}), and Sellars and Tegart (ε_{ST}).

The peak strain rate values predicted for the Sellars and Tegart, Johnson-Cook, and Kocks and Mecking laws are 613, 924, and 348 s^{-1}, respectively. The maximum strain rates as well as strain rate differences occur at the pin (Figure 2-9). The Johnson-Cook law predicts strain rate values more than two and a half times larger than those for the Kocks and Mecking law. The large strain rates may be attributed to uncertainty in boundary conditions at the pin in the finite element model.

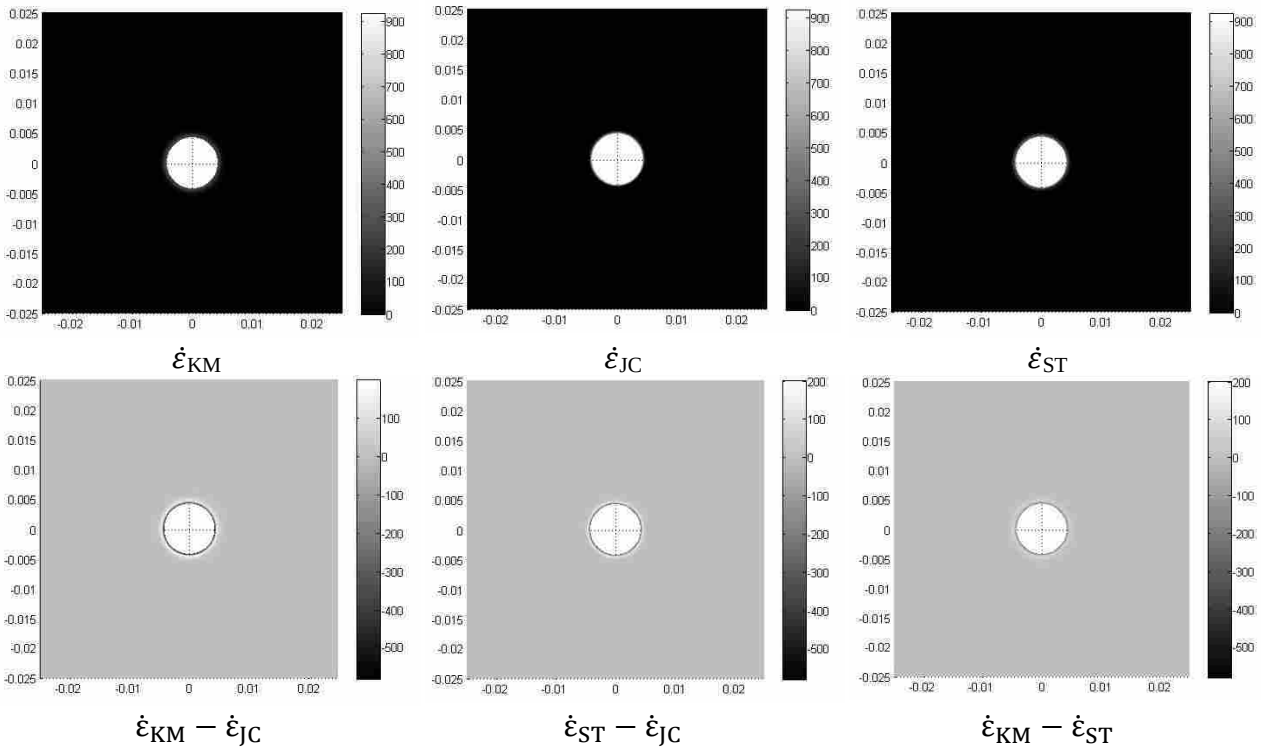

Figure 2-9: Comparison of strain rate data for a Hickory FSW simulation for Kocks and Mecking ($\dot{\varepsilon}_{KM}$), Johnson-Cook ($\dot{\varepsilon}_{JC}$), and Sellars and Tegart ($\dot{\varepsilon}_{ST}$).

The peak flow stress values for the Sellars and Tegart, Johnson-Cook, and Kocks and Mecking models are 164, 150, and 179 MPa, respectively. The Kocks and Mecking law predicts flow stress values 20% larger than those for the Johnson-Cook law. The flow stress profiles are also affected by constitutive law (Figure 2-10). The difference in flow stress values between the Sellars and Tegart and Kocks and Mecking models is highest a small distance outside of the pin where strains lower. The Kocks and Mecking model is able to predict strain hardening at low strains; however, the Sellars and Tegart law can only predict saturation values due to its strain independence.

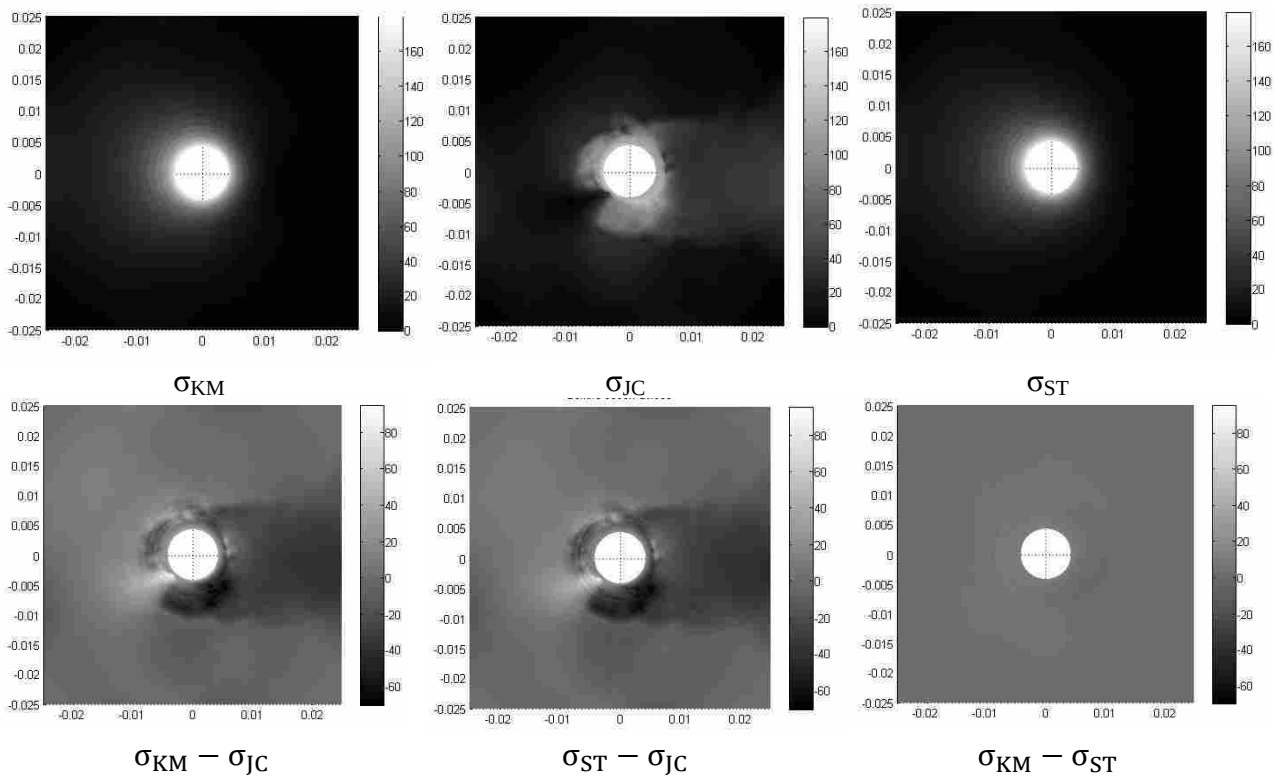

Figure 2-10: Comparison of flow stress data for a Hickory FSW simulation for Kocks and Mecking (σ_{KM}), Johnson-Cook (σ_{JC}), and Sellars and Tegart (σ_{ST}).

The Johnson-Cook law predicts higher flow stress values than both the Sellars and Tegart and Kocks and Mecking laws around the pin where strains are high. The Johnson-Cook law is unable to predict saturation; however, both the Sellars and Tegart and Kocks and Mecking models can predict saturation.

Table 2-6 summarizes the peak temperatures, strains, strain rates, and flow stress values predicted by each constitutive law.

Table 2-6: Peak values predicted by Hickory for each constitutive law.

Constitutive Law	Peak Temperature (K)	Peak Strain	Peak Strain Rate (s^{-1})	Peak Flow Stress (MPa)
Sellars and Tegart	762	109	613	164
Johnson-Cook	680	230	924	150
Kocks and Mecking	821	101	348	179

The differences in peak values for temperature, strain, strain rate, and flow stress as well as the differences in profiles for these parameters discussed previously indicate that the constitutive law does have a significant effect on model predictions for friction stir welding.

2.8 Conclusions

The peak temperatures involved in friction stir welding range from 0.6 and 0.95 times the absolute melting temperature of the material. Strain rates have been reported from 0 to 160 s^{-1}, and strain values range from 0 to a maximum value of 80 in a limited volume of the weld. None of the path-independent laws evaluated in this paper have been demonstrated valid over the entire range of strain, strain rate, and temperature in friction stir welding.

The Sellars and Tegart/Sheppard and Wright and saturated Hart laws, are strain insensitive. This simplification may be justified in the highest strain regions where the stress has been saturated, such as the stir zone.

Strains in the nugget and possibly a portion of the TMAZ are higher than those over which the Johnson-Cook constants used by Schmidt and Hattel [44] were determined.

Temperatures in the nugget exceed those over which the constants for the Sellars and Tegart law for aluminum alloys used by several authors [6, 29, 50-53] were determined.

The nugget strain is outside the range of strains over which the constants for the constitutive law proposed by Arbegast [56] were determined.

Although constants for the saturated Hart model [57] were determined over a variety of temperatures and strain rates, no exact ranges were reported. Therefore, no evaluation of applicability could be made.

No information is given in the literature on the origin of the constants for constitutive laws used by Askari et al. [45], Ulysse [49], Buffa et al. [55], Zhang and Chen [41], and Heurtier et al. [14]. Therefore, no evaluation of the applicability could be made.

While holding all other parameters constant, changing the constitutive law in a FSW model can result in up to a 21% difference in peak temperature. Varying locations for maximum temperature differences indicate that a change in constitutive law may result in a change in predicted temperature profile. Predicted peak strains can vary by 130%, and predicted peak strain rates can vary by 166%. Differences in flow stress profiles indicate that different constitutive laws may have strengths in different areas of the weld. The Sellars and Tegart and Kocks and Mecking models are able to predict saturation at high strains which occur in the nugget region near the pin. The Johnson-Cook and Kocks and Mecking models are able to capture strain hardening which occurs a small distance from the pin in the thermomechanically affected zone.

Clearly, the choice of constitutive law is critical to accurate modeling of FSW. This paper has demonstrated that the applicability of a certain constitutive law to a given area of a friction stir weld should be carefully considered in addition to boundary condition issues when modeling FSW because no single constitutive law has been proven valid across the entire range of FSW phenomena.

3 A COMPARISON OF EXPERIMENTAL COMPRESSION DATA AND MODEL PREDICTIONS WITH CONSTITUTIVE LAWS USED TO MODEL FRICTION STIR WELDING

3.1 Abstract

Numerical modeling of friction stir welding is dependent on the constitutive law used to determine flow stress as a function of strain rate, temperature, and strain. The three constitutive laws analyzed in this paper are Sheppard and Wright, Johnson-Cook, and Kocks and Mecking. Material constants were determined for AA5083 for these laws from constant strain rate and temperature compression data found in the Atlas of Formability. Two-dimensional Lagrangian models of axial compression tests identical to source data tests were developed. The modeled stress-strain curves were compared with curves from the Atlas of Formability. Models of interrupted temperature and strain rate compression tests were also developed and compared to material behavior under similar conditions. This comparison was used to evaluate the implications of using each constitutive law to model friction stir welding.

The Sheppard and Wright law is capable of capturing saturation but incapable of capturing strain hardening with errors as large as 57% near yield. The Johnson-Cook law is capable of capturing strain hardening; however, its inability to capture saturation causes over-predictions of stress at large strains with errors as large as 37% near saturation. The Kocks and Mecking model is capable of capturing strain hardening and saturation with errors less than 5% over the entire range of plastic strain. The Sheppard and Wright and Johnson-Cook laws are

incapable of capturing transients characteristic of material behavior under interrupted temperature or strain rate. The use of a state variable in the Kocks and Mecking law allows it to predict such transients. The Sheppard and Wright law is valid in the nugget region where strains have reached saturation values. The Johnson-Cook law is valid in the thermomechanically affected zone near the heat affected zone when strains are moderate. The Kocks and Mecking model across the entire weld in friction stir welding.

3.2 Background

Friction stir welding (FSW) is a large strain, moderate- to high-strain rate, elevated-temperature deformation process. Strain values have been reported as high as 80 in a limited volume of the weld [5], strain rates can be as high as 160 s^{-1} [6], and temperatures can reach up to 95% of the absolute melting temperature of the material [7]. While exact values are uncertain, the strains, strain rates, and temperatures in FSW are higher than most metalworking processes.

Unlike conventional metalworking processes, such as rolling, which are isothermal and uniform strain rate, FSW is characterized by steep gradients in strain, strain rate, and temperature. Strain and strain rate go from zero to the maximum over a few millimeters, and temperature goes from zero to the maximum over a few centimeters. While various metalworking and joining models have been used to model FSW, the steep gradients in strain, strain rate, and temperature inherent in FSW potentially limit the accuracy of such models.

To develop accurate models of the friction stir welding process, a constitutive law which is valid throughout the entire weld is desirable. A constitutive law consists of a set of parametric equations that characterizes flow stress as a function of strain rate and temperature and accounts for the prior strain, strain rate, and temperature history of the material; and a set of constants determined to fit the parametric equations to the behavior of a given material.

Three constitutive laws, namely the Sellars and Tegart, Johnson-Cook, and Kocks and Mecking models are analyzed for AA 5083. Constants for the Kocks and Mecking model for AA 5083 have not been reported in the literature. A process for determining constants for the Kocks and Mecking model from Atlas of Formability data is described.

Constants for the Sellars and Tegart and Johnson-Cook laws will be determined from the same set of experimental data, and model predictions will be compared under constant temperature and strain rate as well as variable strain rate conditions. No comparison of these models, using the same source data, under variable strain rate conditions has been reported in the literature.

FSW models cannot be used to determine accuracy of constitutive laws due to model discrepancies such as boundary conditions and heat transfer properties. However, interrupted strain rate compression testing will partially assess the applicability of the constitutive laws because variable strain rates exist across a typical friction stir weld.

The Sellars and Tegart/Sheppard and Wright law treats the material as an incompressible viscous non-Newtonian fluid and neglects the effects of strain hardening [59, 60]:

$$\sigma_e = \frac{1}{\alpha}\sinh^{-1}\left[\left(\frac{Z}{A}\right)^{1/n}\right] = \frac{1}{\alpha}\ln\left\{\left(\frac{Z}{A}\right)^{1/n} + \left[1 + \left(\frac{Z}{A}\right)^{2/n}\right]^{1/2}\right\} \quad \textbf{(3-1)}$$

$$Z = \dot{\varepsilon}\exp\left(\frac{Q}{RT}\right) \quad \textbf{(3-2)}$$

where σ_e is the effective stress, Z is the Zener-Hollomon parameter or temperature compensated strain rate, Q is the activation free energy, and R is the universal gas constant.

A, α, Q, and n are determined from hot compression and torsion tests. Material constants generally used are those determined by Sheppard and Jackson for aluminum alloys [61].

The advantages of the Sellars and Tegart law modified by Sheppard and Wright are availability of material constants and ease of implementation in commercial codes.

The Johnson-Cook plasticity law is a multiplicative law which includes the effects of strain, strain rate, and temperature. The Johnson-Cook law for the von Mises flow stress is [62]:

$$\sigma = [A + B\varepsilon^n][1 + C\ln\dot{\varepsilon}^*][1 - T^{*m}] \quad \textbf{(3-3)}$$

$$T^* = \frac{T - T_{ROOM}}{T_{MELT} - T_{ROOM}} \quad \textbf{(3-4)}$$

where ε is the equivalent plastic strain and $\dot{\varepsilon}^* = \dot{\varepsilon}/\dot{\varepsilon}_0$ is the dimensionless strain rate where $\dot{\varepsilon}_0$=1.0 s^{-1}. *A* is the room temperature yield stress of the material. *B* and *n* are representative of the effects of strain hardening. *C* is the strain rate hardening coefficient, and m is the thermal softening exponent.

The Johnson-Cook law requires a large and diverse amount of experimental data to determine constants that capture the effects of strain, strain rate, and temperature. Torsion and tensile data at room temperature and constant strain rate, Hopkinson bar tests run at various temperatures, and torsion and tensile data over a wide range of strain rates and various strain levels are required to determine the strain, thermal, and strain rate sensitivities, respectively [62].

This law can be fit over a wide range of strain, strain rate, and temperature. Several materials, each with its own set of constants, can be characterized by the Johnson-Cook law. However, accuracy for a particular material may be sacrificed for this versatility [62].

The Kocks and Mecking model consists of three master curves and one implicit equation [58, 73]. The first master curve characterizes the hardening rate which is defined as:

$$\Theta = \frac{d\sigma}{d\varepsilon} \quad \textbf{(3-5)}$$

when temperature and strain rate are held constant. A plot of hardening rate versus stress for several combinations of temperature and strain rate can be normalized to collapse the data onto one master curve.

The flow stress is represented implicitly by a Voce approximation, a linear representation of hardening rate versus stress which crosses the stress axis at the saturation or Voce stress, to the hardening rate.

$$\frac{\Theta}{\mu} = \left(\frac{\Theta}{\mu}\right)_0 \left(1 - \left[\frac{\sigma/\sigma_Y}{\sigma_V/\sigma_Y}\right]\right) \quad \textbf{(3-6)}$$

Θ_0 is the initial hardening rate, $\left[\frac{\sigma}{\sigma_Y}\right]$ is the state variable (s), $\left[\frac{\sigma_V}{\sigma_Y}\right]$ is the saturation value of the state variable (s^{sat}), and σ_V and σ_Y are the scaling or Voce stress and yield stress, respectively, which are both functions of temperature and strain rate.

Master curves for Voce stress and yield stress as a function of temperature and strain rate can be approximated by Equations 3-7 and 3-8.

$$\frac{\sigma_V}{\mu} = \frac{\sigma_{V0}}{\mu_0}\left\{1 - \left(\frac{1}{g_0}\frac{kT}{\mu b^3}\ln\frac{\dot{\varepsilon}_0}{\dot{\varepsilon}}\right)^p\right\}^q \quad \textbf{(3-7)}$$

$$\frac{\sigma_y}{\mu} = \frac{\sigma_{y0}}{\mu_0}\left\{1 - \left(\frac{1}{g_y}\frac{kT}{\mu b^3}\ln\frac{\dot{\varepsilon}_0}{\dot{\varepsilon}}\right)^p\right\}^q \quad \textbf{(3-8)}$$

μ is the temperature dependent shear modulus, k is the Boltzmann constant, b is the magnitude of the Burgers vector, p and q are phenomenological parameters, and $\dot{\varepsilon}_0$ is a constant on the order of magnitude of 10^7 s^{-1}.

As a result of thermal activation control, material behavior is preserved when temperature or strain rate are varied such that the normalized activation energy $g = \frac{kT}{\mu b^3}\ln\left(\frac{\dot{\varepsilon}_0}{\dot{\varepsilon}}\right)$ is within the experimental range [73]. Thus, using the model outside the experimental range of strain rate and temperature used to determine the constants, but within the range of modeled activation energies, is not an extrapolation, but an interpolation in activation energy.

Master curves capture flow stress data from a wide range of strain rates and temperatures. All constants and relationships can be determined from uniaxial deformation, typically

compression testing, at various combinations of constant strain rate and temperature. Thus, data at constant strain rate and temperature can be applied to any variable path.

3.3 Method

3.3.1 Obtaining Model Constants

Data from axial compression tests having 24 combinations of temperature and strain rate were used to determine constants for three different constitutive laws for AA 5083. Temperatures and strain rates ranged from 200 to 500 °C and 0.01 to 5.0 s^{-1}, respectively. All experimental monotonic stress-strain curves were taken from the Atlas of Formability [72]. Figure 3-1 displays the combinations of temperature and strain rate used to create the models.

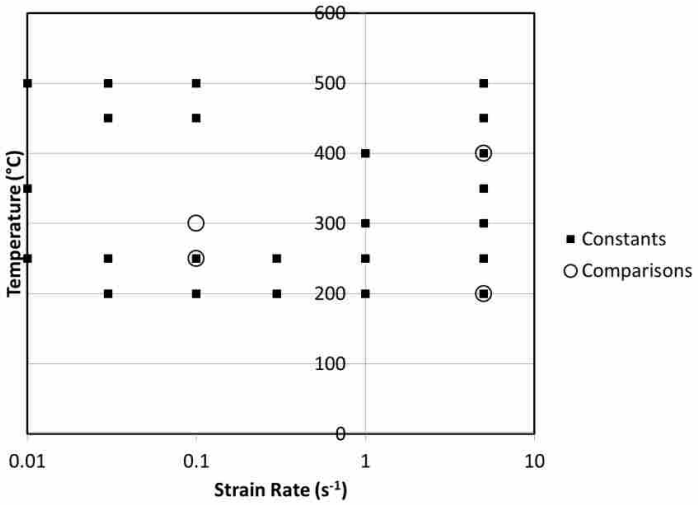

Figure 3-1: Curve usage from Atlas of Formability for each constitutive law.

For the Sellars and Tegart law, the method of least squares was used to determine constants A, α, n, and Q. The experimental value for effective stress was chosen as the saturation stress for each monotonic stress-strain curve.

For the Johnson-Cook law, the method of least squares was used to determined constants *A*, *B*, *n*, *C*, and *m*. Room temperature was defined as 297.15 K, and the absolute melting temperature for AA 5083 was defined as 847.15 K. The flow stress was fit along each monotonic stress-strain curve from yield to saturation. Data points were fit in strain increments of 0.005. The resulting number of points for each curve was nonconstant due to variation in final strain of the measured data.

For the Kocks and Mecking model, the shear modulus is needed as a function of temperature. Shear modulus was determined by a curve fit to the data presented by Mecking et al. [74].

The hardening rate master curve was determined by the following method. Hardening rate was normalized by the temperature-dependent shear modulus (μ) and plotted against stress which was normalized by a scaling stress (σ_V). Voce stress values were optimized until all hardening rate curves collapsed onto one master curve.

The scaling stresses determined by the Voce law were fit to a master curve as a function of temperature and strain rate. Voce stress normalized by temperature dependent shear modulus was plotted against activation energy, g. Equation 3-7 was fit to the data by changing the phenomenological parameters p and q and $\dot{\varepsilon}_0$ to maximize R^2.

While no master curve for yield stress has been reported in the literature, a relationship between yield stress and temperature and strain rate is needed to implement the Kocks and Mecking law. The yield stress (σ_Y) for each combination of temperature and strain rate was determined by shifting each $\Theta - \sigma$ curve along the abscissa by σ_Y until the normalized hardening rate curves recollapsed onto a new single master curve (as suggested by Kocks and Mecking [58]) (Figure 3-2).

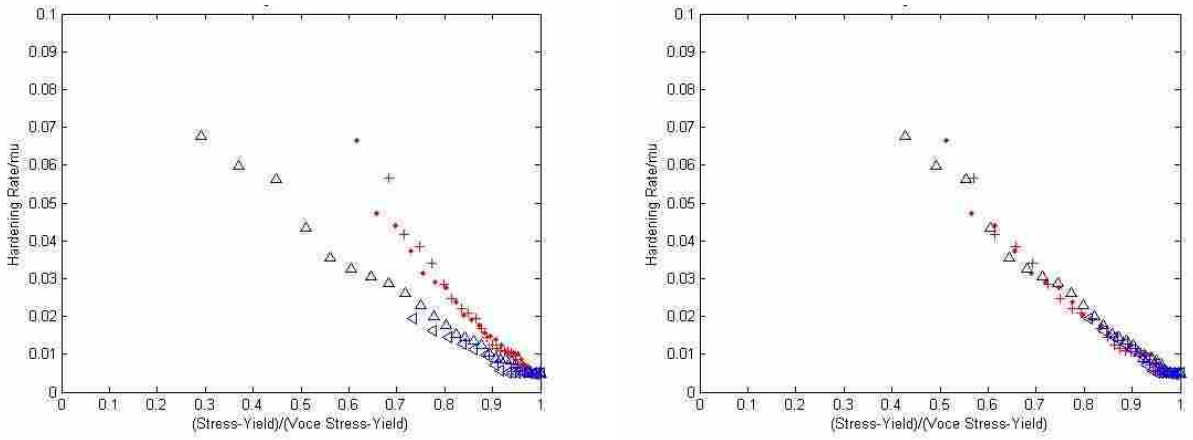

(a) **(b)**

Figure 3-2: (a) Hardening rate master curve before optimized yield shift. (b) Hardening rate master curve following yield shift.

The yield stresses determined by the optimized yield shift in Figure 3-2 were fit to a master curve as a function of temperature and strain rate. Yield stress normalized by temperature dependent shear modulus was plotted against activation energy, g. Equation 3-8 was fit to the data using the same phenomenological parameters p and q and $\dot{\varepsilon}_0$ used to fit Equation 3-7.

3.3.2 Determining Model Performance

Two-dimensional Lagrangian models of axial compression tests identical to source data tests were developed. In order to implement the Kocks and Mecking model, the initial state variable was set equal to 1, or yield. At the end of each time step, the hardening rate was used to calculate the stress for that time step. This stress was then used in conjunction with the corresponding values for yield stress to determine the state variable for the next time step.

Table 3-1 lists the combinations of temperature and strain rate evaluated in this paper. The curves evaluated were indicated on Figure 3-1.

Table 3-1: Temperature and strain rate combinations for each simulation.

Run	Temperature (°C)	Strain Rate (s^{-1})	Activation Energy (g)
1	250	0.1	0.2497
2	200	5	0.1721
3	300	0.1	0.2832
4	400	5	0.2820

3.4 Results and Discussion

The constants determined for the Sellars and Tegart, Johnson-Cook, and Kocks and Mecking laws are shown in Table 3-2, Table 3-3, and Table 3-4, respectively.

Table 3-2: Material constants for Sellars and Tegart law for AA 5083.

Parameter	Author's Value	Literature Value [6]
A	1.088E10 (s^{-1})	1.088E10 (s^{-1})
α	0.0522 (1/MPa)	0.015 (1/MPa)
n	1.499	4.99
Q	178037.07 (J/mol)	171400 (J/mol)

Table 3-3: Material constants for Johnson-Cook law for AA 5083.

Parameter	Author's Value	Literature Value [12]
A	237.127 (MPa)	270 (MPa)
B	254.125 (MPa)	470 (MPa)
n	0.2692	0.6
C	0.0377	0.0105
m	1.1873	1.2

Table 3-4: Material constants for Kocks and Mecking model for AA 5083.

Parameter	Author's Value
$\left(\frac{\Theta}{\mu}\right)_0$	0.275
b	2.91E-10 m
$\dot{\varepsilon}_0$	1.0E7 s^{-1}
p	0.5
q	1.5
g_0	0.5925
$\frac{\sigma_{V0}}{\mu_0}$	0.04598

Table 3-4 Continued

Parameter	Author's Value
R^2 (V)	99.05%
g_{Y0}	0.717385
$\frac{\sigma_{Y0}}{\mu_0}$	0.02286
R^2 (Y)	95.95%

The temperature-dependent shear modulus was determined by the following equation:

$$\mu(T) = 2.819E4 + 2.875E-1 * T - 5.082E-2 * T^2 + 6.506E-5 * T^3 - 2.870E-8 * T^4 \quad \textbf{(3-9)}$$

where T is in Kelvin and μ is in MPa [74].

The constants determined for the Sellars and Tegart and Johnson-Cook laws are comparable to those previously found in the literature [61, 75]. No such comparison can be made for the Kocks and Mecking model as it has not previously been fit for AA 5083.

The modeled stress-strain curves from Table 3-1 are compared with experimental data from the Atlas of Formability in Figure 3-3.

The stress-strain curves for the combinations of temperature and strain rate presented in this paper are indicative of general trends that result from the use of each constitutive law evaluated.

The Sellars and Tegart law over-predicts stress at low values of strain due to its inability to capture strain hardening and can result in an under-prediction of saturation due to its lack of dependence on strain.

The Johnson-Cook law over-predicts stress at large strains due to its inability to capture saturation and over-predicts the hardening rate following yield due to the additive nature of the strain hardening term.

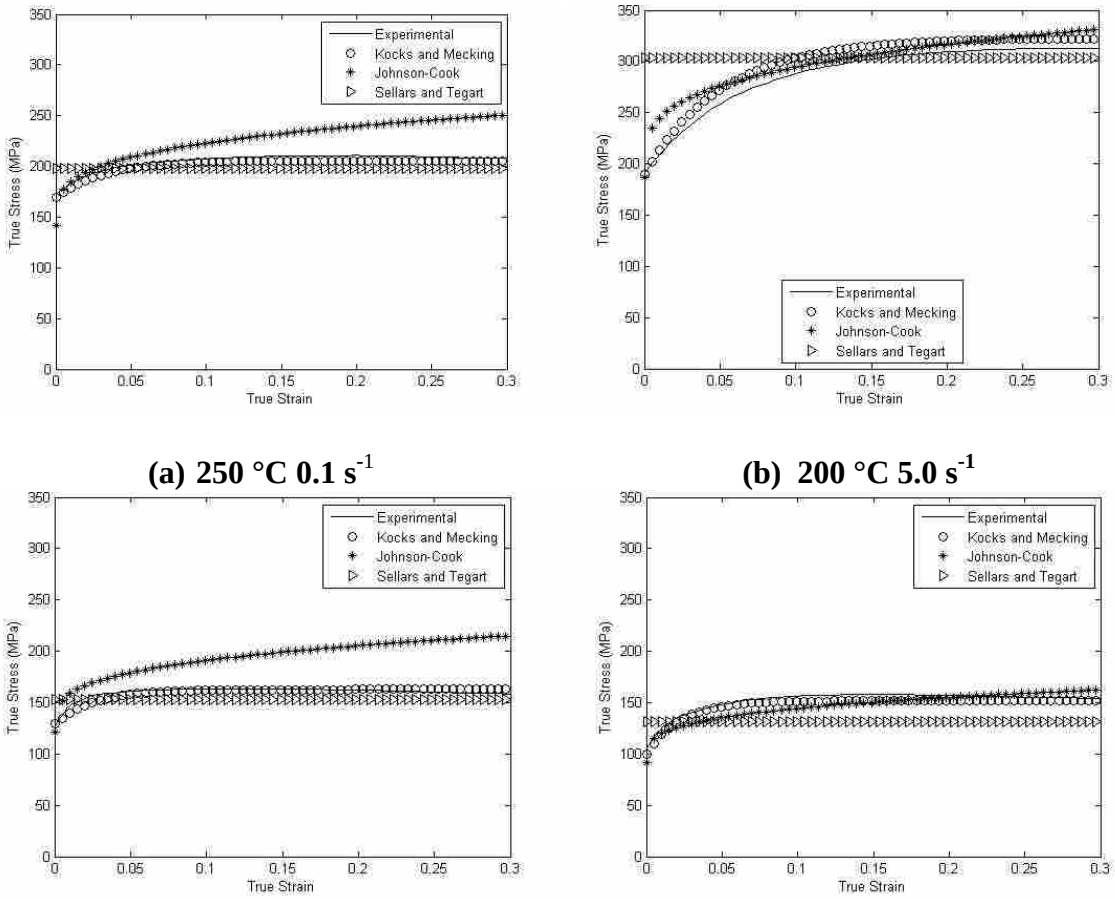

(a) 250 °C 0.1 s^{-1} **(b) 200 °C 5.0 s^{-1}**

(c) 300 °C 0.1 s^{-1} **(d) 400 °C 5.0 s^{-1}**

Figure 3-3: (a), (b), (c), (d) A comparison of experimental and simulated stress-strain curves [76].

The Kocks and Mecking model results in an initial error in slope due to its use of a Voce approximation to the entire hardening rate curve and a relatively constant error due to its ability to capture both strain hardening and saturation with one set of constants. Table 3-5 and Figure 3-4 display the magnitude of the described errors for each constitutive law.

Table 3-5: Maximum percent error near yield and saturation for each constitutive law [76].

		Sellars and Tegart		Johnson-Cook		Kocks and Mecking	
Temperature (°C)	**Strain Rate (s^{-1})**	**Yield (% Error)**	**Saturation (% Error)**	**Yield (% Error)**	**Saturation (% Error)**	**Yield (% Error)**	**Saturation (% Error)**
250	0.1	14.68	5.04	18.16	20.15	2.07	1.45
200	5	57.25	2.99	16.56	5.88	1.52	3.08
300	0.1	17.39	3.64	10.88	35.52	0.57	2.80
400	5	28.12	14.67	10.92	5.19	2.67	1.67

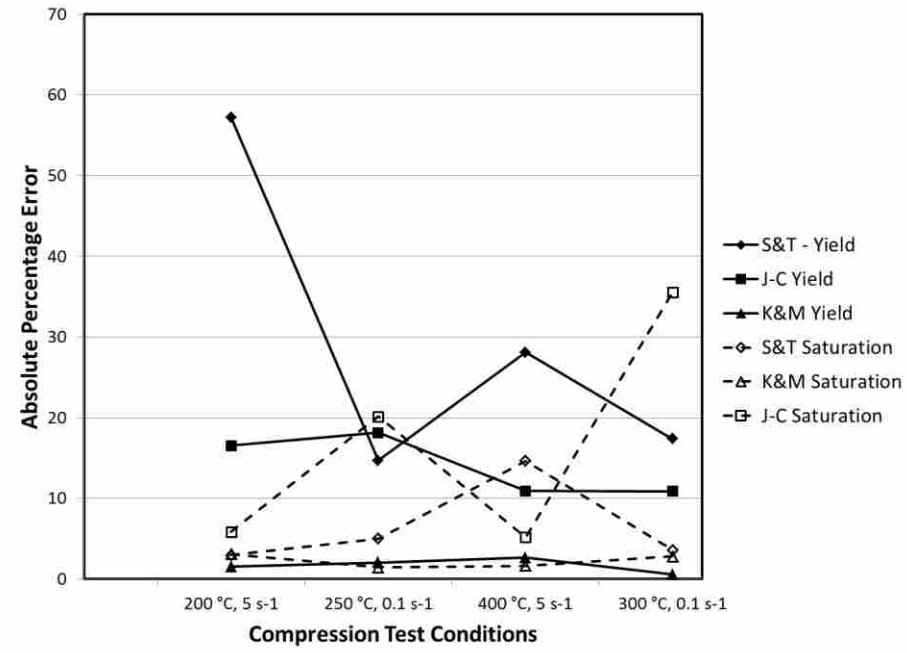

Figure 3-4: A comparison of experimental and simulated stress-strain curves.

Transient behavior is seen in material that is deformed under interrupted temperature or strain rate conditions. Figure 3-5 is an illustration of the transients that exist when prestrain occurs at a different temperature. Kocks and Mecking [58] deformed two texture free Cu-samples in compression at 77 K to an identical flow stress level. Both were then held at room temperature for about 2 hours where one of them was deformed by about 5% strain at a low rate and unloaded. Then deformation was continued for both samples at the original temperature and

strain rate. At the same strain, strain rate, and temperature, the material deformed at room temperature is softer than the material that was only held at room temperature.

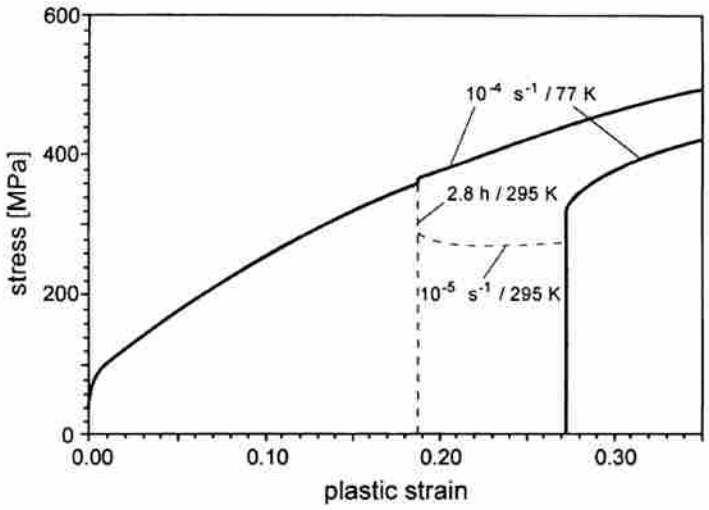

Figure 3-5: This figure is an illustration of the transients that exist when prestrain occurs at a different temperature [58].

An interrupted temperature test was simulated for AA 5083 using all three constitutive laws evaluated in this paper. Deformation was simulated at 200 °C and 5 s^{-1} up to 0.15 strain when the temperature was raised to 400 °C and strain rate was kept at 5 s^{-1} for an additional 0.075 strain. Following deformation under these conditions, the temperature was lowered to 200 °C with no change in strain rate. Figure 3-6, Figure 3-7, and Figure 3-8 show the resultant modeled stress-strain curves for the Sellars and Tegart, Johnson-Cook, and Kocks and Mecking laws, respectively.

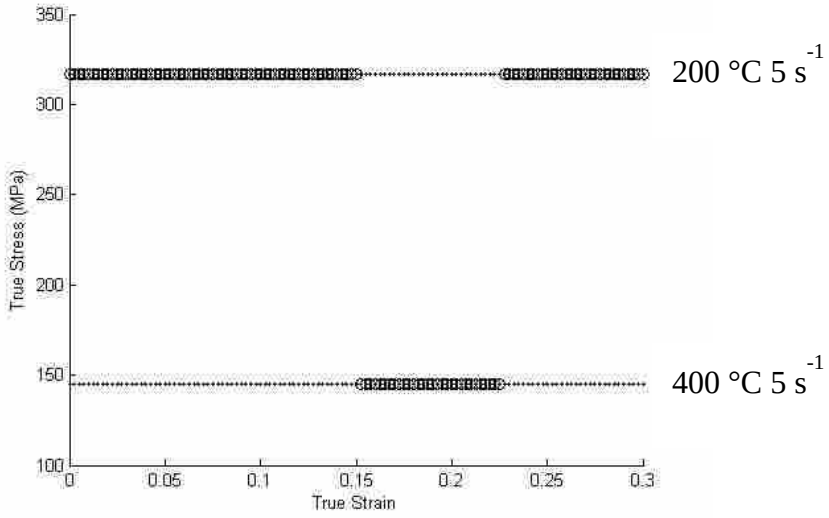

Figure 3-6: Resultant modeled stress-strain curves for the Sellars and Tegart law showing the interrupted temperature constant strain rate curve superimposed on the constant temperature and strain rate curves.

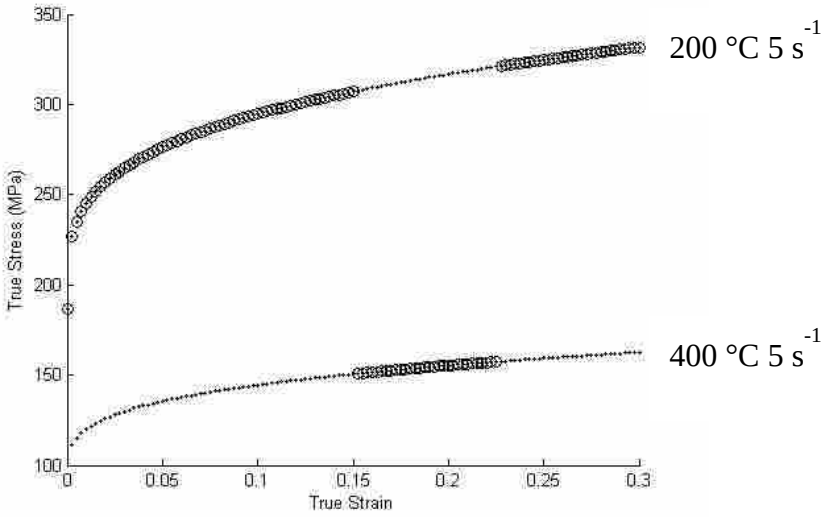

Figure 3-7: Resultant modeled stress-strain curve for the Johnson-Cook law showing the interrupted temperature constant strain rate curve superimposed on the constant temperature and strain rate curves.

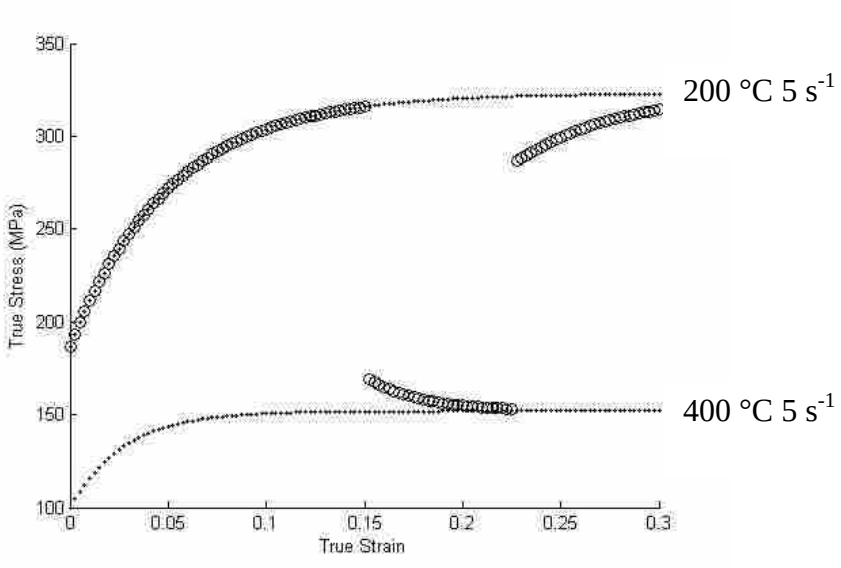

Figure 3-8: Resultant modeled stress-strain curve for the Kocks and Mecking law showing the interrupted temperature constant strain rate curve superimposed on the constant temperature and strain rate curves.

The Sellars and Tegart and Johnson-Cook predictions show no dependence on the temperature at which any prior strain occurred. However, the Kocks and Mecking law is capable of predicting the transients characteristic of changes in temperature seen in experimental data (Figure 3-5).

Figure 3-9 plots a continuous stress-strain curve for a copper sample strained at a strain rate of 10^{-3}, together with one strained at 10^{-4}, but occasionally changed to 10^{-3} [73]. It is seen that the flow stress at the higher rate depends on whether the specimen had been prestrained at the lower or the higher rate (if the comparison is made at the same strain). This observation confirms that the rate of evolution itself depends on the 'path' taken (i.e., the temperature and strain rate) [77]. The transients seen also demonstrate that the accumulated strain used in the Johnson-Cook law is not a proper variable to use in constitutive descriptions: it is a history rather than a state variable.

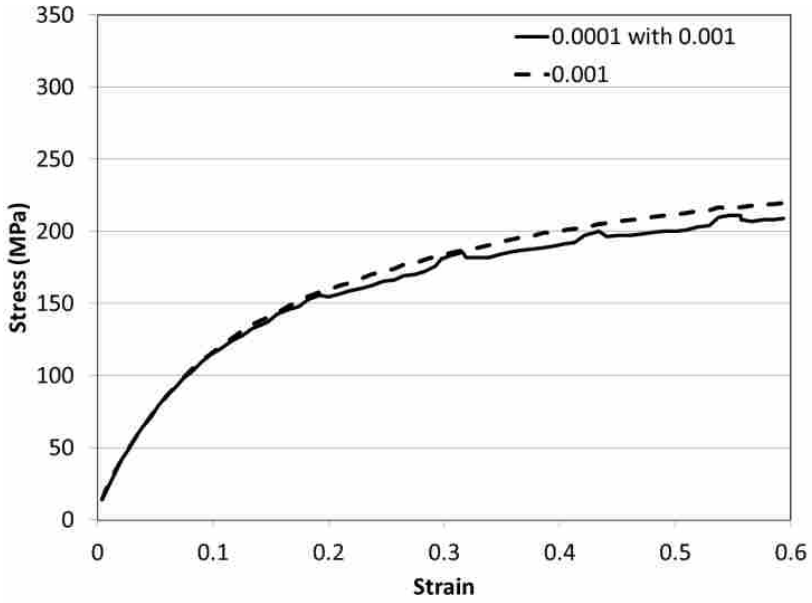

Figure 3-9: A continuous stress-strain curve at 10^{-3} s^{-1} and one at 10^{-4} s^{-1} with occasional excursions to 10^{-3} s^{-1}. Both at 200 °C [73].

An interrupted strain rate test was simulated for AA 5083 using all three constitutive laws evaluated in this paper. Deformation was simulated at 300 °C and 0.1 s^{-1} with occasional excursions to 1 s^{-1}. Figure 3-10, Figure 3-11, and Figure 3-12 show the resultant modeled stress-strain curves for the Sellars and Tegart, Johnson-Cook, and Kocks and Mecking laws, respectively.

The Sellars and Tegart and Johnson-Cook predictions show no dependence on the strain rate at which any prior strain occurred. However, the Kocks and Mecking law is capable of predicting the transients characteristic of changes in strain rate seen in experimental data (Figure 3-9).

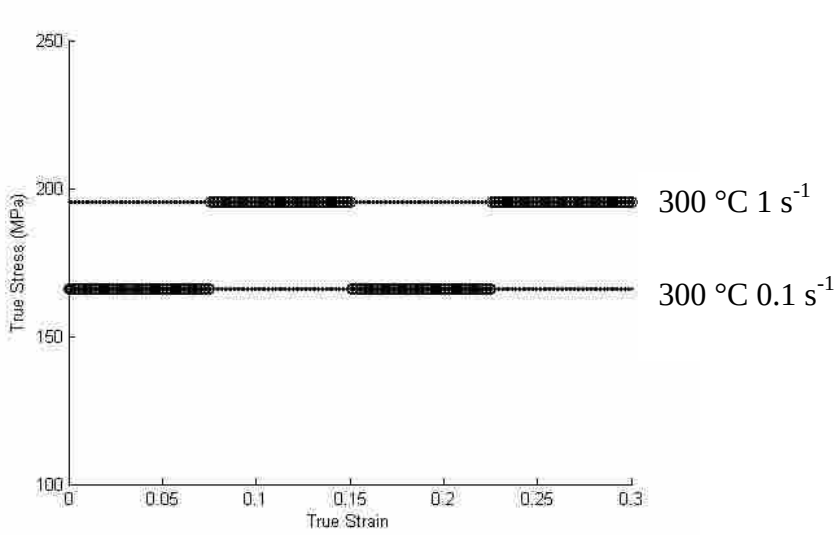

Figure 3-10: Resultant modeled stress-strain curve for the Sellars and Tegart law showing the interrupted temperature constant strain rate curve superimposed on the constant temperature and strain rate curves.

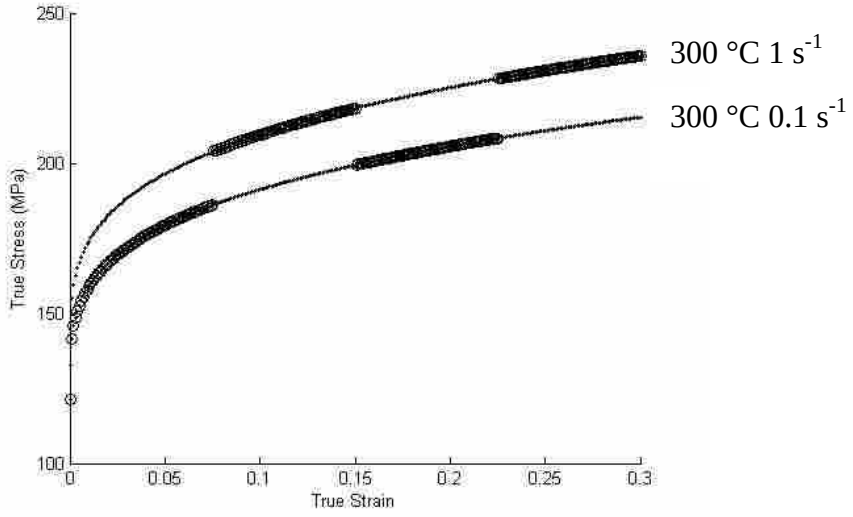

Figure 3-11: Resultant modeled stress-strain curve for the Johnson-Cook law showing the interrupted temperature constant strain rate curve superimposed on the constant temperature and strain rate curves.

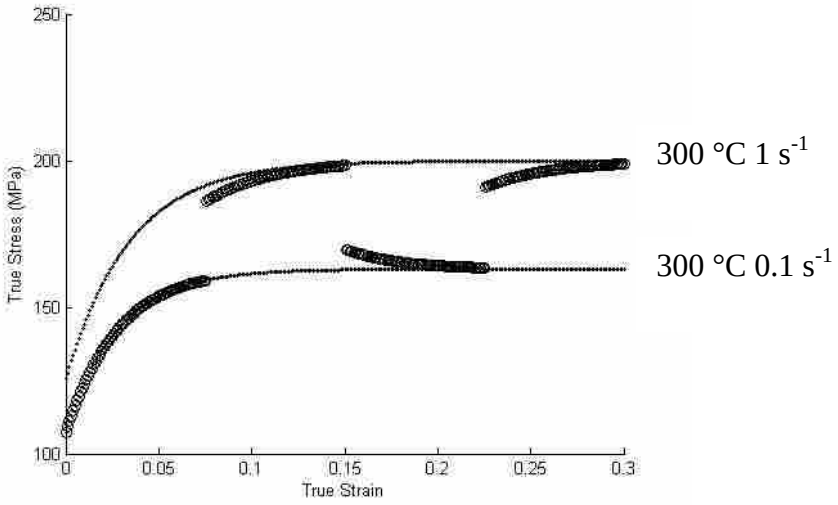

Figure 3-12: Resultant modeled stress-strain curve for the Kocks and Mecking law showing the interrupted temperature constant strain rate curve superimposed on the constant temperature and strain rate curves.

In order to minimize errors in predictions due to discrepancies between testing procedures used to create the Atlas of Formability and testing done by the authors, a new set of constants was determined for each constitutive law to predict variable strain rate behavior determined by the authors.

Cylindrical specimens with a diameter of 12.7 mm (0.5 in) and a height of 25.4 mm (1.0 in) were machined from AA 5083 plate. Isothermal, constant strain rate compression tests were conducted in a MTS machine with Tungsten DiSulfide as a lubricant to minimize barreling of the samples. The samples were tested at combinations of temperature and strain rate between 150 and 350 °C and 0.01 and 1.0 s^{-1}, respectively. Constants were determined for the Sellars and Tegart, Johnson-Cook, and Kocks and Mecking laws in a similar manner to those determined in the previous section. The constants are listed in Table 3-6, Table 3-7, and Table 3-8.

Table 3-6: Material constants for Sellars and Tegart law for AA 5083.

Parameter	Value
A	1.088E10 (s^{-1})
α	0.0109 (1/MPa)
n	5.995
Q	159969 (J/mol)

Table 3-7: Material constants for Johnson-Cook law for AA 5083.

Parameter	Value
A	92 (MPa)
B	475 (MPa)
n	0.0870
C	0.035
m	0.85

Table 3-8: Material constants for Kocks and Mecking model for AA 5083.

Parameter	Value
$\left(\frac{\Theta}{\mu}\right)_0$	0.275
b	2.91E-10 m
$\dot{\varepsilon}_0$	1.0E7 s^{-1}
p	0.5
q	1.5
g_0	0.5925
$\frac{\sigma_{V0}}{\mu_0}$	0.04598
R^2 (V)	99.05%
g_{Y0}	0.717385
$\frac{\sigma_{Y0}}{\mu_0}$	0.02286
R^2 (Y)	95.95%

Additional samples were tested under interrupted strain rate conditions. One test was initiated at a 200 °C and 0.01 s^{-1}. After 0.15 plastic strain, the strain rate was raised to 0.1 s^{-1}. The resultant stress strain behavior compared to predicted behavior for each constitutive law analyzed in this paper is shown in Figure 3-13, Figure 3-14, and Figure 3-15.

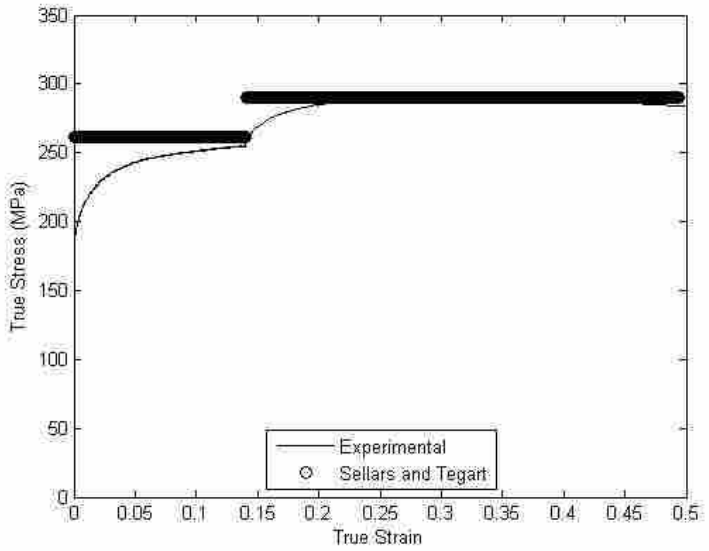

Figure 3-13: Experimental behavior compared to the Sellars and Tegart prediction for isothermal, variable strain rate test conditions at 200 °C.

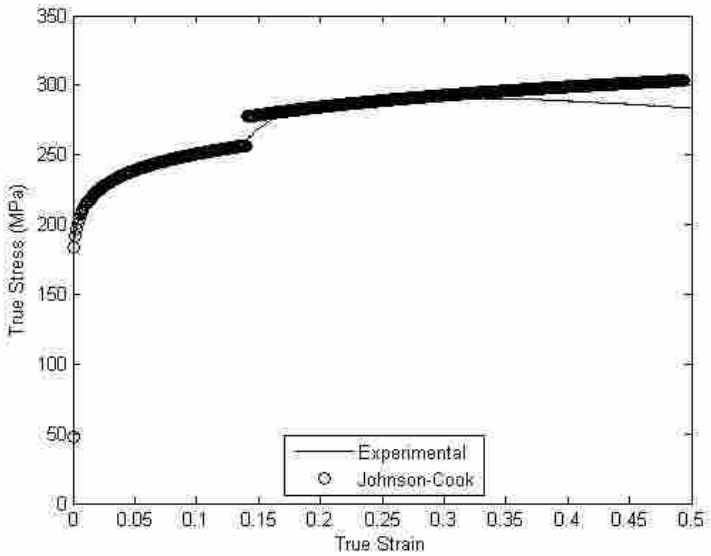

Figure 3-14: Experimental behavior compared to the Johnson-Cook prediction for isothermal, variable strain rate test conditions at 200 °C.

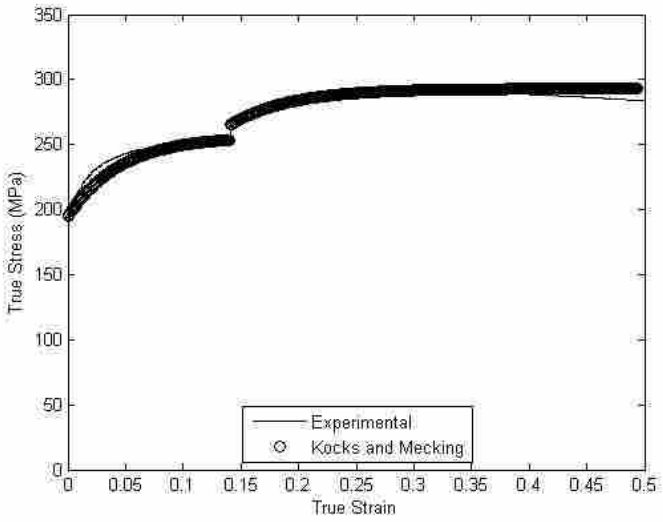

Figure 3-15: Experimental behavior compared to the Kocks and Mecking prediction for isothermal, variable strain rate test conditions at 200 °C.

Figure 3-16 displays the absolute error versus strain for each constitutive law when compared to the experimental data.

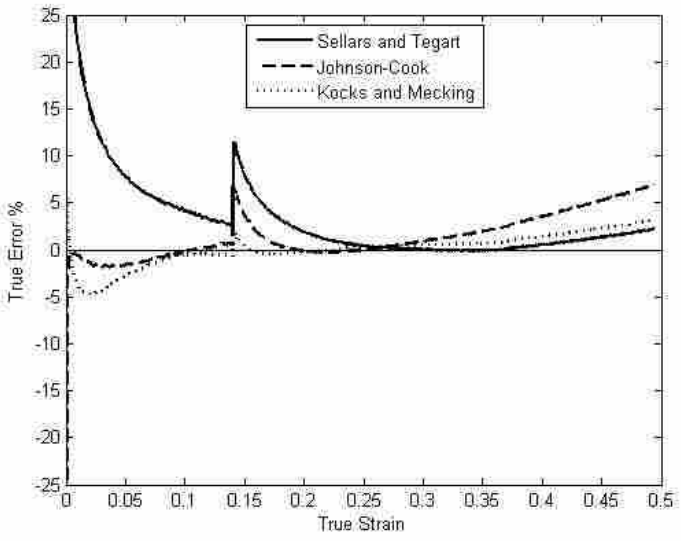

Figure 3-16: Absolute percent error for each constitutive law compared to experimental data.

Near yield, the Johnson-Cook and Kocks and Mecking laws have low errors at approximately 0.5 %, while the Sellars and Tegart law has the largest error at greater than 25 % (Figure 3-16). The Sellars and Tegart law predicts a constants stress, independent of strain (Figure 3-13). This supports the previous claim that the Sellars and Tegart law is unable to capture strain hardening behavior near yield.

At the change in strain rate, the Kocks and Mecking model has the smallest error at approximately 1.5%. The error for the Johnson-Cook law is more than three times that at 6%, and the Sellars and Tegart law is more than six times that for Kocks and Mecking at approximately 12%. This supports the previous claim that the Kocks and Mecking law is the only law of the three investigated capable of capturing transients due to changes in strain rate (compare Figures 3-13 through 3-15).

At saturation, the Sellars and Tegart and Kocks and Mecking models have the lowest errors at approximately 3% for up to 0.5 plastic strain. The Johnson-Cook law results in an error twice as large at 7%. While the Sellars and Tegart and Kocks and Mecking models have predicted saturation at large strain (Figure 3-13 and Figure 3-15), the Johnson-Cook law predicts continued hardening at the end of the test (Figure 3-14) which will cause a continued increase in error at larger strains. This supports the previous claim that the Johnson-Cook law is incapable of capturing saturation at large strains.

The amount of strain characterized by large errors in prediction of stress for each constitutive law analyzed in Figure 3-16 is dependent on the temperature and strain rate at which the deformation takes place.

The amount of deformation that takes place before the material saturates affects the amount of strain for which the Sellars and Tegart law overpredicts stresses due to its inability to

capture strain hardening. This amount of strain characterized by large errors in stress increases with decreasing temperature or increasing strain rate (low activation energies) due to the increase in the duration of hardening (Figure 3-3).

The amount of deformation that takes place before the material saturates also affects the strains at which the Johnson-Cook predictions result in large errors. For high temperatures and low strain rates (high activation energies), the Johnson-Cook law predicts large errors at relative small values of plastic strain (Figure 3-3).

The predicted errors for the Kocks and Mecking model are independent of the temperature and strain rate at which the test is performed (Figure 3-3, Table 3-5, and Figure 3-4). The Kocks and Mecking predictions for all tests analyzed in Figure 3-3 result in errors of less than 5% from yield through saturation.

3.5 Implications in FSW

When modeling the stir zone only, where maximum strains have been reported between 5 and 9 [28, 40], the Sellars and Tegart and Kocks and Mecking models would be appropriate. Both of these constitutive laws are error bounded at high strains due to a zero hardening rate; however, the Johnson-Cook law is not as evidenced by large errors at saturation seen in Figure 3-4.

When modeling the TMAZ only, where there is a high gradient in strain, the Johnson-Cook and Kocks and Mecking models would be appropriate. Both of these constitutive laws are capable of capturing the effects of strain hardening; however, the Sellars and Tegart law is not as evidenced by large errors near yield seen in Figure 3-4. The over-prediction of hardening rate by the Johnson-Cook law at low strains characteristic near the border between the HAZ and TMAZ could lead to an artificially narrow stir zone.

In order to accurately capture the strain hardening characteristics in the TMAZ and the saturation characteristic of the stir zone, the Kocks and Mecking model would be appropriate. Both the Johnson-Cook and Sellars and Tegart laws are incapable of capturing both phenomena, while the Kocks and Mecking model captures both yield and saturation with the smallest error (Figure 3-4).

In order to accurately capture transients that occur due to variable temperature and strain characteristic of friction stir welding, the Kocks and Mecking model would be appropriate. Both the Johnson-Cook and Sellars and Tegart laws are incapable of capturing transient behavior because they determine flow stress using current process parameters only; however, the Kocks and Mecking model accounts for the full thermomechanical history.

3.6 Conclusions

Constants for the Kocks and Mecking model for AA 5083 have been determined and reported. A process to determine constants for the Kocks and Mecking model from Atlas of Formabilty data was described.

Constants for the Sellars and Tegart, Johnson-Cook, and Kocks and Mecking models were determined from the same set of experimental data. Model predictions have been compared with experimental data under constant temperature and strain rate conditions as well variable strain rate conditions.

The Sellars and Tegart law is capable of capturing saturation but incapable of capturing strain hardening, which can account for up to 0.2 plastic strain. The Sellars and Tegart law can also result in under-predictions at saturation due to its lack of dependence on strain. The Sellars and Tegart law will be most accurate in the stir zone due to the characteristically high strains.

The Johnson-Cook law is capable of capturing strain hardening. However, its inability to capture saturation causes over-predictions of stress at large strains. The additive nature of the strain hardening term in the law can result in under-predictions of yield or over predictions of strain hardening following yield. The Johnson-Cook law will be most accurate near the border between the TMAZ and HAZ where strains are low. However, the initial over-prediction of hardening rate could lead to an artificially narrow stir zone.

The Kocks and Mecking model results in the lowest value for maximum error for each combination of temperature and strain rate evaluated in this paper. The Kocks and Mecking model is capable of capturing strain hardening and saturation. However, the initial slope predicted by the model can be inaccurate due to the use of a Voce approximation of the entire hardening rate curve. The Kocks and Mecking model allows modeling of the entire weld region with only one constitutive law and one set of constants.

The Johnson-Cook and Sellars and Tegart laws are incapable of capturing transients characteristic of material behavior during interrupted temperature or strain rate tests because they have no state variable to account for the temperature and strain rate at which previous strain occurred. The strain at which large errors associated with the Sellars and Tegart law end is increased for low temperatures or high strain rates (low activation energies) where there is significant strain hardening. The strain at which large errors associated with the Johnson-Cook law begin is decreased for high temperatures or low strain rates (high activation energies) where there is no significant strain hardening.

The Kocks and Mecking law's use of a state variable to account for prior history (i.e. the temperature and strain rate at which prior strain occurred) results in its ability to capture transients characteristic of material behavior during interrupted temperature or strain rate tests,

indicating superior performance of this constitutive law in a FSW environment. The errors associated with the Kocks and Mecking model are consistent throughout the entire stress strain curve from yield to saturation, including transient behavior.

4 EXTENDING THE KOCKS AND MECKING MODEL TO SOLID SOLUTION STRENGTHENED FCC ALLOYS OF VARIOUS STACKING FAULT ENERGY

4.1 Abstract

The Kocks and Mecking model has been modified to capture material behavior for materials that exhibit two hardening mechanisms. The Kocks and Mecking model was developed to capture material behavior for pure face-centered cubic metals. However, all materials investigated were moderate to high stacking fault energy and exhibit only one hardening mechanism.

Material constants for AA 5083, AA 3004, and Inconel 600 were determined from Atlas of Formability data. The traditional Kocks and Mecking model fit well for the two aluminum alloys; however, constants for Inconel 600 could not be determined without modification to the model. The temperature and strain rate combinations for Inconel 600 fell into two hardening domains: low temperatures and high strain rates exhibited twinning while high temperatures and low strain rates exhibited slip. An additional master curve was developed for the Kocks and Mecking model to account for two hardening mechanisms. Model predictions are compared to experimental data from the Atlas of Formability for identical constant temperature and strain rate tests. The errors for the modified Kocks and Mecking model predictions are generally within 10% for all materials analyzed.

4.2 Introduction

The Kocks and Mecking model was developed to capture the material behavior of pure face-centered cubic alloys [58]. The purpose of this work is to analyze the applicability of the Kocks and Mecking law when extended to solid solution strengthened face-centered cubic (fcc) alloys of various stacking fault energies.

The Kocks and Mecking law consists of three master curves and one implicit equation [58]. Compression data is used to calculate the hardening rate which is defined as:

$$\Theta = \frac{d\sigma}{d\varepsilon} \tag{4-1}$$

when temperature and strain rate are held constant. Hardening rate curves are produced by plotting hardening rate against flow stress (Figure 4-1).

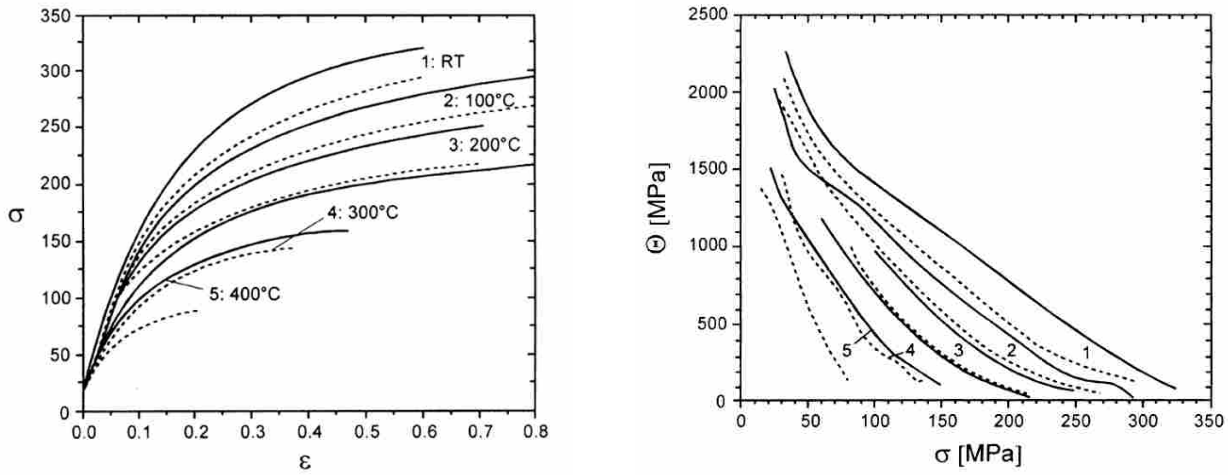

(a) **(b)**

Figure 4-1: (a) Compression stress-strain curves for strain rates of 1 s^{-1} (solid) and 10^{-4} s^{-1} (dashed) at the indicated temperatures [58]. (b) Differentiated stress-strain curves plotted against stress [58].

When hardening rate is normalized by temperature dependent shear modulus and stress is normalized by a scaling stress, plots of hardening rate versus stress for several combinations of

temperature and strain rate can be collapsed onto one master curve (Figure 4-2). As published by Kocks and Mecking [58], only one hardening rate master curve is required to characterize the material behavior.

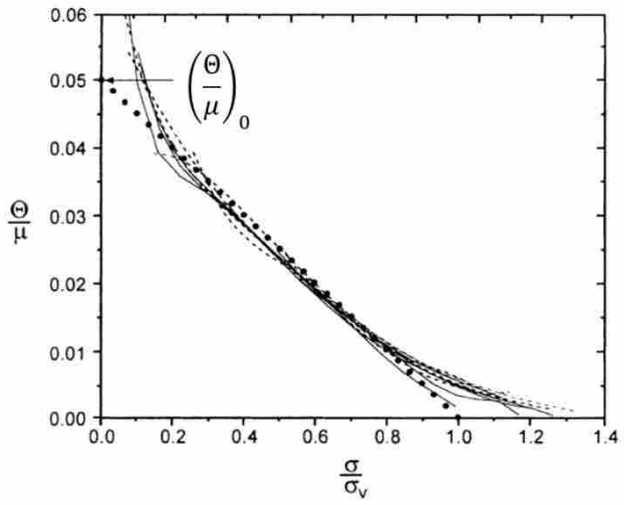

Figure 4-2: Normalized Θ-σ plot. The dotted line is the Voce approximation to the stage III hardening rate [58].

The flow stress is represented implicitly by a Voce approximation, a linear representation of hardening rate versus stress which crosses the stress axis at the saturation or Voce stress, to the hardening rate. The normalizing scaling stress for each temperature and strain rate combination is equal to the corresponding Voce stress.

$$\frac{\Theta}{\mu} = \left(\frac{\Theta}{\mu}\right)_0 \left(1 - \left[\frac{\sigma/\sigma_Y}{\sigma_V/\sigma_Y}\right]\right) \quad \textbf{(4-2)}$$

$\left(\frac{\Theta}{\mu}\right)_0$ corresponds to the initial hardening rate, $\left[\frac{\sigma}{\sigma_Y}\right]$ is the state variable (s), $\left[\frac{\sigma_V}{\sigma_Y}\right]$ is the saturation value of the state variable (s^{sat}), and σ_V and σ_Y are the scaling or Voce stress and yield stress, respectively, which are both functions of temperature and strain rate.

The Voce stress master curve relates Voce stress to temperature and strain rate through activation energy:

$$g = \frac{kT}{\mu b^3} \ln\left(\frac{\dot{\varepsilon}_0}{\dot{\varepsilon}}\right) \quad \textbf{(4-3)}$$

Voce stress normalized by the temperature dependent shear modulus can be related to activation energy using Equation 4-4 [58].

$$\frac{\sigma_V}{\mu} = \frac{\sigma_{V0}}{\mu_0}\left\{1 - \left(\frac{1}{g_0}\frac{kT}{\mu b^3}\ln\frac{\dot{\varepsilon}_0}{\dot{\varepsilon}}\right)^p\right\}^q \quad \textbf{(4-4)}$$

μ is the temperature dependent shear modulus, k is the Boltzmann constant, b is the magnitude of the Burgers vector, p and q are phenomenological parameters, and $\dot{\varepsilon}_0$ is a constant on the order of magnitude of 10^7 s^{-1}.

While no master curve for yield stress has been reported in the literature, a relationship between yield stress and temperature and strain rate is needed to implement the Kocks and Mecking law. Kocks and Mecking [58] suggested that if the hardening rate master curve undergoes an optimized yield shift, the hardening rate master curve can be recollapsed onto a new master curve with a new variable on the abscissa:

$$\frac{\boldsymbol{\sigma - \sigma_Y}}{\boldsymbol{\sigma_V - \sigma_Y}} \quad \textbf{(4-5)}$$

as seen in Figure 4-3.

While the initial hardening rate master curve will be used to evolve the state variable (s), the values determined for yield stress from the optimized shift can be related to activation energy using the same function form as the relationship between Voce stress and activation energy:

$$\frac{\sigma_Y}{\mu} = \frac{\sigma_{Y0}}{\mu_0}\left\{1 - \left(\frac{1}{g_{Y0}}\frac{kT}{\mu b^3}\ln\frac{\dot{\varepsilon}_0}{\dot{\varepsilon}}\right)^p\right\}^q \quad \textbf{(4-6)}$$

where p, q, and $\dot{\varepsilon}_0$ are the same values used to determine the corresponding relationship for Voce stress.

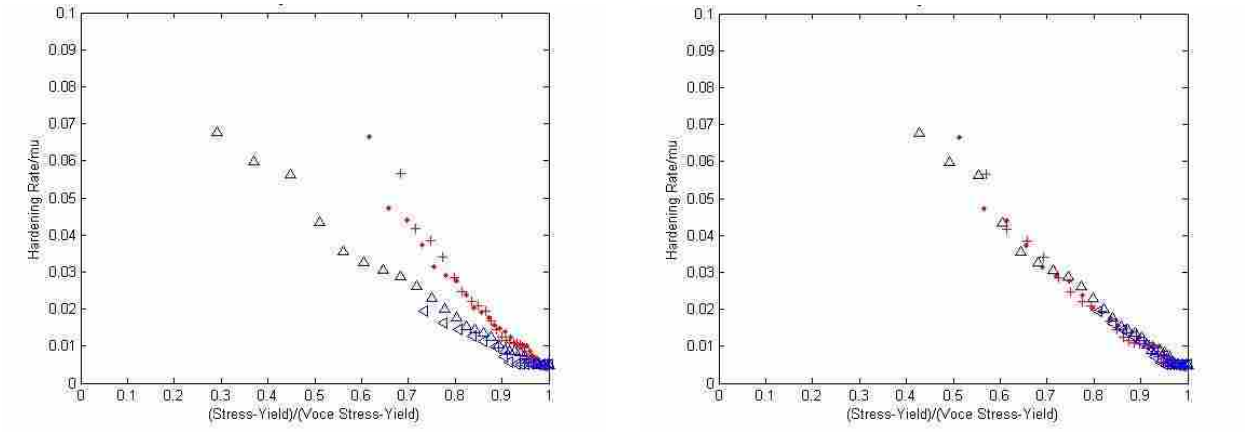

(a) **(b)**

Figure 4-3: (a) Hardening rate master curve before optimized yield shift. (b) Hardening rate master curve following yield shift.

As a result of thermal activation control, material behavior is preserved when temperature or strain rate are varied such that the normalized activation energy $g = \frac{kT}{\mu b^3} \ln\left(\frac{\dot{\varepsilon}_0}{\dot{\varepsilon}}\right)$ is within the experimental range [73]. Then, this is not really an extrapolation of material properties, but an interpolation in activation energy.

Master curves capture flow stress data from a wide range of strain rates and temperatures. All constants and relationships can be determined from uniaxial deformation, typically compression testing, at various combinations of constant strain rate and temperature. Thus, data at constant strain rate and temperature can be applied to any variable path.

The Kocks and Mecking model was developed for high purity fcc, moderate to high stacking fault energy materials. Such materials exhibit slip under standard test conditions; however, the model has not been demonstrated for lower stacking fault energy materials, such as solid solution strengthened fcc alloys, which may exhibit twinning under standard conditions.

Kalidindi [78] provides a framework for including deformation twinning in crystal plasticity models. Salem et. al [79] performed a study on strain hardening due to deformation

twinning in α-Titanium. They included deformation twinning into a Taylor-type crystal plasticity model. Model predictions for the overall stress-strain response and texture evolution compared well with experimental results. These results emphasize the necessity of incorporating twinning into realistic constitutive descriptions.

The dominant hardening mechanism for a given material, either slip or twinning, is dependent on both stacking fault and activation energy. Twinning occurs readily in materials with low stacking fault energy (SFE), such as 304 stainless steel; however, reports of twinning have not been found in the literature for high SFE materials, such as aluminum. Twinning in moderate SFE materials, such as copper, is only seen at low activation energies (low temperatures or large strain rates) [80, 81]. This implies that a critical value for activation energy exists which separates the two domains, slip and twinning. If twinning occurs, the hardening rate is greater than that for slip alone [81, 82].

Dislocation motion is highly sensitive to strain rate and temperature, while twinning has a much lower sensitivity to these parameters [83]. This difference in dependencies leads to separate slip and twinning domains [84]. A critical stress for twinning can be compared to a critical stress for slip to determine which mode will dominate. The mechanism with the lower critical stress should be the preferred mode of deformation [85].

The critical stress for twinning is dependent on the SFE (γ) and the magnitude of the burgers vector of a Shockley partial dislocation (b_P) according to Equation 4-7 [86].

$$\tau_{twinning} = \frac{\gamma}{b_p} \quad \textbf{(4-7)}$$

The critical stress for twinning has been reported to have little to no dependence on temperature in fcc metals [80].

The critical stress for slip is not explicitly a function of SFE [83], but is related to the temperature dependent shear modulus (μ), magnitude of the burgers vector of a unit dislocation (b), and a critical length of a pinned dislocation ($\bar{l}$) by the following equation [85].

$$\tau_{slip} = \frac{\mu b}{\bar{l}} \quad \textbf{(4-8)}$$

Rohatgi et al. conducted tests on pure Cu as well as several Cu-Al alloys [81]. For high SFE materials, the work hardening rate increased with increasing stacking fault energy. However, for low SFE materials, the work-hardening rate was almost independent of strain rate over the range of strain rates employed.

Johari and Thomas conducted explosive tests on copper and copper-aluminum alloys of known stacking fault energies [85]. A critical deformation pressure was determined for twinning which corresponds to a critical strain rate. The critical pressure (strain rate) increases with increasing stacking fault energy.

The previous discussion indicates that the stacking fault energy as well as test conditions, namely temperature and strain rate, may affect the hardening rate master curve in the Kocks and Mecking model. There is evidence that a critical g value exists which separates the two domains for slip and twinning.

4.3 Results and Discussion

4.3.1 Critical *g* Values as a Function of Stacking Fault Energy

Values collected from the literature were used to create a schematic representation of the dependence of slip and twinning stress on SFE and activation energy. The materials used in this demonstration from lowest to highest SFE are 304 stainless steel, Inconel 600, copper, and aluminum.

The temperature dependent shear modulus for aluminum, copper, and Inconel 600 was determined by a polynomial fit to the data presented by Mecking et al. [74] in Figure 4-4.

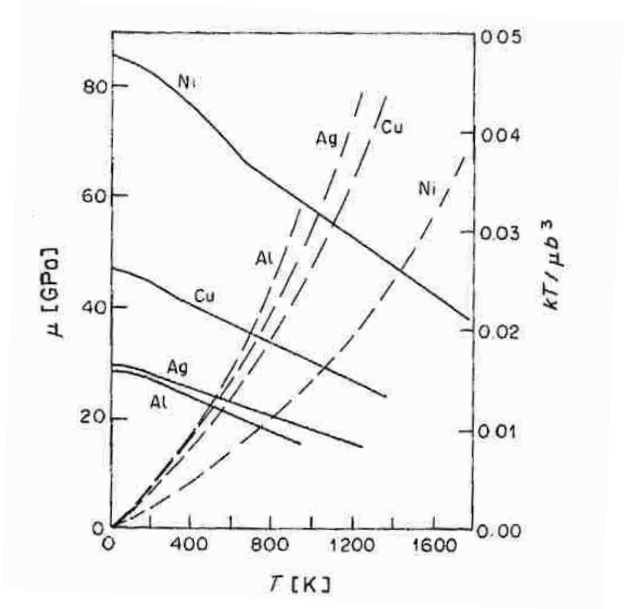

Figure 4-4: Shear modulus (solid) and $kT/\mu b^3$ (dashed) as a function of temperature [74].

The temperature-dependent shear modulus for aluminum was determined by the following equation:

$$\mu(T) = 2.819E4 + 2.875E-1 * T - 5.082E-2 * T^2 + 6.506E-5 * T^3 - 2.867E-8 * T^4 \quad \textbf{(4-9)}$$

where T is in Kelvin and μ is in MPa.

The function for shear modulus for copper is found in the following equation:

$$\mu(T) = 4.718E4 - 1.349E1 * T - 1.422E-2 * T^2 + 1.692E-5 * T^3 - 6.216E-9 * T^4 \quad \textbf{(4-10)}$$

where μ is in MPa, and T is in Kelvin.

The temperature-dependent shear modulus for Inconel 600 was approximated using the shear modulus for Nickel (Figure 4-4). The shear modulus as a function of temperature was determined by the following equation:

$$\mu(T) = 8.567E4 - 1.309E1 * T - 4.501E - 2 * T^2 + 4.043E - 5 * T^3 - 1.108E - 8 * T^4 \quad \textbf{(4-11)}$$

where T is in Kelvin and μ is in MPa.

The function for shear modulus for 304 stainless steel is found in the following equation:

$$\mu(T) = 1.214E5 - 2.836E2 * T + 6.717E - 1 * T^2 - 7.656E - 4 * T^3 + 3.058E - 7 * T^4 \quad \textbf{(4-12)}$$

where μ is in MPa, and T is in Kelvin [87].

The magnitude of the burgers vector for a full and partial dislocation was found using the following relations:

$$b = {a_0}/{\sqrt{2}} \quad \textbf{(4-13)}$$

$$b_p = {a_0}/{\sqrt{6}} \quad \textbf{(4-14)}$$

where a_0 is the lattice parameter for the material.

The critical length values ($\bar{l}$ in Equation 4-8) were estimated based on SFE values for each material in Figure 4-5 [85]. Critical length is not a linear function of SFE, and only a best approximation could be made; however, the critical length increases with decreasing SFE which is consistent with previous work [88]. The values for SFE, lattice parameter, and critical length of a pinned dislocation are shown in Table 4-1 with their associated references.

The critical length for each material was determined by the linear fit to the data in Figure 4-5 in the following equation:

$$\ln(\bar{l}) = -1.0637 * \ln(SFE) + 0.1486 \quad \textbf{(4-15)}$$

where $\bar{l}$ is in μm and *SFE* is in mJ/m^2.

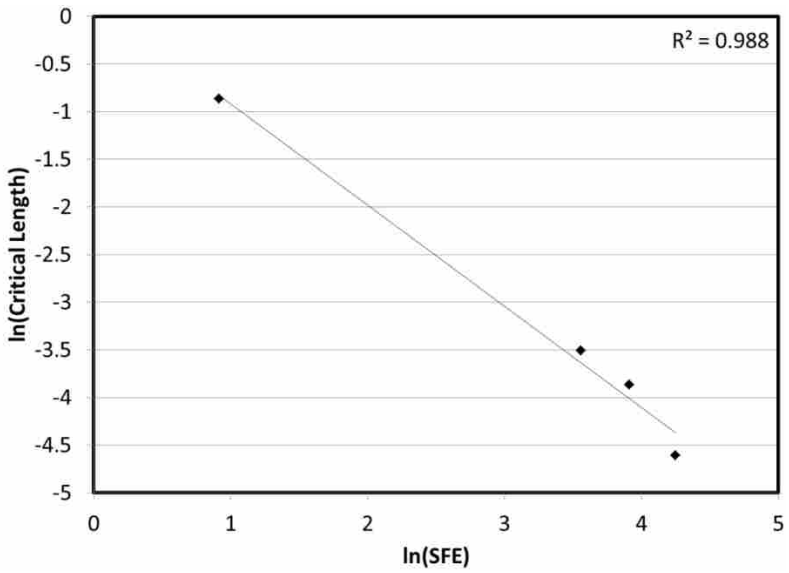

Figure 4-5: Critical length as a function of SFE [85].

Table 4-1: Material values for schematic of twinning and slip domains. References are listed next to the associated values.

Material	SFE (mJ/m^2)	Lattice Parameter (nm)	Critical Length (μm)
Aluminum	166 [86]	0.4050	0.005
Copper	45 [86]	0.3615	0.020
Inconel 600	19 [89]	0.3555 [90]	0.051
304 Stainless Steel	13 [91]	0.361 [92]	0.076

Figure 4-6 illustrates how twinning stress and slip stress are related to SFE and activation energy. Twinning and slip stress values were calculated at a constant strain rate in order to create similar ranges of activation energy for each material with the temperature dependent shear modulus data found in the literature. Thus, slip stress is only a function of temperature. Table 4-2 summarizes the temperature ranges and strain rate for each material as well as the critical activation energy. A maximum *g* value of 0.5 was chosen because most of the tests analyzed in this paper were characterized by activation energies below this value.

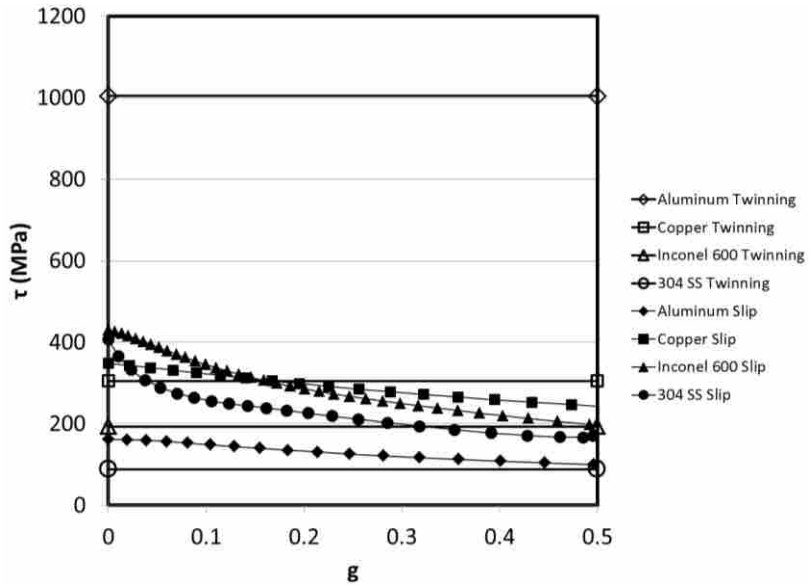

Figure 4-6: Schematic of twinning stress and slip stress as a function of stacking fault and activation energy.

Table 4-2: Maximum temperature, strain rate, and associated maximum *g* value for each material.

Material	Maximum Temperature (K)	Strain Rate (s-1)	Critical *g*
Aluminum	850	0.01	< 0
Copper	850	1E6	0.17
Inconel 600	1750	10	0.50
304 Stainless Steel	1100	1E-5	> 0.5

The schematic in Figure 4-6 is consistent with the work presented by Rohatgi et al. [81]. The lowest SFE material (304 stainless steel) is dominated by twinning over the entire range, while copper, a moderate to high SFE material, switches from slip to twinning at low temperature and high strain rates ($g = 0.17$).

The schematic in Figure 4-6 is also consistent with the work presented by Johari and Thomas [85]. The critical *g* value to switch from slip to twinning decreases with increasing SFE. Figure 4-7 shows critical *g* values from Figure 4-6 as a function of SFE.

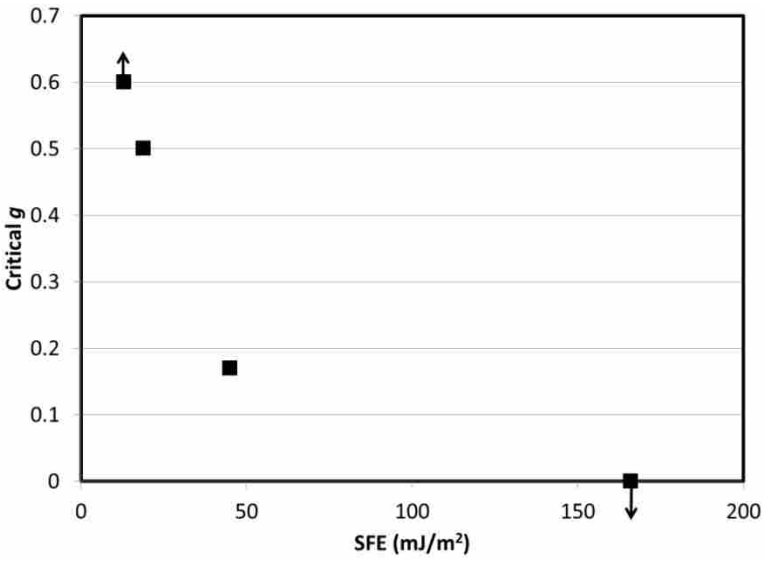

Figure 4-7: Critical *g* value as a function of SFE.

For a high SFE material, e.g. aluminum, slip dominates over the entire range of activation energy, and for a low SFE material, such as stainless steel, twinning dominates over the entire range of activation energy. This implies that only one hardening rate master curve is necessary in the Kocks and Mecking model for high and low SFE materials.

Moderate SFE materials, such as Inconel 600 and copper, exhibit a critical activation energy which separates slip and twinning. If the critical *g* value lies within the test parameters, then two hardening rate master curves may be necessary to capture the contributions of both slip and twinning in the Kocks and Mecking model.

4.3.2 Extending the Kocks and Mecking Model to Various SFE Materials

4.3.2.1 Determining Constants for Kocks and Mecking for Various SFE Materials

All three master curves characteristic of the Kocks and Mecking law were determined for three solid solution strengthened fcc alloys of various SFE: AA 5083, AA 3004, and Inconel 600.

The associated fits for each master curve were used to determine the constants in Equations 4-2, 4-4, and 4-6.

Constant temperature and strain rate data was taken from the Atlas of Formability for each material [72, 93, 94]. Table 4-3 lists the associated ranges of temperature, strain rate, and *g* used to determine master curves for each material analyzed in this paper.

Table 4-3: Ranges of temperature, strain rate, and g used for each material.

	AA 5083		AA 3004		Inconel 600	
	Low	High	Low	High	Low	High
Strain Rate s^{-1}	0.01	5	0.05	15	0.002	0.2
Temperature (°C)	200	500	250	482	871	1204
Activation Energy (g)	0.1721	0.5009	0.2130	0.4985	0.2911	0.5648

In order to implement the Kocks and Mecking model, a two-dimensional Lagrangian finite element code named Hickory was used [71]. The Kocks and Mecking law was added to the source code by the author. Equation 4-16 was used to evolve the state variable. For each simulation the initial state variable was set equal to 1, or yield.

$$\frac{ds}{dt} = \frac{\mu}{\sigma_Y}\left(\frac{\theta}{\mu}\right)_0 \left(1 - \frac{s}{s^{sat}}\right)\dot{\varepsilon} \qquad \textbf{(4-16)}$$

Simulations of axial compression tests identical to source data tests were developed for each material. Table 4-4, Table 4-5, and Table 4-6 list the combinations of temperature and strain rate, with the corresponding activation energy, evaluated in this paper for AA 5083, AA 3004, and Inconel 600, respectively.

Table 4-4: Temperature and strain rate combinations analyzed for AA 5083.

Run	Temperature (°C)	Strain Rate (s^{-1})	Activation Energy (unitless)
1	250	0.1	0.2497
2	400	5	0.2820
3	300	0.1	0.2832
4	300	20	0.2017

Table 4-5: Temperature and strain rate combinations analyzed for AA 3004.

Run	Temperature (°C)	Strain Rate (s^{-1})	Activation Energy (unitless)
1	250	1	0.2497
2	345	1	0.3155
3	250	15	0.2130
4	345	15	0.2691

Table 4-6: Temperature and strain rate combinations analyzed for Inconel 600.

Run	Temperature (°C)	Strain Rate (s^{-1})	Activation Energy (unitless)
1	927	0.002	0.4019
2	1149	0.2	0.4111
3	871	0.2	0.2911
4	1038	0.002	0.4618

4.3.2.2 Application of Kocks and Mecking to Various SFE Materials

Shear modulus as a function of temperature for both aluminum alloys was found using Equation 4-9, and shear modulus as a function of temperature for Inconel 600 was found using Equation 4-11.

4.3.2.2.1 Hardening Rate Master Curves

Figure 4-8 and Figure 4-9 display the hardening rate master curves for the Kocks and Mecking model for AA 5083 and AA 3004, respectively.

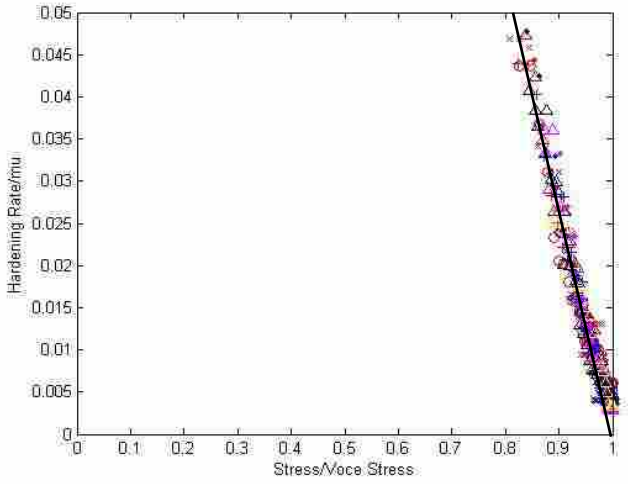

Figure 4-8: Hardening master curve for AA 5083.

Only one hardening rate master curve was required for the aluminum alloys which have high stacking fault energies. This is consistent with Figure 4-6 where slip dominates over the entire range of *g* values for the high SFE material (aluminum).

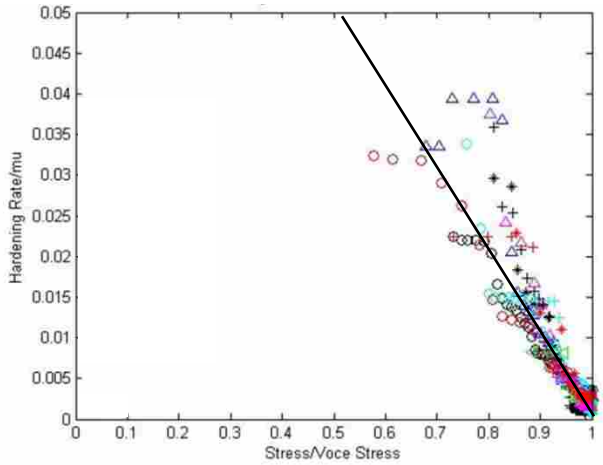

Figure 4-9: Hardening master curve for AA 3004.

The hardening rate curves for Inconel 600 were also plotted to attempt to create one master curve (Figure 4-10). However, one master curve could not be determined with the data presented. The possibility of two hardening rate master curves was determined by inspection. The temperature and strain rate of each individual hardening rate curve was analyzed to see if a distinguishing characteristic could be used to separate the two apparent master curves. It was found that activation energy could serve as this distinguishing characteristic.

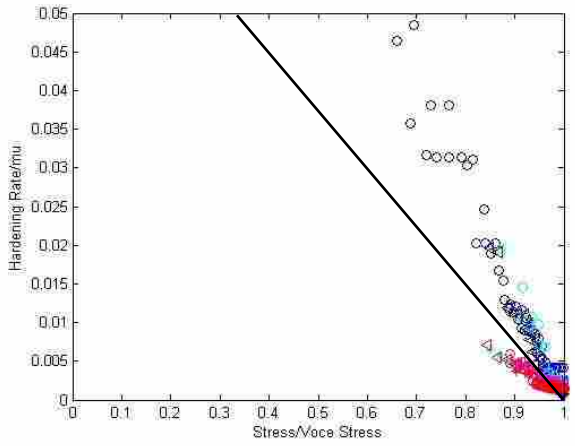

Figure 4-10: Hardening rate master curve for Inconel 600.

Two hardening rate master curves, each with a unique intercept, were determined. Figure 4-11(a) is the hardening rate master curve for the low activation energy values ($0.291 < g < 0.410$), and Figure 4-11(b) is the hardening rate master curve for the high activation energy values ($0.411 < g < 0.565$). Table 4-7 displays the corresponding temperatures and strain rates associated with each range of g.

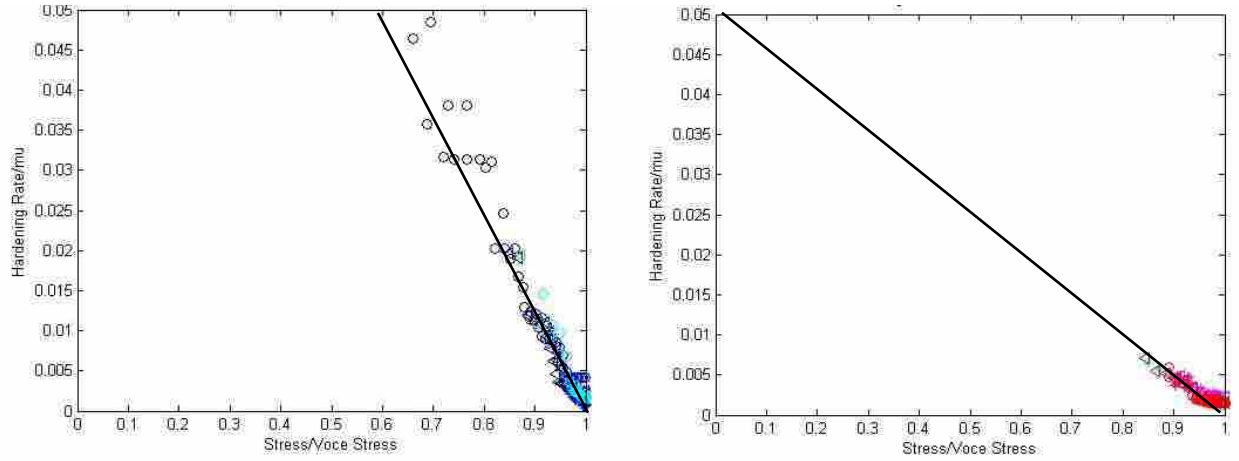

(a) (b)

Figure 4-11: Hardening rate master curve for Inconel 600 (a) low g, (b) high g.

Table 4-7: Separation of temperature and strain rate by low and high activation energy.

Low Activation Energy			High Activation Energy		
Temperature (°C)	Strain Rate (s^{-1})	Activation Energy (g)	Temperature (°C)	Strain Rate (s^{-1})	Activation Energy (g)
871	0.2	0.29109	1149	0.2	0.41108
927	0.2	0.31260	1204	0.2	0.43927
871	0.02	0.33268	1038	0.002	0.46179
927	0.02	0.35726	1149	0.02	0.46980
1038	0.2	0.35917	1204	0.02	0.50203
871	0.002	0.37426	1149	0.002	0.52853
927	0.002	0.40192	1204	0.002	0.56478
1038	0.02	0.41048			

A switch in dominant hardening mechanism was found to occur at a critical *g* value of 0.41. This is consistent with Figure 4-6 where Inconel 600 displays a critical *g* value of 0.5. The determination of two hardening rate master curves indicates that a critical *g* value does exist and that it is within the test parameters in the Atlas of Formability.

The low activation energy curves (Figure 4-11(a)), which correspond to low temperatures and/or high strain rates, are characterized by a higher hardening rate than the high activation energy curves (Figure 4-11(b)). This is consistent with twinning dominant hardening. Twinning

at low activation energies is consistent with Figure 4-6 where the critical stress for twinning is lower than that for slip for Inconel 600 for activation energies less than the critical *g* value.

Murr et al. [95] performed shock loading experiments on several nickel alloys, including Inconel 600. Transmission electron micrographs were used to determine the resultant microstructure. At a pressure of 80 kbar, no deformation twins were present. However at a higher pressure (lower activation energy) of 460 kbar, deformation twins were visible.

Figure 4-12 is a plot of the hardening rate constant for each individual stress-strain curve against activation energy for all three materials. Although there is more scatter in the data for AA 3004 than AA 5083, no clear distinction between low and high activation energies could be made to support the use of two master curves. For Inconel 600, there are two distinct intercepts separated at a *g* value of 0.41. The constants for the hardening rate master curves for all three materials are found in Table 4-8.

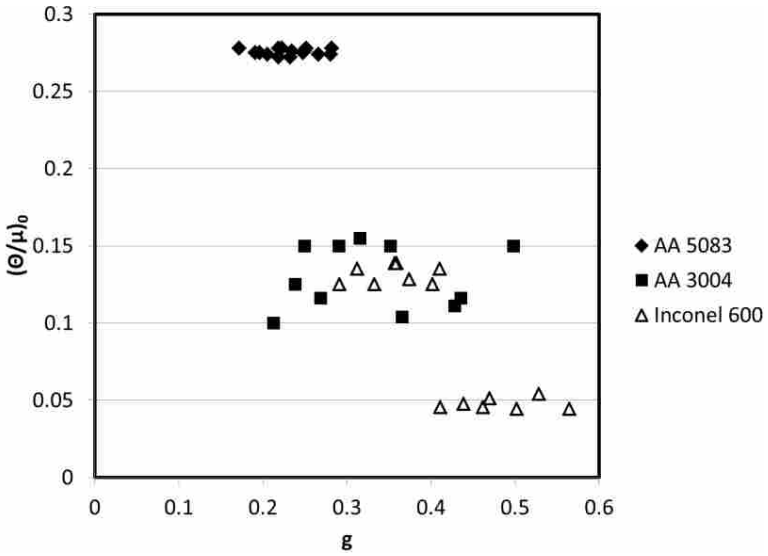

Figure 4-12: Hardening rate constants as a function of activation energy.

Table 4-8: Material constants for hardening rate master curves.

Material	$\left(\frac{\Theta}{\mu}\right)_0$
AA 5083	0.275
AA 3004	0.125
Inconel 600 (low g)	0.13176
Inconel 600 (high g)	0.04762

4.3.2.2.2 Voce Stress Master Curves

The Voce stress master curves for AA 5083, AA 3004, and Inconel 600 are displayed in Figure 4-13, Figure 4-14, and Figure 4-15, respectively.

The constants associated with the Voce stress master curve for each material are listed in Table 4-9.

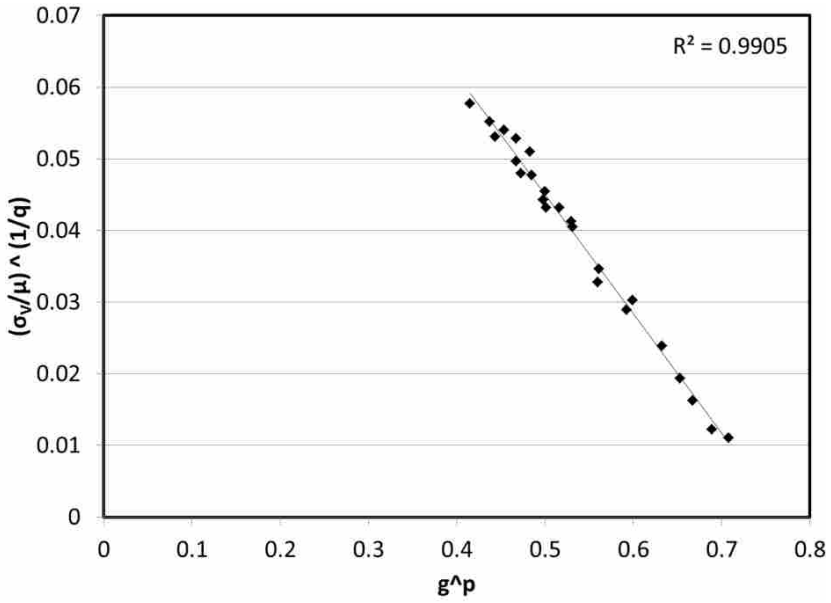

Figure 4-13: Voce stress master curve for AA 5083.

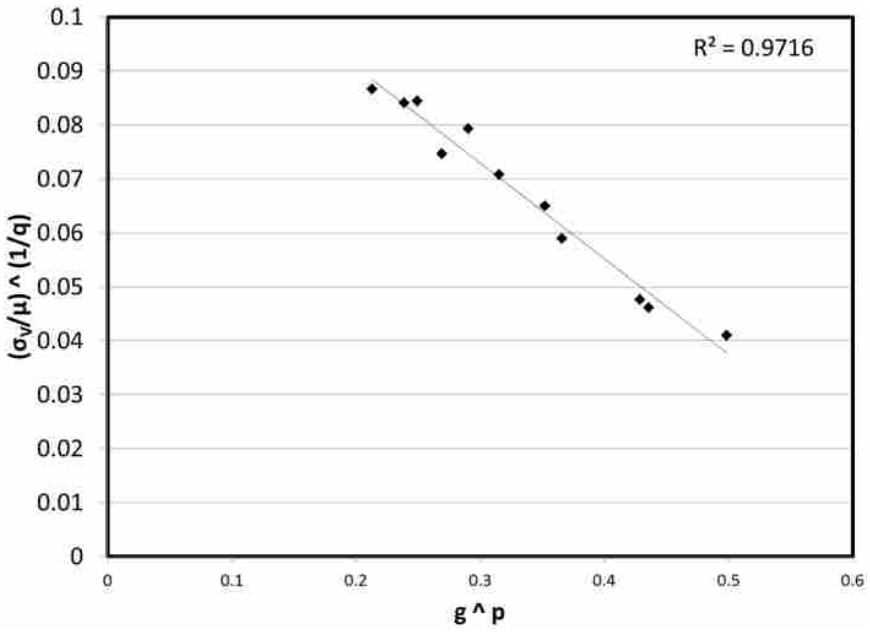

Figure 4-14: Voce stress master curve for AA 3004.

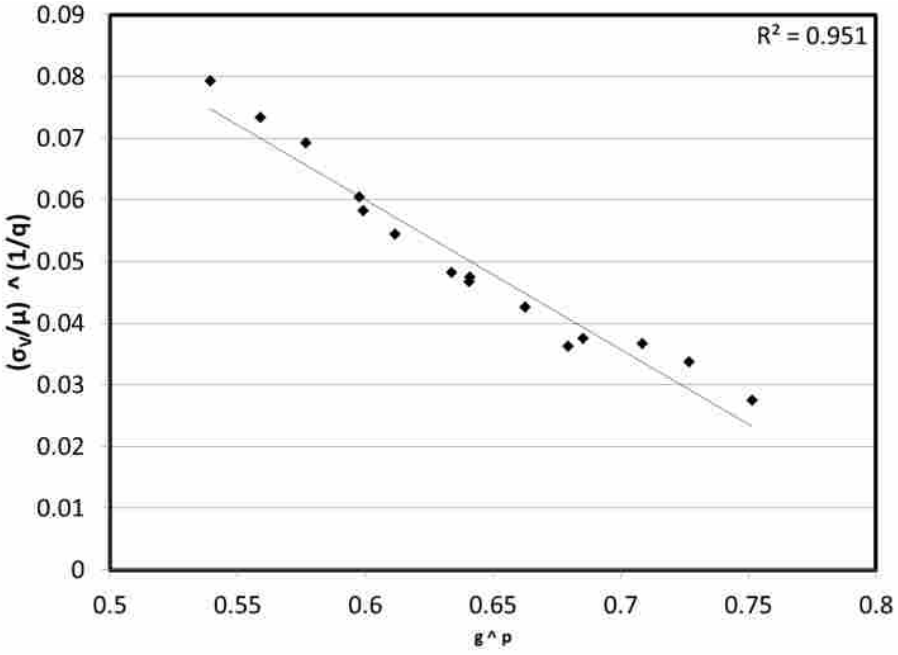

Figure 4-15: Voce stress master curve for Inconel 600.

Table 4-9: Constants for Voce stress master curves.

Constant	AA 5083	AA 3004	Inconel 600
b	2.91E-10 m	2.91E-10 m	2.54E-10 m
$\dot{\varepsilon}_0$	1.0E7 s^{-1}	1E8	2E6
p	0.5	1	0.5
q	1.5	2	2
g_0	0.5925	0.70523	0.71796
$\frac{\sigma_{V0}}{\mu_0}$	0.04598	0.01638	0.042395
R^2	99.05	97.16	95.1

4.3.2.2.3 Yield Stress Master Curves

The yield stress master curves for AA 5083, AA 3004, and Inconel 600 are displayed in Figure 4-16, Figure 4-17, and Figure 4-18, respectively.

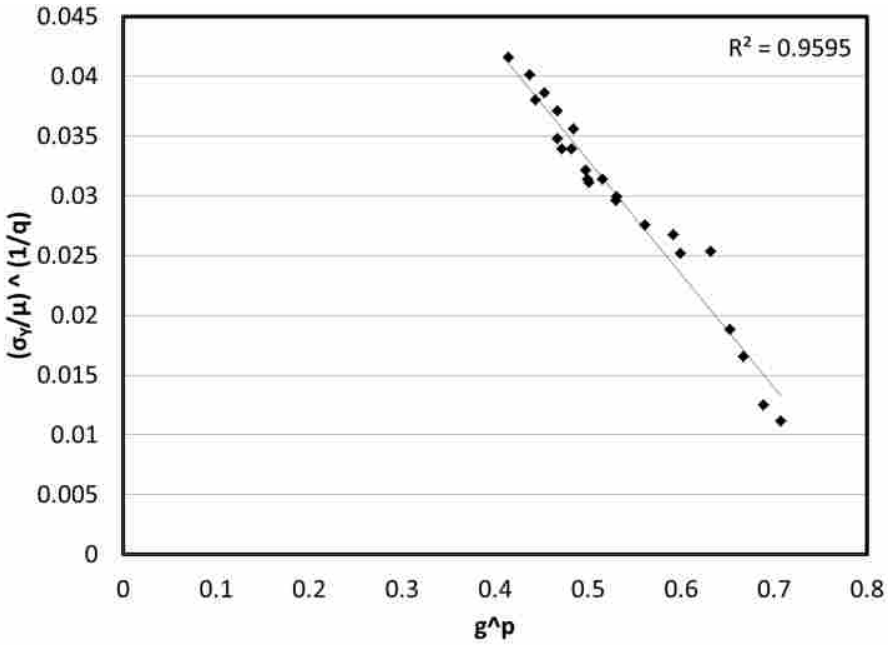

Figure 4-16: Yield stress master curve for AA 5083.

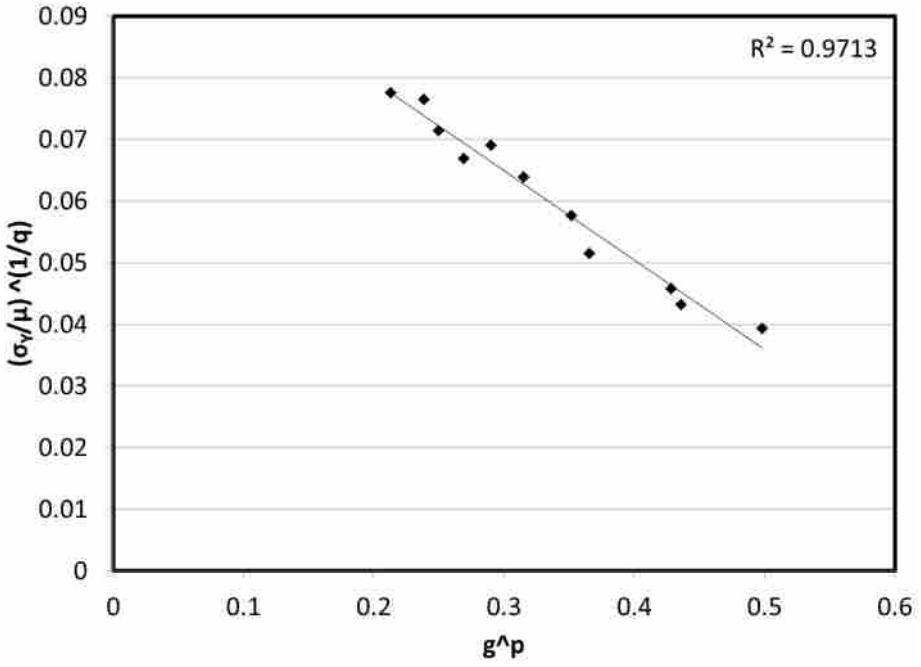

Figure 4-17: Yield stress master curve for AA 3004.

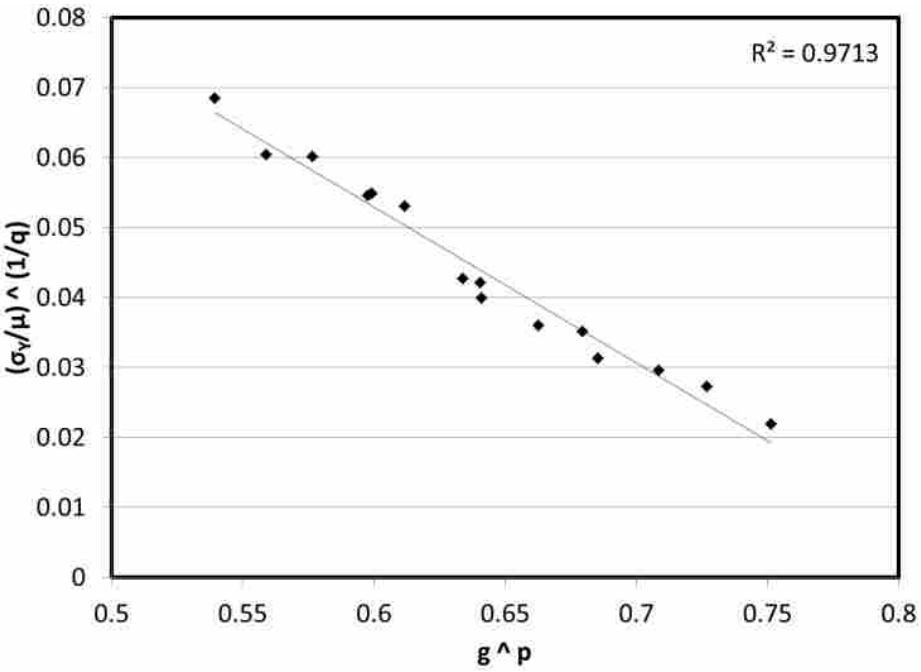

Figure 4-18: Yield stress master curve for Inconel 600.

Table 4-10 summarizes the constants determined for the yield stress master curves.

Table 4-10: Constants for yield stress master curves.

Constant	AA 5083	AA 3004	Inconel 600
b	2.91E-10 m	2.91E-10 m	2.54E-10 m
$\dot{\varepsilon}_0$	1.0E7 s^{-1}	1E8	2E6
p	0.5	1	0.5
q	1.5	2	2
g_{Y0}	0.717385	0.74725	0.699042
$\frac{\sigma_{Y0}}{\mu_0}$	0.02286	0.01177	0.035044
R^2	95.95	97.13	96.63

4.3.2.2.4 Comparisons of Experimental Data and Model Predictions

The plots shown in Figure 4-19 are simulated compression data at combinations of temperature and strain rate that were used to determine the constants for the Kocks and Mecking model for AA 5083.

The predictions shown in Figure 4-19 indicate that the constants are valid for combinations of temperature and strain rate used to determine the constants. The constants are capable of predicting yield stress, hardening rate, and voce stress accurately for both combinations of temperature and strain rate.

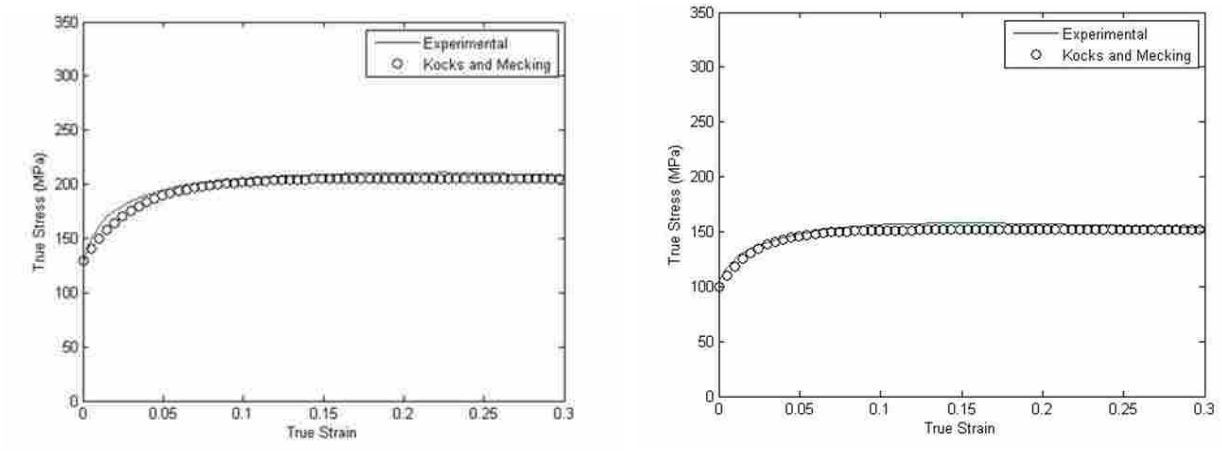

(a) **(b)**

Figure 4-19: AA 5083 (a) 250 °C 0.1 s^{-1} (g = 0.2497) (b) 400 °C 5 s^{-1} (g = 0.2820)

The plots shown in Figure 4-20 are simulated compression data at combinations of temperature and strain rate that were not used to determine the constants for the model for AA 5083. Additionally, the combination of temperature and strain rate shown in Figure 4-20(a) lies outside the range of temperature and strain rate over which the constants were determined, but inside the range of activation energy over which the constants were determined.

The prediction shown in Figure 4-20(a) demonstrates that the constants are valid at combinations of temperature and strain rate within the experimental range, even if the particular combination was not used to determine the constants. Yield stress, voce stress, and hardening rate are all predicted accurately for this combination of temperature and strain rate.

The prediction shown in Figure 4-20(b) demonstrates that the constants are valid even outside the experimental range of temperature and strain rate as long as the combination of temperature and strain rate (g) lies within the experimental range of activation energy. Hardening rate is accurately predicted, and yield and Voce stress values are under-predicted by less than 12%.

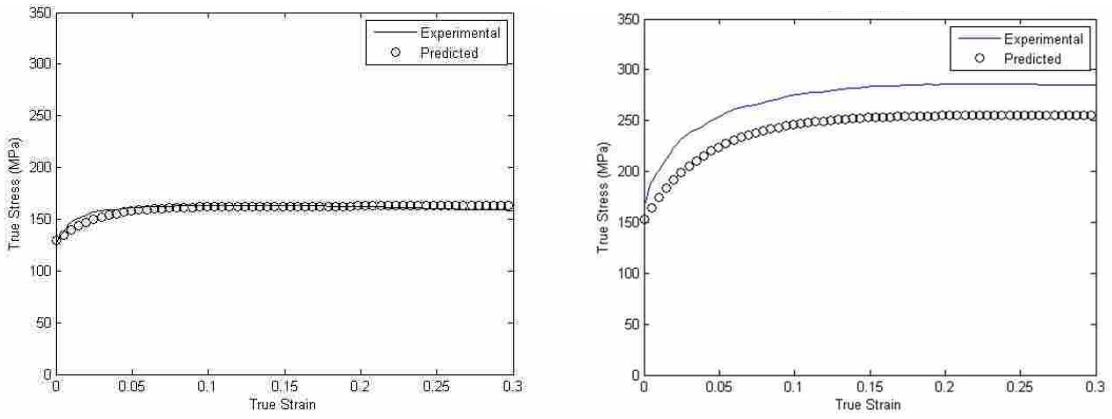

(a) **(b)**

Figure 4-20: AA 5083 (a) 300 °C 0.1 s^{-1} (g = 0.2832) (b) 300 °C 20 s^{-1} (g = 0.2017)

The plots shown in Figure 4-21 and Figure 4-22 are simulated compression data at combinations of temperature and strain rate that were used to determine the constants for the Kocks and Mecking model for AA 3004. No plots will be shown of predictions outside the experimental range of temperature and strain rate due to the limited number of combinations of temperature and strain rate available in the Atlas of Formability for determining constants for AA 3004.

The predictions shown in Figure 4-21 indicate that the constants are valid for combinations of temperature and strain rate used to determine the constants. The constants are capable of predicting yield stress, hardening rate, and voce stress accurately for both combinations of temperature and strain rate.

Figure 4-22(a) demonstrates the effect on predicted stress-strain curve when the hardening rate is not accurate. In this case, the predicted curve crosses the experimental curve at a moderate level of strain. This resultant inaccuracy in hardening rate can be referenced to the amount of scatter in the hardening rate master curve (Figure 4-9).

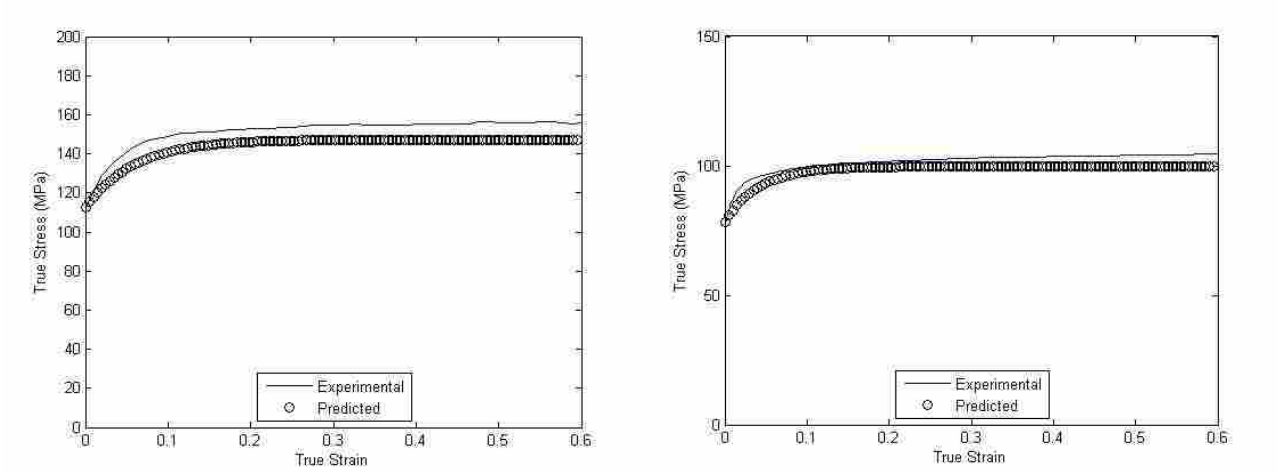

(a) **(b)**

Figure 4-21: AA 3004 (a) 250 °C 1 s^{-1} (g = 0.2497) (b) 345 °C 1 s^{-1} (g = 0.3155)

Figure 4-22(b) demonstrates the effect on the predicted stress-strain curve when there is a combination of errors. At this combination of temperature and strain rate there is over-prediction at yield and an inaccurate hardening rate. The over-prediction of yield compounds with the inaccurate hardening rate to give the maximum error seen at a strain level of approximately 0.12. As previously stated, the error in hardening rate can be referenced to the scatter in Figure 4-9, while the error in yield stress can be referenced to scatter in the yield stress master curve (Figure 4-17). Despite these inaccuracies, the maximum error in flow stress is still less than 10%.

The applicability of the modified Kocks and Mecking model to Inconel 600 is investigated in Figure 4-23, Figure 4-24, and Figure 4-25. The plots shown in Figure 4-23(a) and Figure 4-23(b) are simulated compression data at combinations of temperature and strain rate in the low and high activation energy regimes, respectively. The purpose of Figure 4-23 is to demonstrate the potential of the modified Kocks and Mecking model when the predicted values from all three master curves are accurate.

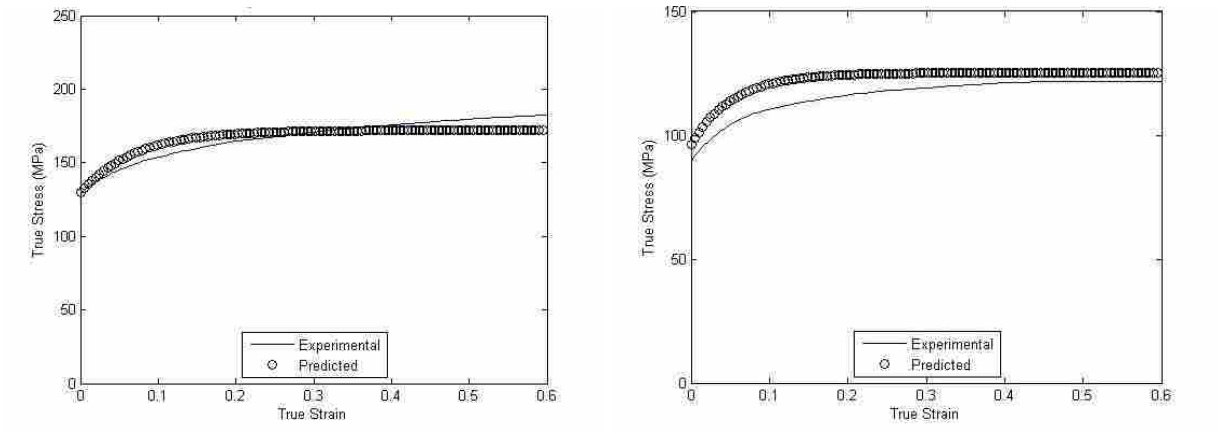

(a) **(b)**

Figure 4-22: AA 3004 (a) 250 °C 15 s^{-1} (g = 0.2130) (b) 345 °C 15 s^{-1} (g = 0.2691)

The errors in model predictions in Figure 4-23(a) and Figure 4-23(b) are less than 7% and 5% across the entire stress-strain curve, respectively. The temperatures and strain rate combinations in Figure 4-23(a) and Figure 4-23(b) correspond to activation energy values of 0.4019 and 0.4111, respectively. These *g* values fall near the middle of the experimental range of activation energy. Errors less than 7% indicated that the modified Kocks and Mecking model performs well for moderate *g* values.

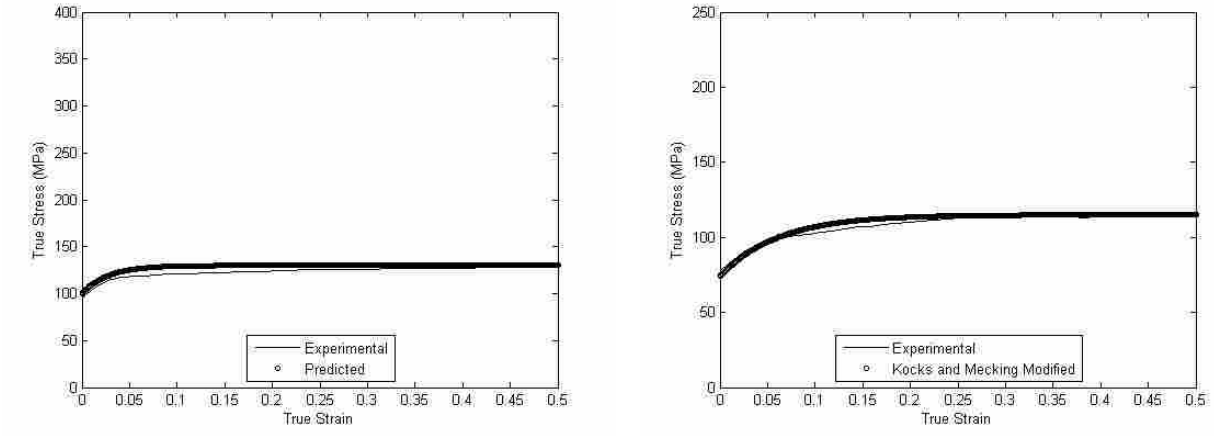

(a) **(b)**

Figure 4-23: Inconel 600 (a) 927 C 0.002 s^{-1} (g = 0.4019) (b) 1149 °C 0.2 s^{-1} (g = 0.4111)

While all three master curves yield accurate predictions for moderate *g* values, the master curves for the yield and Voce stress do not always result in accurate predictions at more extreme values of *g*. Figure 4-24(a) and Figure 4-25(b) demonstrate the result of inaccurate yield and Voce stress predictions for more extreme low and high *g* values, respectively.

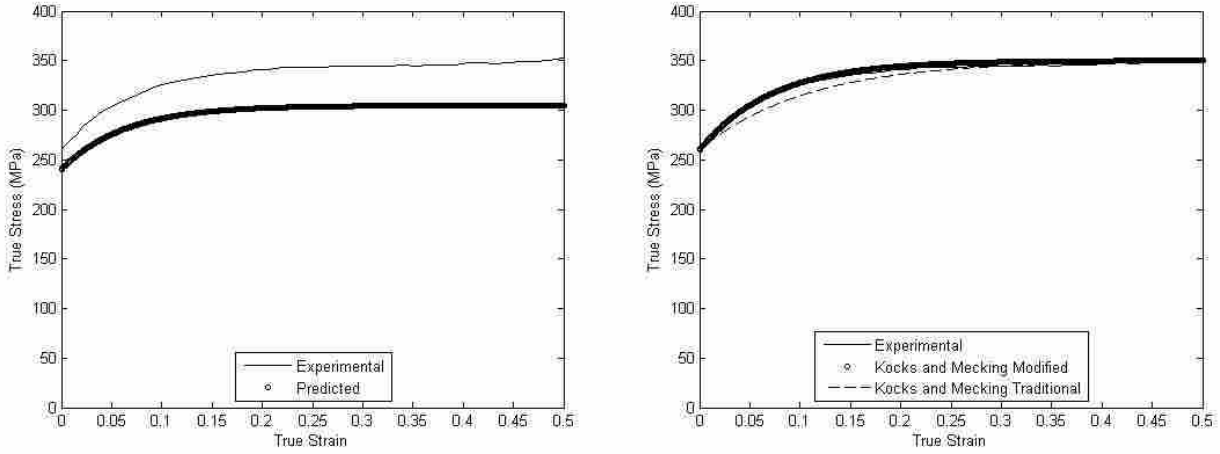

(a) **(b)**

Figure 4-24: Inconel 600 871 °C 0.2 s^{-1} (g = 0.2911) (a) model predicted yield and Voce stress (b) experimental yield and Voce stress.

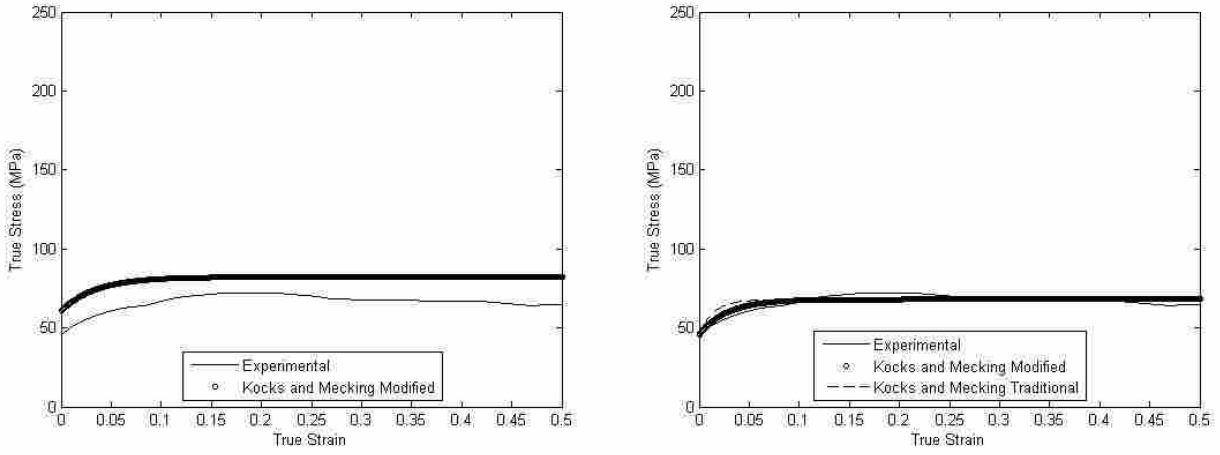

(a) **(b)**

Figure 4-25: Inconel 600 1038 °C 0.002 s^{-1} (g = 0.4618) (a) model predicted yield and Voce stress (b) experimental yield and Voce stress.

The inaccuracies in yield and Voce stress predictions lead to maximum errors of 14% and 25%, for Figure 4-24(a) and Figure 4-25(a), respectively. The magnitude of the shear modulus is a contributing factor to this error. The master curves for yield and Voce stress are determined for the respective stress value normalized by the temperature dependent shear modulus. Thus, errors in yield stress will be magnified by larger values of shear modulus. The shear modulus for Inconel 600 is on the order of two and half times that of the aluminum alloys. It is important to note that the error in yield and Voce stress in more significant (by percentage) for high g values because stress values are lower (Figure 4-15 and Figure 4-18).

In order to investigate the effect of hardening rate alone, the yield and Voce stress values in the model were set to equal the corresponding experimental values in Figure 4-24(b) and Figure 4-25(b). The hardening rate for the modified Kocks and Mecking model is compared to that for the traditional Kocks and Mecking model. The intercept for the hardening rate master curve for the traditional model was found by averaging the two intercepts used in the modified model.

The modified model predicts a hardening rate that is higher than that for the traditional model for low activation energy curves because the traditional model does not account twinning as a different mechanism; the traditional model predicts an average hardening rate for either deformation mechanism. The increased hardening rate of the modified model better represents the increased hardening rate for twinning at low activation energies (Figure 4-24(b)).

The modified model predicts a hardening rate that is higher than that for the traditional model for high activation energy curves because the traditional model does not account for slip as a different mechanism; the traditional model predicts an average hardening rate for either deformation mechanism. The decreased hardening rate of the modified model better represents

the decreased hardening rate for slip without twinning at high activation energies (Figure 4-25(b)).

Figure 4-24(b) and Figure 4-25(b) demonstrate the effect of improving the prediction of both yield and Voce stress. The improvement in flow stress predictions indicates that the modified Kocks and Mecking model does accurately predict hardening rate; however, the prediction of yield and Voce stress are potential areas for improvement in future research.

The ability to predict stress-strain behavior for low and high activation energy curves for Inconel 600 indicates that our modification to the Kocks and Mecking model allows for capturing of both slip and twinning by recognizing the different phenomena and using two hardening rate master curves.

4.4 Conclusions

A critical stress value exists for both slip and twinning. The critical stress for slip is highly dependent on temperature and strain rate, but the critical stress for twinning has little to no dependence on temperature. Thus, two separate domains exist for twinning and slip. The mechanism with the lower critical stress will dominate the hardening.

For high and low SFE materials, only one hardening rate master curve is required for the Kocks and Mecking model because one hardening mechanism dominates over the entire range of temperature and strain rate: slip in high SFE materials and twinning in low SFE materials.

For moderate SFE materials, the test parameters, namely temperature and strain rate, must be considered to determine whether one or two master curves will be necessary to characterize the behavior of the material in the Kocks and Mecking model. For moderate SFE materials, a critical activation energy separates the range of temperature and strain rate into two domains: slip and twinning.

The Kocks and Mecking law can be successfully extended to solid solution strengthened fcc alloys of various SFE. In order to implement this extension, yield stress as a function of temperature and strain rate must be known.

The materials analyzed in this paper, namely AA 5083, AA 3004, and Inconel 600 demonstrate strengths and weaknesses of this model extension.

The results for AA 5083 show that the Kocks and Mecking law can be used to predict stress-strain behavior over a wide range of temperature and strain rate. The AA 5083 master curves had the best fit of the three materials analyzed. It was demonstrated that the use of activation energy in the master curves of the law expand the range of temperature and strain rate over which the constants are valid with maximum errors less than 12%.

The results for AA 3004 show that excessive scatter in a hardening rate master curve can lead to inaccurate prediction. In addition, inaccurate predictions of yield stress values can magnify the effect of an inaccurate hardening rate; however, these inaccuracies resulted in maximum errors less than 10%.

The analysis of Inconel 600 demonstrates the possibility of different phenomena governing hardening rate at low and high values of activation energy. Low values of activation energy correspond to higher hardening rates or twinning, while high values of activation energy correspond to lower hardening rates or slip.

Maximum errors for Inconel 600 are up to 30%, but errors are generally within 10%. The fits for the Voce stress for Inconel 600 are not as good as those for AA 5083 and AA 3004. The nature of both the yield and Voce stress master curves leads to increased errors for higher shear modulus values and high g values. Yield and Voce stress values are multiplied by shear modulus, and high g values correspond to lower stresses. Thus, the relative error is magnified

under these conditions. Improving the prediction of yield and Voce stress is a potential area for future research.

It appears inaccuracies in the modified Kocks and Mecking model are largely due to errors in yield and Voce stress. Hardening rate as a function of activation energy is accurate across the entire range of activation energy for both slip and twinning.

Our modification to the Kocks and Mecking model allows for capturing both slip and twinning by recognizing the difference in phenomena and using two hardening rate master curves.

5 CONCLUSIONS AND RECOMMENDATIONS FOR FUTURE WORK

Constitutive laws have been classified as path-dependent or path-independent. Path-independent laws can be classified by the physical phenomena that they capture. Three-component laws characterize flow stress as a function on strain, strain rate, and temperature. Two-component laws characterize flow stress as a function of strain rate and temperature. One-component laws characterize flow stress as a function of strain rate.

Physics based path-dependent laws allow for the development of master curves. Through the use of master curves, path-dependent laws may provide a method for extending the range of temperature and strain rate over which a constitutive law is valid. Normalization by material properties transforms extrapolation in temperature and strain rate into interpolation in parameters such as activation energy.

Observed material behavior indicates that path-independent laws cannot accurately capture material behavior when gradients in temperature and strain rate exist.

The applicability of several constitutive laws in a friction stir weld has been evaluated. None of the constants for the path-independent laws analyzed in this dissertation were demonstrated valid across the characteristic strains, strain rates, and temperatures in FSW reported in the literature.

The effect of constitutive law on FSW model predictions has been investigated. While holding all other parameters constant, changing the constitutive law in a FSW model can result in

up to a 21% difference in peak temperature. Varying locations for maximum temperature differences indicate that a change in constitutive law may result in a change in predicted temperature profile.

Predicted peak strains can vary by 130%, and predicted peak strain rates can vary by 166%. Differences in flow stress profiles indicate that different constitutive laws may have strengths in different areas of the weld. The Sellars and Tegart and Kocks and Mecking models are able to predict saturation at high strains which occur in the nugget region near the pin. The Johnson-Cook and Kocks and Mecking models are able to capture strain hardening which occurs a small distance from the pin in the thermomechanically affected zone.

The accuracy of flow stress predictions for three constitutive laws used to model FSW has been evaluated using compression data. Constant temperature and strain rate data as well as interrupted strain rate data was used to characterize the errors in model predictions for the Sellars and Tegart, Johnson-Cook, and Kocks and Mecking laws. The characteristics of the errors were used to determine applicability of the constitutive laws to a friction stir weld.

The Sellars and Tegart law is capable of capturing saturation but incapable of capturing strain hardening, which can account for up to 0.2 plastic strain. The strain at which large errors associated with the Sellars and Tegart law end is increased for low temperatures or high strain rates (low activation energies) where there is significant strain hardening. The Sellars and Tegart law can also result in under-predictions at saturation due to its lack of dependence on strain. The Sellars and Tegart law will be most accurate in the stir zone due to the characteristically high strains.

The Johnson-Cook law is capable of capturing strain hardening. However, its inability to capture saturation causes over-predictions of stress at large strains. The strain at which large

errors associated with the Johnson-Cook law begin is decreased for high temperatures or low strain rates (high activation energies) where there is no significant strain hardening. The additive nature of the strain hardening term in the law can result in under-predictions of yield or over predictions of strain hardening following yield. The Johnson-Cook law will be most accurate near the border between the TMAZ and HAZ where strains are low. However, the initial over-prediction of hardening rate could lead to an artificially narrow stir zone.

The Kocks and Mecking model results in the lowest value for maximum error for each combination of temperature and strain rate evaluated in this paper. The Kocks and Mecking model is capable of capturing strain hardening and saturation. However, the initial slope predicted by the model can be inaccurate due to the use of a Voce approximation of the entire hardening rate curve. The Kocks and Mecking model allows modeling of the entire weld region with only one constitutive law and one set of constants.

The Johnson-Cook and Sellars and Tegart laws are incapable of capturing transients characteristic of material behavior during interrupted temperature or strain rate tests because they have no state variable to account for prior history (i.e. the temperature and strain rate at which prior strain occurred); however, the state variable in the Kocks and Mecking law does account for prior history. Thus, the Kocks and Mecking model is capable of predicting transients that occur due to the variable temperature, variable strain rate nature of friction stir welding.

The Kocks and Mecking model has been extended to materials that exhibit more than one deformation mechanism by creating two hardening rate master curves. The dominant mechanism is dependent on the stacking fault energy and activation energy.

A critical stress value exists for both slip and twinning. The critical stress for slip is highly dependent on temperature and strain rate, but the critical stress for twinning has little to no

dependence on temperature. Thus, two separate domains exist for twinning and slip. The mechanism with the lower critical stress will dominate the hardening.

For high and low SFE materials, only one hardening rate master curve is required for the Kocks and Mecking model because one hardening mechanism dominates over the entire range of temperature and strain rate: slip in high SFE materials and twinning in low SFE materials.

For moderate SFE materials, the test parameters, namely temperature and strain rate, must be considered to determine whether one or two master curves will be necessary to characterize the behavior of the material in the Kocks and Mecking model. For moderate SFE materials, a critical activation energy separates the range of temperature and strain rate into two domains: slip and twinning.

The Kocks and Mecking law has been demonstrated to apply in solid solution strengthened fcc alloys AA 5083 and AA 3004. By adding an additional master curve, the Kocks and Mecking model has been extended to capture the two deformation mechanisms observed in moderate stacking fault energy materials.

The Kocks and Mecking law can be used to predict stress-strain behavior for AA 5083 over a wide range of temperature and strain rate. The AA 5083 master curves had the best fit of the three materials analyzed. It was demonstrated that the use of activation energy in the master curves of the law expand the range of temperature and strain rate over which the constants are valid with maximum errors less than 12%.

The results for AA 3004 show that excessive scatter in a hardening rate master curve can lead to inaccurate prediction. In addition, inaccurate predictions of yield stress values can magnify the effect of an inaccurate hardening rate; however, these inaccuracies resulted in maximum errors less than 10%.

The analysis of Inconel 600 demonstrates the possibility of different phenomena governing hardening rate at low and high values of activation energy. Low values of activation energy correspond to higher hardening rates or twinning, while high values of activation energy correspond to lower hardening rates or slip.

Maximum errors for Inconel 600 are up to 30%, but errors are generally within 10%. The nature of the yield and Voce stress master curves leads to increased errors for higher shear modulus values and high g values. Yield and Voce stress values are multiplied by shear modulus, and high g values correspond to lower stresses. Thus, the relative error is magnified under these conditions.

Based upon the results and conclusions discussed previously, it is recommended that the following work be performed.

- Investigate the applicability of the Kocks and Mecking model to pure bcc metals. This may be accomplished by applying the Kocks and Mecking model to Armco Iron.
- Evaluate Kocks and Mecking model predictions for switching between slip and twinning dominated domains. This may be accomplished by selecting a moderate stacking fault energy material which has a critical activation energy that can be obtained under quasistatic conditions.
- Determine an accurate function for critical activation energy versus stacking fault energy. This may be accomplished using Cu-Al alloys of varying Al content.
- Determine an accurate critical activation energy for pure copper. This may be accomplished using cryogenic techniques to induce twinning in the copper.

REFERENCES

1. Thomas, M., J. Nicholas, J. Needham, M. Murch, P. Templesmith, and C. Dawes, *Friction Stir Butt Welding*. 1991: United Kingdom.

2. *Friction Stir Welding*, in *TWI Website*. 2003, TWI.

3. Chao, Y. and X. Qi, "Thermal and Thermo-Mechanical Modeling of Friction Stir Welding of Aluminum Alloy 6061-T6". *Journal of Materials Processing and Manufacturing Science*, 1998: p. 215-233.

4. *ASM Handbook, Vol. 14A, Metalworking: Bulk Forming*. 2005, Materials Park, OH: ASM International.

5. Heurtier, P., C. Desrayaud, and F. Montheillet, "A Thermomechanical Analysis of the Friction Stir Welding Process". *Materials Science Forum*, 2002: p. 1537-1542.

6. Nandan, R., G. Roy, and T. DebRoy, "Numerical Simulation of Three-Dimensional Heat Transfer and Plastic Flow During Friction Stir Welding". *Metallurgical and Materials Transactions A*, 2006: p. 1247-1259.

7. McNelly, T., S. Swaminathan, and J. Su, "Recrystallization Mechanisms during Friction Stir Welding/Processing of Aluminum Alloys". *Scripta Materialia*, 2008: p. 349-354.

8. Cho, J., D. Boyce, and P. Dawson, "Modeling Strain Hardening and Texture Evolution in Friction Stir Welding of Stainless Steel". *Materials Science and Engineering A*, 2005: p. 146-163.

9. Nunes, A., E. Bernstein, and J. McClure. *A Rotating Plug Model for Friction Stir Welding*. in *81st American Welding Society Annual Convention*. 2000. Chicago.

10. Schmidt, H. and J. Hattel, "Thermal Modeling of Friction Stir Welding". *Scripta Materialia*, 2008: p. 332-337.

11. Fratini, L. and G. Buffa, "CDRX Modeling in Friction Stir Welding of Aluminium Alloys". *International Journal of Machine Tool and Manufacture*, 2005: p. 1188-1194.

12. Hamilton, C., S. Dymek, I. Kalemba, and M. Blicharski, "Friction Stir Welding of Aluminium 7136-T76511 Extrusions". *Science and Technology of Welding and Joining*, 2008: p. 714-720.

13. Mahoney, M., C. Rhodes, J. Flintoff, R. Spurling, and W. Bingel, "Properties of Friction-Stir-Welded 7075 T651 Aluminum". *Metallurgical and Materials Transactions A*, 1998: p. 1955-1964.

14. Heurtier, P., M. Jones, C. Desrayaud, J. Driver, F. Montheillet, and D. Allehaux, "Mechanical and Thermal Modeling of Friction Stir Welding". *Journal of Materials Processing Technology*, 2006: p. 348-357.

15. Song, M. and R. Kovacevic, "Thermal Modeling of Friciton Stir Welding in a Moving Coordinate System and its Validation". *International Journal of Machine Tools and Manufacture*, 2003: p. 605-615.

16. Nelson, T., R. Steel, and W. Arbegast, "In Situ Thermal Studies and Post-Weld Mechanical Properties of Friction Stir Welds in Age Hardenable Al Alloys". *Science and Technology of Welding and Joining*, 2003: p. 1-6.

17. Arbegast, W., K. Baker, and P. Hartley. *Fracture Toughness Evaluations of 2195 Al-Cu-Li Autogenous and Hybrid Friction Stir Welds*. in *Proceedings of the 5th International of Conference: Trends in Welding Research*. 1998. Pine Mountain, GA.

18. Arbegast, W. and P. Hartley. *Friction Stir Weld Technology Development at Lockheed Martin Michoud Space System - An Overview*. in *Proceedings of the 5th International Conference: Trends in Welding Research*. 1998. Pine Mountain, GA.

19. Jata, K. and S. Semiatin, "Continuous Dynamic Recrystallization during Friction Stir Welding of High Strength Aluminum Alloys". *Scripta Materialia*, 2000: p. 743-749.

20. Li, Y., L. Murr, and J. McClure, "Flow Visualization and Residual Microstructures Associated with the Friction-Stir-Welding of 2024 Aluminum to 6061 Aluminum". *Materials Science and Engineering A*, 1999: p. 213-223.

21. Benavides, S., Y. Li, L. Murr, D. Brown, and J. McClure, "Low-Temperature Friction-Stir-Welding of 2024 Aluminum". *Scripta Materialia*, 1999: p. 809-815.

22. Schneider, J., A. Nunes, P. Chen, and G. Steele, "TEM Study of the FSW Nugget in AA2195-T81". *Journal of Materials Science*, 2005: p. 4341-4345.

23. Tang, W., X. Guo, J. McClure, and L. Murr, "Heat Input and Temperature Distribution in Friction Stir Welding". *Journal of Matierals Processing and Manufacturing Science*, 1998: p. 163-172.

24. Murr, L., G. Liu, and J. McClure, "TEM Study of Precipitation and Related Microstructures in Friction-Stir-Welded 6061 Aluminum". *Jounal of Materials Science*, 1998: p. 1243-1251.

25. Sato, Y., U. Mitsunori, and H. Kokawa, "Parameters Controlling Microstructure and Hardness during Friction Stir Welding of Precipitation-Hardenable Aluminum Alloy 6063". *Metallurgical and Materials Transactions A*, 2002: p. 625-635.

26. Sato, Y., H. Kokawa, M. Enomoto, and S. Jogan, "Microstructure Evolution of 6063 Aluminum during Friction Stir Welding". *Metallurgical and Materials Transactions A*, 1999: p. 2429-2437.

27. Lienert, T., W. Stellway, B. Grimmett, and R. Warke, "Friction Stir Welding Studies on Mild Steel". *Supplement to the Welding Journal*, 2003: p. 1-9.

28. Buffa, G., L. Donati, L. Fratini, and L. Tomesani, "Solid State Bonding in Extrusion and FSW: Process Mechanics and Analogies". *Journal of Materials Processing Technology*, 2006: p. 344-347.

29. Bastier, A., M. Maitournam, K. Van, and F. Roger, "Steady State Thermomechanical Modeling of Friction Stir Welding". *Science and Technology of Welding and Joining*, 2006: p. 278-288.

30. Khandkar, M., J. Khan, A. Reynolds, and M. Sutton, "Predicting Residual Thermal Stresses in Friction Stir Welded Metals". *Journal of Materials Processing Technology*, 2006: p. 195-203.

31. Buffa, G. and L. Fratini, "Friction Stir Welding of Steels: Process Design through Continuum Based FEM Model". *Science and Technology of Welding and Joining*, 2009: p. 239-246.

32. *ASM Handbook, Vol. 2, Properties and Selection: Nonferrous Alloys and Special-Purpose Materials, 10th ed.* 1990, Materials Park, OH: ASM International.

33. Kostrivas, A. and J. Lippold, "Simulating Weld-Fusion Boundary Microstructures in Aluminum Alloys". *Journal of the Minerals, Metals and Materials Society*, 2004: p. 65-72.

34. Song, M., Kovacevic, R, "Numerical and Experimental Study of the Heat Transfer Process in Friction Stir Welding". *Journal of Engineering Manufacture*, 2003: p. 13.

35. Argyris, J., J. Szimmat, and K. William, "Computational Aspects of Welding Stress Analysis". *Computer Methods in Applied Mechanics and Engineering*, 1982: p. 635-665.

36. Guzman, R., J. Melendez, J. Zahr, and J. Perez-Castellanos, "Determination of the Constituive Relation Parameters of a Metallic Material by Measurment of Temperature Increment in Compressive Dynamic Tests". *Experimental Mechanics*, 2010: p. 389-397.

37. *ASM Specialty Handbook, Stainless Steels*. 1994, Materials Park, OH: ASM International.

38. Norman, A., L. Brough, and P. Pragnell, "High Resolution EBSD Analysis of the Grain Structure in an AA2024 Friction Stir Weld". *Materials Science Forum*, 2000: p. 1713-1718.

39. Rhodes, C., M. Mahoney, W. Bingel, R. Spurling, and C. Bampton, "Effects of Friction Stir Welding on Microstructure of 7075 Aluminium". *Scripta Materialia*, 1997: p. 69-75.

40. Buffa, G., J. Hua, R. Shivpuri, and L. Fratini, "Design of the Friction Stir Welding Tool using the Continuum Based FEM Model". *Materials Science and Engineering A*, 2006: p. 381-388.

41. Zhang, Z. and J. Chen, "The Simulation of Material Behaviors in Friction Stir Welding Process by using Rate-Dependent Constitutive Model". *Journal of Materials Science*, 2008: p. 222-232.

42. Masaki, K., Y. Sato, M. Maeda, and H. Kokawa, "Experimental Simulation of Recrystallized Microstructure in Friction Stir Welded Al Alloy using a Plane-Strain Compression Test". *Scripta Materialia*, 2008: p. 355-360.

43. Frigaard, O., O. Grong, and O. Midling, "A Process Model for Friction Stir Welding of Age Hardening Aluminum Alloys". *Metallurgical and Materials Transactions A*, 2001: p. 1189-1200.

44. Schmidt, H. and J. Hattel, "A Local Model for the Thermomechanical Conditions in Friction Stir Welding". *Modelling and Simulation in Materials Science and Engineering*, 2005: p. 77-93.

45. Askari, A., S. Silling, B. London, and M. Mahoney. *Modeling and Analysis of Friction Stir Welding Processes*. in *Proceedings of Symposium on Firction Stir Welding and Processing*. 2001. Indianopolis, IN: TMS.

46. Darras, B. and M. Khraisheh, "Analytical Modeling of Strain Rate Distribution during Friction Stir Processing". *Journal of Materials Engineering and Performance*, 2008: p. 168-177.

47. Colegrove, P. and H. Shercliff, "CFD Modeling of Friction Stir Welding of Thick Plate 7449 Aluminium Alloy". *Science and Technology of Welding and Joining*, 2006: p. 429-441.

48. Chang, C., C. Lee, and J. Huang, "Relationship between Grain Size and Zener-Holloman Parameter during Friction Stir Processing in AZ31 Mg Alloys". *Scripta Materialia*, 2004: p. 509-514.

49. Ulysse, P., "Three-Dimensional Modeling of hte Friction Stir-Welding Process". *International Journal of Machine Tools and Manufacture*, 2002: p. 1549-1557.

50. Tianzhong, L., T. Seidel, T. Wei, and A. Reynolds, "A Friction Stir Welding Model Using Computational Fluid Dynamics". *The Materials Society*, 2003: p. 299-312.

51. Colegrove, P. and H. Shercliff, "3-Dimensional CFD Modeling of Flow Round a Threaded Friction Stir Welding Tool Profile". *Journal of Materials Processing Technology*, 2005: p. 320-327.

52. Colegrove, P., H. Shercliff, and R. Zettler, "Model for Predicting Heat Generation and Temperature in Friction Stir Welding from the Material Properties". *Science and Technology of Welding and Joining*, 2007: p. 284-297.

53. Seidel, T. and A. Reynolds, "Two-Dimensional Friction Stir Welding Process Model Based on Fluid Mechanics". *Science and Technology of Welding and Joining*, 2003: p. 175-183.

54. Nandan, R., G. Roy, T. Lienert, and T. DebRoy, "Three-Dimensional Heat and Material Flow during Friction Stir Welding of Mild Steel". *Acta Materiala*, 2007: p. 883-895.

55. Buffa, G., J. Hua, R. Shivpuri, and L. Fratini, "A Continuum Based FEM Model for Friction Stir Welding - Model Develoment". *Materials Science Engineering A*, 2006: p. 389-396.

56. Arbegast, W. *Modeling Friction Stir Joining as a Metalworking Process*. in *Proceedings of Hot Defomation of Al Alloys III*. 2003. San Diego, CA.

57. Nandan, R., G. Roy, T. Linert, and T. DebRoy, "Numerical Modelling of 3D Plastic Flow and Heat Transfer during Friction Stir Welding of Stainless Steel". *Science and Technology of Welding and Joining*, 2006: p. 526-537.

58. Kocks, U. and H. Mecking, "Physics and phenomenology of strain hardening: the FCC case". *Progress in Materials Science*, 2003: p. 171-273.

59. Sellars, C. and W. Tegart, "Hot Workability". *International Metallurgical Reviews*, 1972: p. 1-24.

60. Sheppard, T. and D. Wright, "Determination of Flow Stress: Part 1 Constitutive Equation for Aluminium Alloys at Elevated Temperatures". *Metals Technology*, 1979: p. 215-223.

61. Sheppard, T. and A. Jackson, "Constitutive Equations for use in Prediction of Flow Stress during Extrusion of Aluminum Alloys". *Materials Science Technology*, 1997: p. 203-209.

62. Johnson, G. and W. Cook. *A Constitutive Model and Data for Metals Subjected to Large Strains, High Strain Rates and High Temperature*. in *Proceedings of the Seventh International Symposium on 'Ballistics'*. 1983. The Hague, Netherlands.

63. Hart, E., C. Li, H. Yamada, and G. Wire, "Phenomenological Theory - Guide to Constitutive Relations and Fundamental Deformation Properties". *Constitutive Equations in Plasticity*, 1975: p. 149-197.

64. Lesuer, D., *Experimental Investigations of Material Models for Ti-6Al-4V and 2024-T3*. 1999, DOE: Oak Ridge, TN.

65. Johnson, G., Hoegfeldt, JM, U. Lindholm, and A. Nagy, "Response of Various Metals to Large Torsional Strains Over a Large Range of Strain Rates-Part 2: Less Ductile Metals". *Journal of Engineering Materials and Technology*, 1983.

66. Kozlowski, P., B. Thomas, J. Azzi, and H. Wang, "Simple Constitutive Equations for Steel at High Temperature". *Metallurgical Transactions A*, 1992: p. 903-918.

67. Wray, P., "Effect of Carbon Content on the Plastic Flow of Plain Carbon Steels at Elevated Temperatures". *Metallurgical Transactions A*, 1982: p. 125-134.

68. Suzuki, T., K. Tacke, and K. Wunnenberg, "Creep Properties of Steel at Continuous Casting Temperatures". *Ironmaking and Steelmaking*, 1988: p. 90-.

69. *Metal Handbook Mechanical Testing*. 1985, Metal Park, OH: American Society for Metals.

70. Cook, P. *True Stress-Strain Curves for Steel in Compression at High Temperatures and Strain Rates, for Application to the Calculation of Load and Torque in Hot Rolling*. in *Proceedings of the Conference on Properties of Materials at High Rate of Strain*. 1957: IME.

71. Forrest, D., J. Nguyen, M. Posada, J. DeLoach, D. Boyce, J. Cho, and P. Dawson. *Simulation of HSLA-65 Friction Stir Welding*. 2005. Pine Mountain, GA: ASM International.

72. Chaudhury, P. and V. January, *Atlas of Formability, Aluminum 5083*. 1993, NCEMT: Johnsontown, PA.

73. Chen, S. and U. Kocks, *High-temperautre plasticity in copper polycrystals*, in *High temperature constitutive modeling*. 1991, Am. Soc. Mech. Eng.: New York.

74. Mecking, H., B. Nicklas, and N. Zarubova, "A 'universal' temperature scale for plastic flow". *Acta Metallurgica*, 1986: p. 527-535.

75. Gray, G., S. Chen, W. Wright, and M. Lopez, *Constitutive Equations for Annealed Metals under Compression at High Strain Rates and High Temperatures*. 1994, Los Alamos National Laboratory: Los Alamos, NM.

76. Kuykendall, K., C. Sorensen, and T. Nelson. *A Comparison of Experimental Data and Model Predictions with Consitutitive Laws Commonly used to Model Friction Stir Welding*. 2011. San Diego, CA: John Wiley and Sons, Inc.

77. Follansbee, P. and U. Kocks, "A Constitutive Description of the Deformation of Copper Based on the Use of the Mechanical Threshold Stress as an Internal State Variable". *Acta Metallurgica*, 1988: p. 81-93.

78. Kalidindi, S., "Incorporation of Deformation Twinning in Crystal Plasticity Models". *Journal of the Mechanics and Physics of Solids*, 1998. 46(2): p. 5.

79. Salem, A., Kalidindi, SR, Semiatin, SL, "Strain Hardening due to Deformation Twinning in α-Titanium: Constitutive Relations and Crystal-Plasticity Modeling". *Acta Materiala*, 2005. 53: p. 8.

80. Mahajan, S. and D. Williams, "Deformation Twinning in Metals and Alloys". *International Metallurgical Reviews*, 1973. 18(2): p. 43-61.

81. Rohatgi, A., K. Vecchio, and G.I. Gray, "The Influence of Stacking Fault Energy on the Mechanical Behavior of Cu and CU-Al Alloys: Deformation Twinning, Work Hardening, and Dynamic Recovery". *Metallurgical and Materials Transactions A*, 2001. 32: p. 135-142.

82. Remy, L., "The Interaction between Slip and Twinning Systems and the Influence of Twinning on the Mechanical Behavior of fcc Metals and Alloys". *Metallurgical Transactions A*, 1981: p. 387-408.

83. Meyers, M., O. Vohringer, and V. Lubarda, "The Onset of Twinning in Metals: A Constitutive Description". *Acta Materialia*, 2001: p. 4025-4039.

84. Schneider, M., B. Kad, D. Kalantar, B. Remington, E. Kenik, H. Jarmakani, and M. Meters, "Laser Schock Compression of Copper and Copper-Aluminum Alloys". *International Journal of Impact Engineering*, 2005: p. 473-507.

85. Johari, O. and G. Thomas, "Substructures in Explosively Deformed Cu and Cu-Al Alloys". *Acta Metallurgica*, 1964: p. 1153-1159.

86. Han, W., Z. Zhang, S. Wu, and S. Li, "Combined Effects of Crystallographic Orientation, Stacking Fault Energy and Grain Size on Deformation Twinning in FCC Crystals". *Philosophical Magazine*, 2008: p. 3011-3029.

87. Khatak, H. and R. Baldev, *Corrosion of Austenitic Stainless Steels: Mechanism, Mitigation, and Monitoring*. 2002: Woodhead Publishing.

88. Hertzberg, R., *Deformation and Fracture Mechanics of Engineering Materials*. 1996, Hoboken, NJ: John Wiley and Sons, Inc.

89. Murr, L. and P. Smith, Gilmore, CM, "Relatie Interfacial Free Energies in Pure Nickel, Dispersion Hardened Nickel, and a Precipitation Hardened Nickel-Based Alloy". *Philosophical Magazine*, 1968: p. 89-106.

90. Holden, T., R. Holt, and A. Clarke, "Intergranular Strains in Inconel-600 and the Impact on Interpreting Stress Fields in Bent Steam-Generator Tubing". *Materials Science and Engineering*, 1998: p. 180-198.

91. Ryan, N. and H. McQueen, *Comparative Kocks and Mecking Analysis of the Dynamic Recovery of 304 and 309*, in *Advances in Hot Deformation Texutres and Microstructures*. 1994, The Minerals, Metals, and Materials Society. p. 445-457.

92. Zhang, H., Z. Hei, G. Liu, J. Lu, and K. Lu, "Formation of Nanostructured Surface Layer on AISI 304 Stainless Steel by Means of Surface Mechanical Attrition Treatment". *Acta Materialia*, 2003: p. 1871-1881.

93. Kuhn, H., *Atlas of Formability, Cast Aluminum 3004*. 1991, NCEMT: Johnsontown, PA.

94. Kuhn, H., *Atlas of Formability, Inconel 600*. 1991, NCEMT: Johnsontown, PA.

95. Murr, L., Vydyanath, HR, Foltz, JV, "Comparison of the Substructures and Properties of Nickel, TD-Ni, Chromel-A, Inconel 600, and TD-NiCr Following Explosive-Shock Deformation". *Metallurgical and Materials Transactions B*, 1970. 1(11): p. 3215-3223.

APPENDIX A. HICKORY CODE CHANGES

This document describes modifications made to the Hickory code to implement new constitutive laws. The subroutines created to calculate viscosity as function of strain rate, temperature, and/or state variable in material.f are shown below. The evolution of the state variable (if applicable) was added to sv-dot.F. The state variable evolution functions for the Johnson-Cook and Kocks and Mecking laws are shown below. A new function to calculate shear modulus was created and is shown under shearmod.f. All other changes associated with the implementation will be described by listing the file title and a summary of the changes.

material.f

- Three subroutines were added: one for each constitutive law. The calculation of flow stress as a function of state variable, strain rate, and/or temperature was included in this file.

```
c-----------------------------------------------------------------------
c
c
      SUBROUTINE vssellars(itan, npts, cmatl, d2, visc, dvdd2,
     &   sv1, temp)
c
c     Sellars and Tegart viscosity model.
c
c-----------------------------------------------------------------------
c
      IMPLICIT NONE
c
c     Arguments:
c
c     itan : flag indicating derivative calculation       (input only)
c     npts : number of points                             (input only)
```

```
c
      INTEGER itan, npts
c
c     cmatl: model parameters                                (input only)
c     d2   : effective deformation rate                      (input only)
c     visc : viscosity                                       (output)
c     dvdd2: derivative of viscosity wrt deformation rate    (output)
c     sv1  : state variable 1                                (input only)
c     temp : temperature                                     (input only)
c
      DOUBLE PRECISION cmatl(*), d2(*), visc(*), dvdd2(*),
     &   sv1(*), temp(*)
c
c     Local Variables:
c
      INTEGER i
c
      DOUBLE PRECISION A, alpha, Q, n, d, scaling, cut, r,
     &   hol
c
c-----------------------------------------------------------------------
      A = cmatl(1)
      alpha = cmatl(2)
      Q = cmatl(3)
      n = cmatl(4)
c
      cut = cmatl(5)

      r = 8.314
c
c
      do i=1, npts
c
        d = d2(i)
c
        if (d .lt. cut) then
          d = (cut*0.5d0)*(1.0d0+(d/cut)**2)
        endif
c
        hol = d*dexp(Q/(r*temp(i)))
        visc(i) =
     &   ( ((1/alpha)*dlog((hol/A)**(1/n)+(1+(hol/A)**(2/n))**(1/2)))
     &     /(3.0d0*d))*(1*10**6)

        if (itan .ne. 0) then
c
c         Newton's method.
c
!           dvdd2(i) = (pwr - 1.0d0) * visc(i)/d
c
c         Account for derivative of cutoff function.
c
```

```
          if (d2(i) .le. cut) then
            scaling  = d2(i)/cut
            dvdd2(i) = scaling * dvdd2(i)
          endif
c
        endif
c
      enddo
c
      RETURN
      END
c
c-------------------------------------------------
c
c
      SUBROUTINE vsjcook(itan, npts, cmatl, d2, visc, dvdd2,
     &   sv1, temp, strain, ireffr)
c
c     Johnson-Cook viscosity model.
c
c-----------------------------------------------------------------------
-
c
      IMPLICIT NONE
c
c     Arguments:
c
c     itan : flag indicating derivative calculation       (input only)
c     npts : number of points                             (input only)
c     ireffr : problem type (Eulerian = 0)
c
      INTEGER itan, npts, ireffr
c
c     cmatl: model parameters                             (input only)
c     d2   : effective deformation rate                   (input only)
c     visc : viscosity                                    (output)
c     dvdd2: derivative of viscosity wrt deformation rate (output)
c     sv1  : state variable 1                             (input only)
c     temp : temperature                                  (input only)
c     strain: strain                                      (input only)
c
      DOUBLE PRECISION cmatl(*), d2(*), visc(*), dvdd2(*),
     &   sv1(*), temp(*), strain(*)
c
c     Local Variables:
c
      INTEGER i
c
      DOUBLE PRECISION A, B, n, C, m, d, scaling, cut, epsnot,
     &   Troom, Tmelt, Tstar
c
c-----------------------------------------------------------------------
```

```
      A = cmatl(1)
      B = cmatl(2)
      n = cmatl(3)
      C = cmatl(4)
      m = cmatl(5)
      Tmelt = cmatl(6)
      cut = cmatl(7)

      Troom = 298.15
      epsnot = 1.0
c
c
      do i=1, npts
c
        d = d2(i)
c
        if (d .lt. cut) then
          d = (cut*0.5d0)*(1.0d0+(d/cut)**2)
        endif
c
        Tstar = (temp(i)-Troom)/(Tmelt-Troom)
        if (ireffr .eq. 0) then
        visc(i) = (((A+(B*(sv1(i)**n)))*(1+(C*dlog(d/epsnot)))*
     &     (1-(Tstar**m)))/(3.0d0*d))*1000000

        elseif (ireffr .eq. 1) then
        visc(i) = (((A+(B*(strain(i)**n)))*(1+(C*dlog(d/epsnot)))*
     &     (1-(Tstar**m)))/(3.0d0*d))*1000000
        endif
c
        if (itan .ne. 0) then
c
c         Newton's method.
c
!           dvdd2(i) = (pwr - 1.0d0) * visc(i)/d
c
c         Account for derivative of cutoff function.
c
          if (d2(i) .le. cut) then
            scaling  = d2(i)/cut
            dvdd2(i) = scaling * dvdd2(i)
          endif
c
        endif
c
      enddo
c
      RETURN
      END
c
c-------------------------------------------------
c
```

```
c
      SUBROUTINE vskmeck(itan, npts, cmatl, d2, visc, dvdd2,
     &   sv, temp, mut, sigv, hardrate, qphrate, qpsigv, incr, ielem,
nqp, ne,
     &   ystress, qpyield, sv1, ireffr, qpmu, qpssat)
c
c     Kocks and Mecking viscosity model.
c
c-----------------------------------------------------------------------
c
      IMPLICIT NONE
c
c     Arguments:
c
c     itan : flag indicating derivative calculation       (input only)
c     npts : number of points                             (input only)
c     ireffr : Problem Flag (0-Eulerian)                  (input only)
c

      INTEGER itan, npts, incr, ielem, nqp, ne, ireffr
c
c     cmatl: model parameters                             (input only)
c     d2   : effective deformation rate                   (input only)
c     visc : viscosity                                    (output)
c     dvdd2: derivative of viscosity wrt deformation rate (output)
c     hardrate  : hardening rate                          (input only)
c     temp : temperature                                  (input only)
c     strain: strain                                      (input only)
c     oldstress: stress from previous timestep            (input only)
c
      DOUBLE PRECISION cmatl(*), d2(*), visc(*), dvdd2(*),
     &   sv(*), temp(*), mut(*), sigv(*), hardrate(*),
     &   qphrate(nqp,ne), qpsigv(nqp,ne), ystress(*),
     &   qpyield(nqp,ne), sv1(*), qpmu(nqp,ne), qpssat(nqp,ne)
c
c     Local Variables:
c
      INTEGER i
c
      DOUBLE PRECISION sigv0, p, q, epsnot, b,
     & g0, hrate0, sv0, d, scaling, cut, k, a0, a1, a2, a3, a4,
     & sigy0, gy0, SATUR, g
     PARAMETER(SATUR=0.99D0)
c-----------------------------------------------------------------------
      b = cmatl(1)
      sigv0 = cmatl(2)
      p = cmatl(3)
      q = cmatl(4)
      epsnot = cmatl(5)
      g0 = cmatl(6)
      hrate0 = cmatl(7)
      a0 = cmatl(8)
```

```
      a1 = cmatl(9)
      a2 = cmatl(10)
      a3 = cmatl(11)
      a4 = cmatl(12)
      sigy0 = cmatl(13)
      gy0 = cmatl(14)
      cut = cmatl(15)
      k = 1.3806503d-23
      call shearmod(temp,mut,a0,a1,a2,a3,a4,npts)
c
c

      do i=1, npts
c
        d = d2(i)
c
        if (d .lt. cut) then
          d = (cut*0.5d0)*(1.0d0+(d/cut)**2)
        endif

        g = k*temp(i)*(1/(mut(i)*1.0d6))*(1/(b**3))*dlog(epsnot/d)


        if (g .gt. gy0) then
          ystress(i)=sigy0*mut(i)*((1-SATUR**p)**q)*1000000
        else
        ystress(i) = (mut(i)*sigy0*(1-((1/gy0)*g)**p)**q)*1000000
        endif
c
        if (g .gt. g0) then
          sigv(i) = sigv0*mut(i)*((1-SATUR**p)**q)*1000000
        else
        sigv(i) = (mut(i)*sigv0*(1-((1/g0)*g)**p)**q)*1000000
        endif
        qpsigv(i,ielem) = sigv(i)


        if (ireffr .eq. 1) then
        visc(i) = (sv(i)*ystress(i)*(1/1000000.0d0))/(3.0d0*d)
        qpyield(i,ielem) = ystress(i)*(1/1000000.0d0)

        qpmu(i,ielem) = mut(i)*(1/ystress(i))*1000000*hrate0
        qpssat(i,ielem) = sigv(i)/ystress(i)

c
        elseif (ireffr .eq. 0) then
        visc(i) = (sv1(i)*ystress(i))/(3.0d0*d)
        qpyield(i,ielem) = ystress(i)
        qpmu(i,ielem) = mut(i)*hrate0*(1/ystress(i))*1000000
        qpssat(i,ielem) = sigv(i)/ystress(i)
        endif
```

```
        if (itan .ne. 0) then
c
c         Newton's method.
c
!           dvdd2(i) = (pwr - 1.0d0) * visc(i)/d
c
c         Account for derivative of cutoff function.
c
          if (d2(i) .le. cut) then
            scaling  = d2(i)/cut
            dvdd2(i) = scaling * dvdd2(i)
          endif
c
        endif
c
      enddo
c      endif
c
      RETURN
      END
c-------------------------------------------------
```

sv-dot.F

- Two if statements were added to this section to calculate the evolution of the state variable: one for Johnson-Cook and one for Kocks and Mecking. The evolution of the state variable for each law is shown below.
- Johnson-Cook
    - `dsdt = d2i`
        - `d2i` is the strain rate
- Kocks and Mecking
    - `dsdt = mu*(1-(stv1/ssatkm))*d2i`
        - `d2i` is the strain rate
        - `mu` is the temperature dependent shear modulus
        - `stv1` is the state variable
        - `ssatkm` is the saturation state variable

shearmod.f

- A new function file was created to calculate temperature dependent shear modulus.

```
c-----------------------------------------------------------------------
c
c
      SUBROUTINE shearmod(temp,mut,a0,a1,a2,a3,a4,npts)
c
c     Calculate shear modulus as function of temperature.
c
c-----------------------------------------------------------------------
-
c
      IMPLICIT NONE
c
c     Arguments:
c
c     npts : number of points                              (input only)
c
      INTEGER npts
c
c     temp : temperature                                   (input only)
c
      DOUBLE PRECISION temp(*), mut(*), a0, a1,
     &    a2, a3, a4
c
c     Local Variables:
c
      INTEGER i
c
c
c-----------------------------------------------------------------------
-
c
c
c
c
c
      do i=1, npts
c
            mut(i) =
a0+temp(i)*(a1+temp(i)*(a2+temp(i)*(a3+temp(i)*a4)))

      enddo
c
      RETURN
      END
c
c-------------------------------------------------
```

cmnja.h

- Velocity point and quadrature point vectors were added to account for hardening rate, yield stress, and saturation stress.

cmnsl.h

- Streamline vectors were added to account for hardening rate, yield stress, and saturation stress.

matlvs.F

- Calls to each of the three added constitutive laws were added in this file.

streamline.F

- Streamline calculations were added for hardening rate, yield stress, and saturation stress.

npquant.F

- Statements were added to pull local values from global arrays for hardening rate, yield stress, and saturation stress.

indat.F

- Statements were added to read in material parameters from an input file for the three new constitutive laws

gsmooth.F

- Relaxation parameters for temperature and state variable were adjusted to aid convergence.